4D seismic analysis: Discriminating between saturation and pressure changes form a data acquired Offshore Equatorial Guinea.

Department of Geological Sciences

Dissertation submitted in total fulfillment of the requirements of the degree Master of Science.

Andile Lucky Msolo

10 January 2016

Supervised by: Dr Beth Kahle, Mr Maurice Gidlow and Dr Richard Kahle

Abstract

4D seismic analysis is used to understand the performance of a producing oil field in order to increase production and mitigate risk. This is done by interpreting changes in water saturation and changes in effective pressure in the reservoir, which allows production to be maximized safely. In this project, I determined saturation and pressure changes in an oil field offshore Equatorial Guinea. I used Landrø's technique as a basis for the analysis, however Landrø's technique requires the presence of reservoir samples. For this project, rock samples of the reservoir were not available; this led me to modify Landrø's methodology using approximations based on well-accepted rock physics relationships. I tested this new methodology on a synthetic model, which gave encouraging results, after which it was applied to real seismic data.

Pressure and saturation changes estimated in the reservoir indicate that the northern part of the reservoir experienced a decrease in pore pressure. The saturation changes over the northern part of the reservoir are not prominent. The central and southern parts of the reservoir show an increase in water saturation accompanied by an increase in pore pressure. The results are consistent with the production and injection history of this area.

A comparison between saturation before production, saturation changes after production and pressure changes after production indicates an area (on the northern part of the reservoir) which shows fluid anomalies before production and does not show any production (or 4D) effects. New production wells could potentially be drilled in this area to increase production.

Acknowledgements

I would like to thank my supervisor, Dr Beth Kahle for her advice, guidance and by ensuring that I had all the software I needed to do my dissertation.

I would like to thank Tullow Oil for providing the project, data and funding to make this possible. Special thanks to Mr Maurice Gidlow from Tullow Oil for helping me through the dissertation. Special thanks to Dr Richard Kahle from University of Cape Town for his input on the project.

I thank the Department of Geological Sciences for giving me the opportunity to do my dissertation.

Contents

List of Figures

List of Tables

Glossary

(Definitions are obtained from the Encyclopedic Dictionary of Exploration Geophysics, Sheriff R. E., 1990**)**

Air gun: A seismic source that injects a bubble of highly compressed air into the water.

AVO Class: Variation of reflection amplitude with offset exhibited by the top of hydrocarbon reservoir (Rutherford and Williams, 1989).

Bulk modulus: The stress-strain ratio under simple hydrostatic pressure.

Correlation coefficient: A measure of the goodness of fit of one function to another.

Migration: An inversion operation involving rearrangement of seismic information elements so that reflections and diffractions are plotted at their true locations.

Pressure (Pa): Force per unit area.

- **Effective pressure (Confining pressure)**: The difference between the pressure of a rock's pore fluid and that produced by the weight of the overburden.
- **Lithostatic pressure (Overburden pressure)**: The pressure caused by overlying rock (and water in the case of offshore).
- **Pore pressure**: The pressure of the fluids in the interstices in a rock.

Elastic: The ability to return to its original shape after removal of a distorting stress.

Fluid factor: The measure that indicates that the pore fluid is gas rather than liquid. This is a perpendicular distance away from a trend line in a cross-plot of Vp vs Vs. In reflectivity, fluid factor can be viewed as a perpendicular distance away from a background trend in a cross-plot of Vp vs Vs reflectivity.

Frequency (Hz): The repetition rate of a periodic waveform, measured in Hertz or "cycles per second". This is the reciprocal of period.

Pore space stiffness: The pore space stiffness is the inverse of the dry rock pore space compressibility (Russell, 2013). This is the bulk modulus of the dry pore space.

P-wave: An elastic body wave in which particle motion is in the direction of propagation.

Reflectivity: The ratio of the amplitude of the displacement of a reflected wave to that of the incident wave.

Rock physics: A link between qualitative geologic parameters (porosity, clay content, etc.) and quantitative geophysical measurements (P-wave velocity, S-wave velocity, etc.**)**. (Avserth et al., 2010).

Seismic-Well tie: A correlation between seismic data and a synthetic (from log data) seismic trace to (1) correctly identifying horizons to pick and (2) estimating the wavelet for inverting seismic data to impedance (White and Simm, 2003).

Strain: The change of dimensions or shape produced by a stress.

Shear modulus: The stress-strain ratio for simple shear.

Spectra: Amplitude and phase characteristics as a function of frequency for the components of wavetrain or wavelet.

S-wave: A body wave in which the particle motion is perpendicular to the direction of propagation.

Trace: A record of the data from, for instance, one seismic channel.

Vibroseis: A seismic method in which a vibrator is used as an energy source to generate a controlled wavetrain.

Vp: Velocity of a P-wave.

Vs: Velocity of a S-wave.

Water Saturation (Sw or S): Fraction of the pore volume filled with formation water.

Used terminology

$\frac{\Delta V}{V} = \text{velocity reflectivity}$

$\frac{\Delta \rho}{\rho} = \text{density reflectivity}$

$R = \text{reflection coefficient or reflectivity}$

Chapter 1: Introduction

1.1 Aim

The purpose of this project is to use 4D seismic data to investigate the changes in fluid saturation and the changes in effective pressure from a producing field in West Africa. Changes in effective pressure (or pore pressure) and water saturation help in the maintenance and risk management of the field. For example, saturation changes show areas where hydrocarbons have been replaced by water. This allows interpreters to propose new producing wells if there are areas where hydrocarbons have not been removed. Effective pressure changes cause different processes in the reservoir depending on whether the effective pressure decreased or increased. If the pore pressure rises too high, the injector wells may need to be shut to prevent fracturing of the reservoir, or when new wells are drilled we can get water or hydrocarbons flowing into the bore hole. If the pore pressure falls too low, gas may come out of solution.

1.2 Location of the field

The field used as an example in this study is located offshore Equatorial Guinea (EG). Figure 1 shows the producing fields located offshore EG. The exact location of the field is not indicated for confidentiality reasons. The field is been producing for the last 13 years.

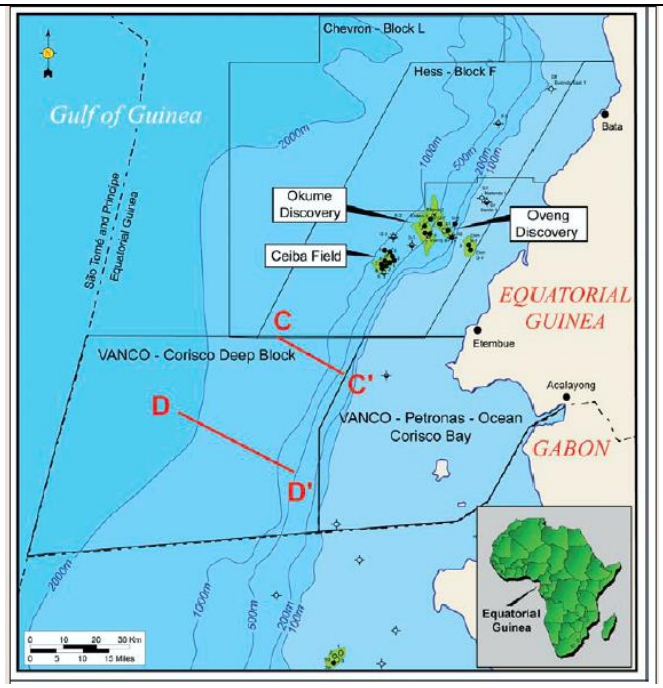

Figure 1: Producing fields located offshore Equatorial Guinea. Image from Coterill et al. (2002).

1.3 Geological settings

A cross-section illustrating the general regional geology of the area is shown in Figure 2. The basement is made up of pre-Mesozoic rocks which are overlain by Cretaceous onlapping sequences followed by Aptian salt which is not present in all areas (Coterill et al., 2002). The salt is overlain by a thick Aptian to Albian sedimentary sequences (Dailly et al., 2002). These thick sequences are overlain by Cenomanian to Turonian units which are believed to contain the source rock for hydrocarbons in the area (Dailly et al., 2002 and Coterill et al., 2002). Above the Cenomanian-Turonian units there are Santonian to Campanian sequences. These Santonian to Campanian sequences have turbidite systems stacked on top of one another which, along with canyon sands form the reservoir in this area (Dailly et al., 2002 and Coterill et al., 2002). The Sentonian units are overlain by Tertiary sequences showing progradation (Coterill et al., 2002 and Dailly et al., 2002).

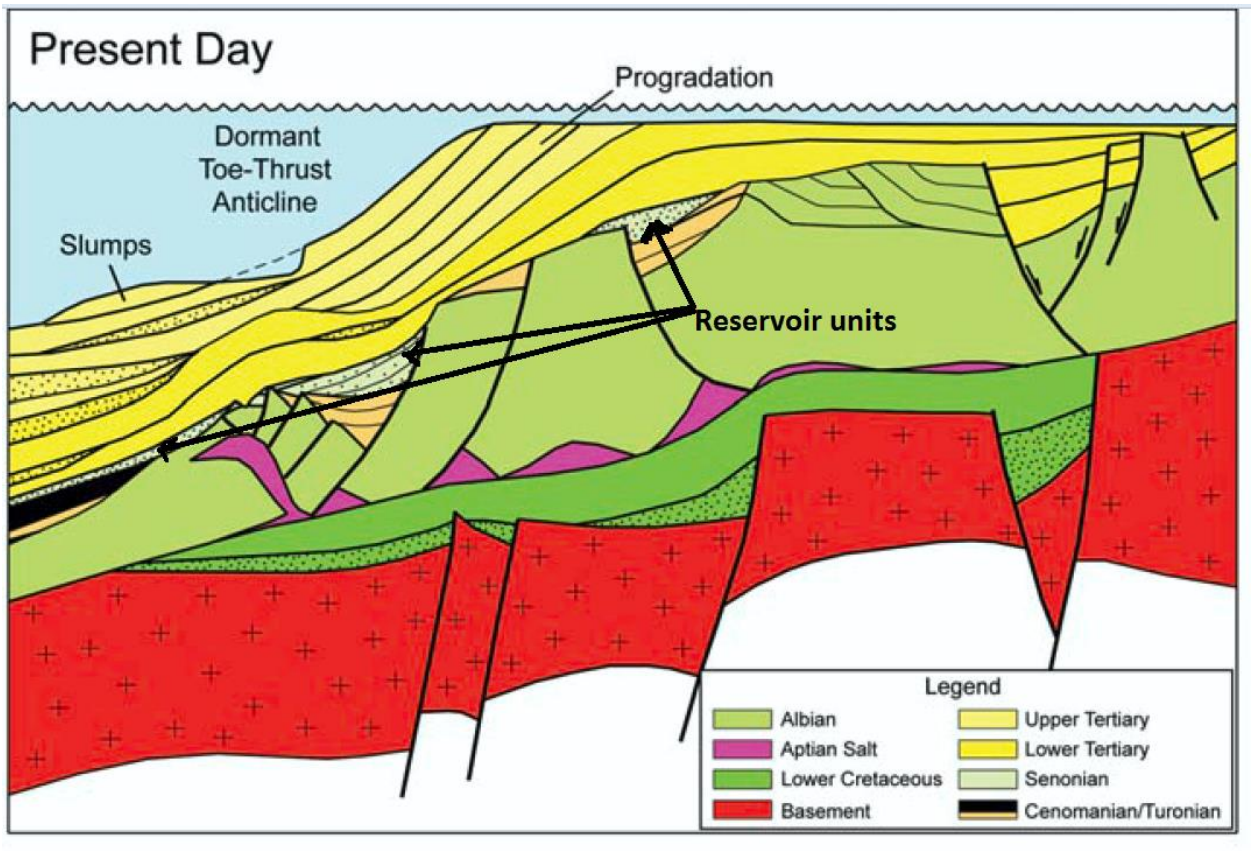

Figure 2: Regional geology of the area of study. Image modified from Coterill et al. (2002).

1.4 Dataset

Three seismic surveys were acquired over the area of study, in 1999, 2003 and 2010. The seismic data were acquired by a vessel equipped with two air gun arrays that were 25m apart. For this acquisition the air guns had compressed air at 2000psi (13.8MPa) of pressure. The vessel had 10 receiver cables that were 4500m long and were separated by 50m. The air gun arrays were 3.5m below the sea surface. The receiver cables were 4m below the sea surface. The distance between the air gun arrays and the nearest receiver was 85m along the inline (which is the direction in which the receiver cables are deployed).

The 1999, 2003 and 2010 seismic data were acquired using the same survey parameters (described above). To show the differences between these surveys, the seismic data were subtracted from one another to produce 2010-1999, 2003-1999 and 2010-2003 full stack (7°-47°), nears stack (7°-17°), mid stack (17°-27°), far stack (27°-37°) and ultrafar stack (37°-47°). In addition to the seismic data, log data for Well 1 (Fig. 3) were made available. Well 1 is the first exploration well in the area. The **IL** in Figure 3 stands for inline, which is the direction in which the receiver cables are deployed. **XL** stands for crossline, which is the direction perpendicular to the receiver cable.

The data went through a number of processing steps including attenuation compensation, signal deconvolution, swell noise attenuation, multiple removal, common mid-point sorting, velocity analysis, migration and stacking (summing the traces). The 2003 and 2010 frequency spectra were matched to the 1999 seismic data.

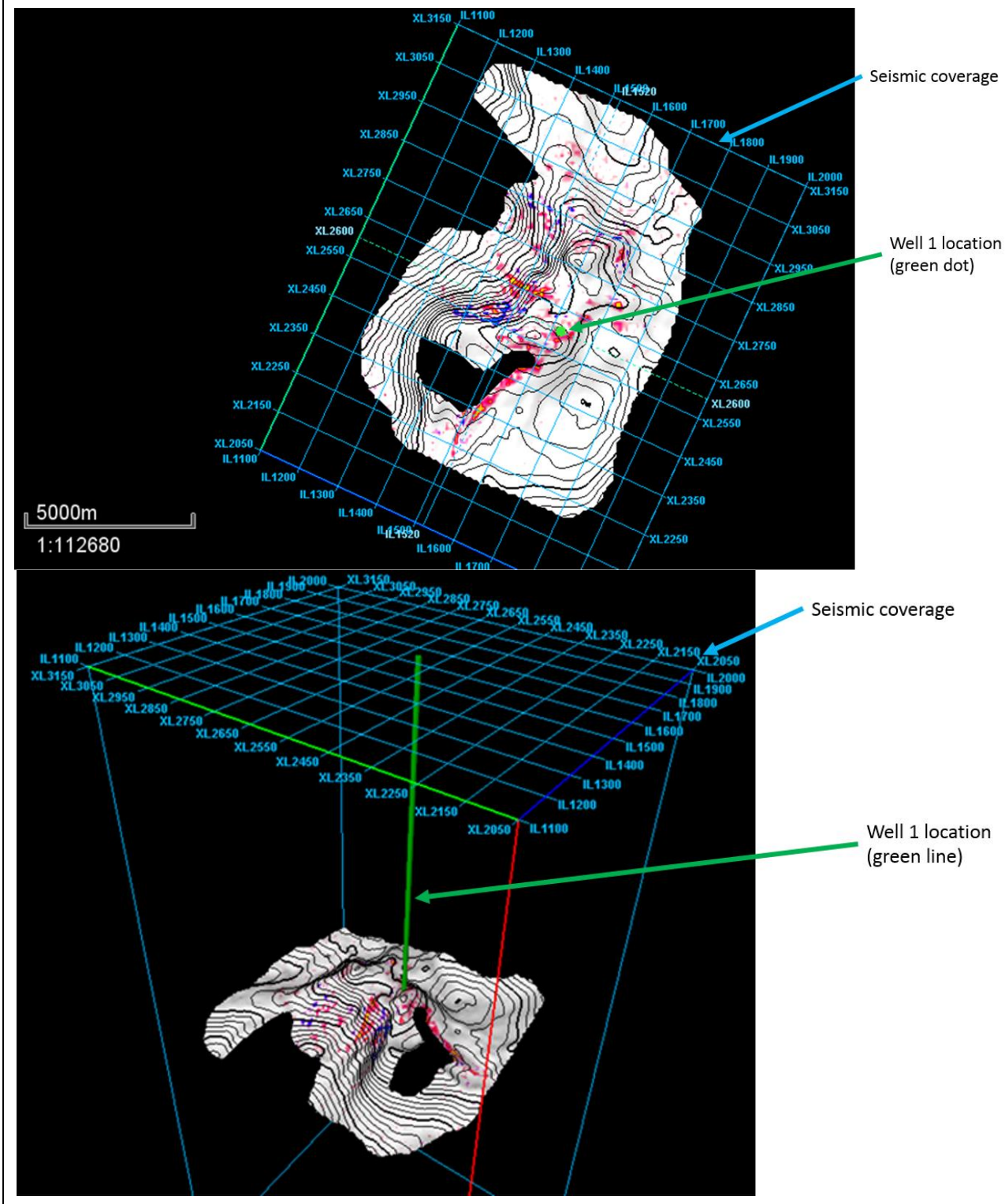

Figure 3: Location of Well 1 relative to seismic data (seismic geometry) and the reservoir. The map represents the spatial geometry of the reservoir and the contours represent time (ms).

1.5 General data acquisition and processing

During seismic acquisition, a ship tows a seismic source and a streamer/receiver cable (Fig. 4). The source is a combination of air guns and is called an air gun array. An air gun array is used rather than a single air gun because a single air gun produces an undesirable source signature. The receivers in the receiver cable are hydrophones (offshore) or geophones (onshore) and they detect the movement of the ground (onshore) or water (offshore) as a result of a traveling wave. Figure 4 shows a ship with a seismic source and a streamer with 4 highlighted receivers in the cable. For each shot, the receivers record reflections from different parts of the reflector (sea floor). **A plot of offset (receiver offset) and arrival times (two way time) of the reflections for each shot** produces a common shot gather (Fig. 5).

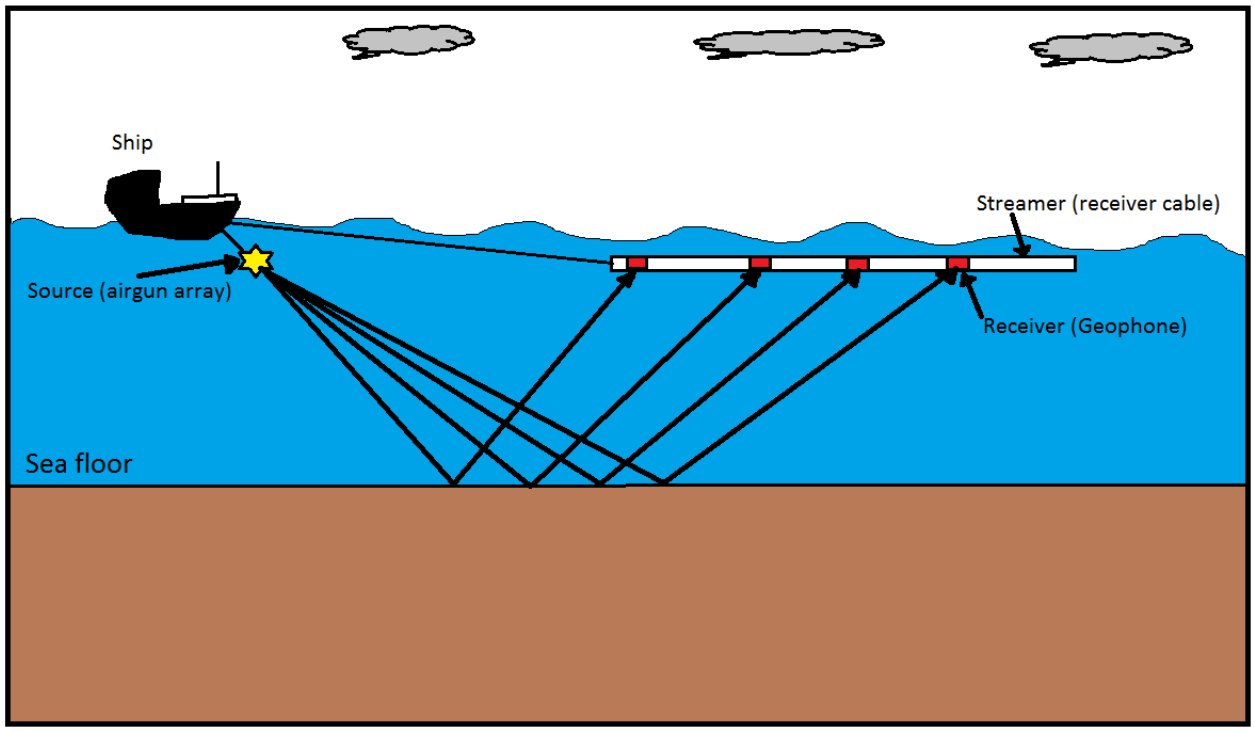

Figure 4: Seismic acquisition geometry showing a source and a receiver cable.

As the ship moves, the air gun array is fired at a specific time interval such that reflections reflected at the same point for different shots are recorded by successive receivers. After the survey, the data are rearranged such that all the traces reflected at the same point are plotted together to produce a common mid-point (CMP) gather also referred to a common depth point (CDP) (Fig. 5).

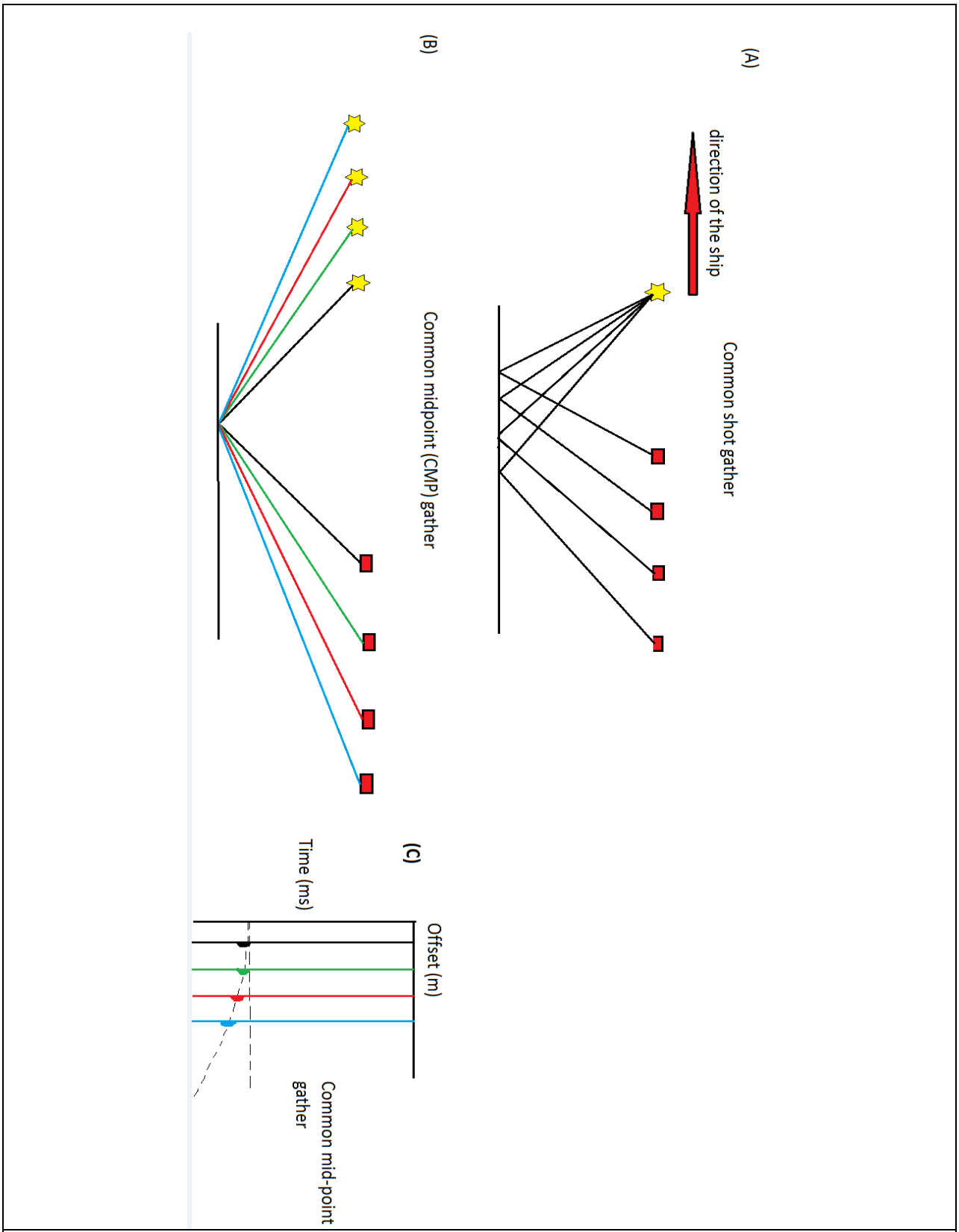

Figure 5: Cartoon showing the geometry of a common shot gather (A), a common mid-point (CMP) gather (B) and a plot of source reciever offset vs time for the CMP gather.

In an unprocessed CMP gather (Fig. 5), the TWT for recorded reflections are not equal. The difference in TWT (relative to the zero offset reflection) is called normal moveout (NMO). NMO correction is a process which correct for the TWT of reflections at offset other than zero to produce a flattened gather (Fig. 6). To correct for NMO, we need the normal moveout velocity (Vnmo), i.e. the velocity used to flatten the gathers.

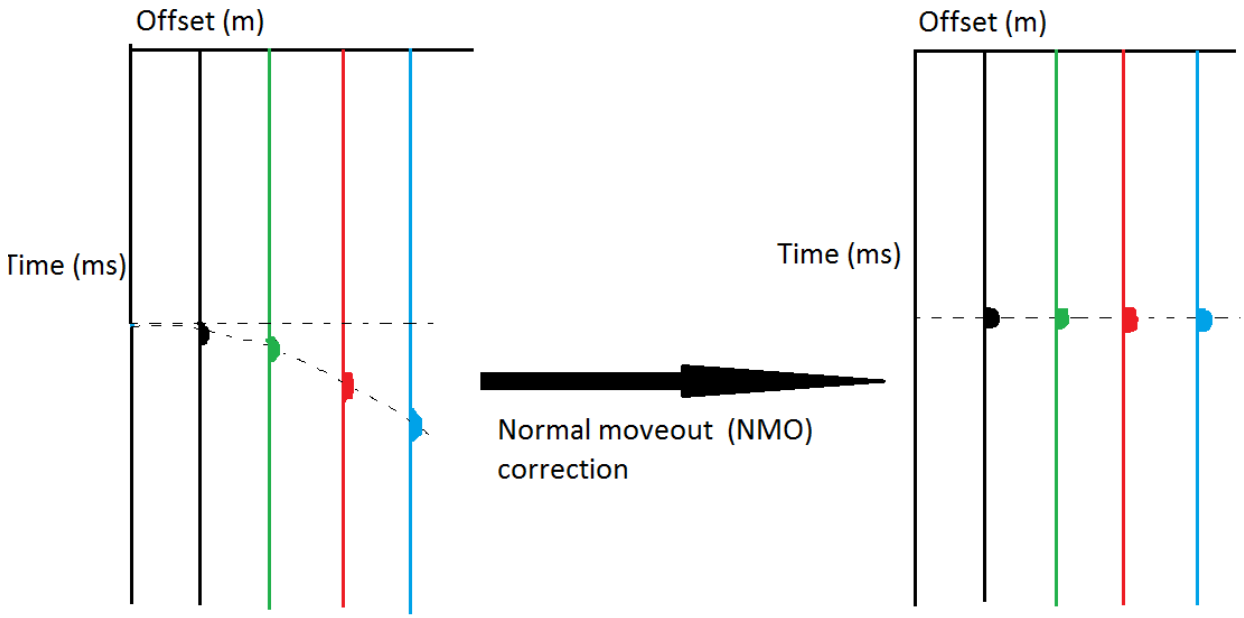

$$T(X)^2 = T_0^2 + \frac{X^2}{V_{nmo}^2}$$

X = offset, T(X) = Two way time traveled by a seismic wave at offset X, To = Two way time traveled by a seismic wave at zero offset. V_{nmo}^2 = Velocity required to flatten the gathers.

Figure 6: Normal moveout corrected CMP gather.

During velocity analysis, a velocity spectrum (Fig. 7) is produced by applying each velocity at different TWT to correct for normal moveout and stack (add) the traces of a gather (Tuner and Koehler, 1969). A correct velocity for a specific time will stack all the reflections and produce a big peak, shown by red colours on Figure 7 (Tuner and Koehler, 1969). After velocity analysis, the gather can be corrected for NMO (Fig. 6) and the offset can be converted to incident angle.

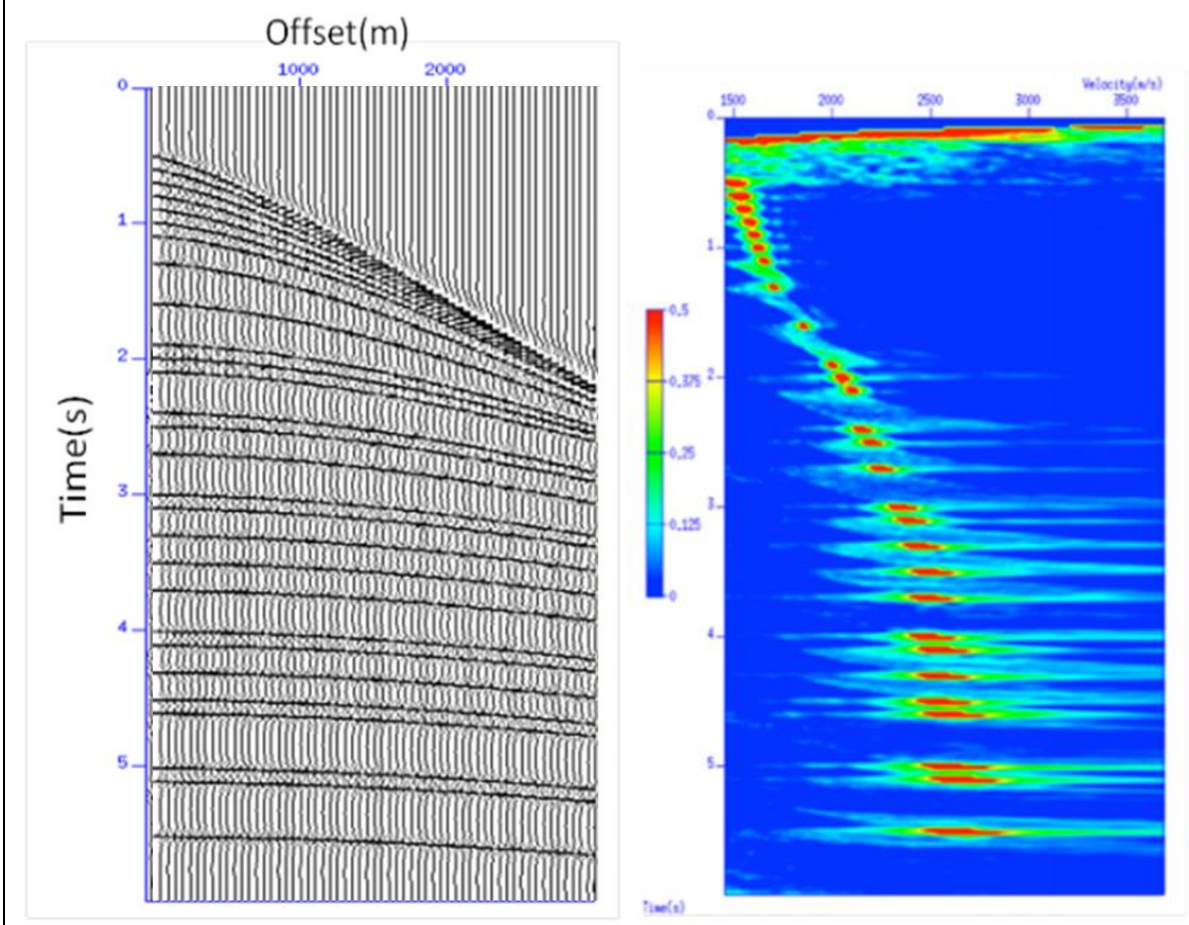

Figure 7: A typical velocity semblance plot (right) for a specific gather (left). Image from Ashcroft (2011).

Once the gathers are flattened, the amplitudes are summed (stacked) to produce a seismic section with relatively high amplitude to noise ratio (Simm et al., 2000 and Kemper, 2010).

After stacking, the seismic data may be migrated. Seismic migration is a process where seismic reflections are rearranged and plotted at their true locations. The need for migration arises since variable velocities and dipping reflectors cause reflections to be recorded at the surface positions different from their subsurface positions. If seismic migration is performed on a stacked seismic data, it is called **post-stack migration**. Seismic migration can also be performed on pre-stack CMP gather and is referred to as **pre-stack migration**. **Time migration** assumes that velocities of the subsurface do not change horizontally (only vertically) whereas **depth migration** assumes that velocities of the subsurface change vertically and horizontally.

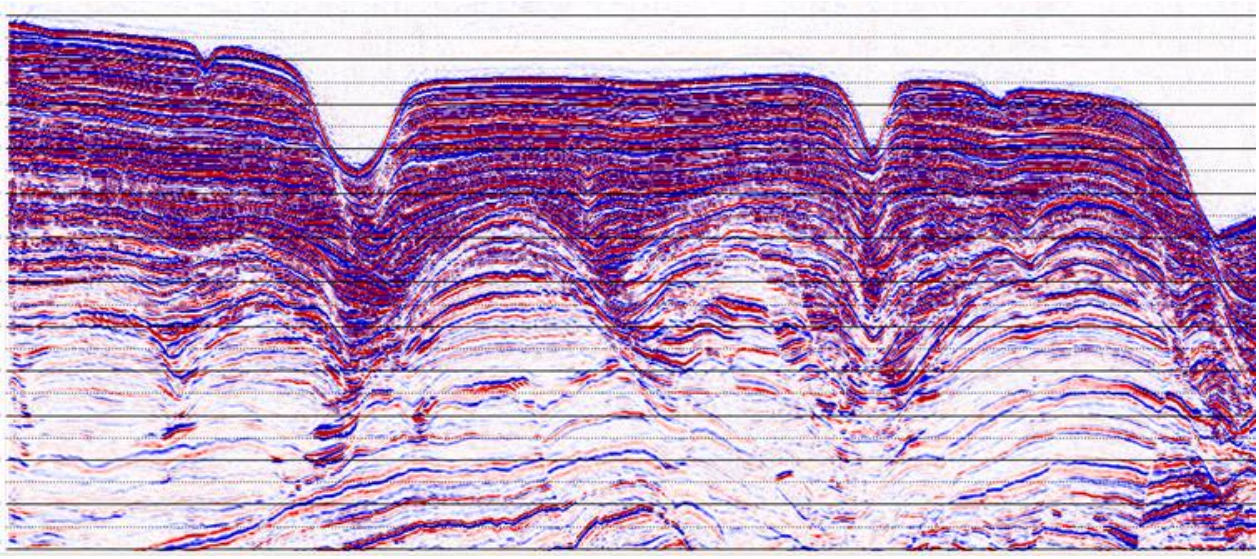

Figure 8: A typical stacked seismic data.

1.6 Background and development of AVO.

Since the 1920s, seismic reflection has been the main technique used for hydrocarbon exploration. The initial strategy was to search for structural features to target for drilling, for example anticlines; the selection process was based only on the structure of the subsurface (Chiburis et al., 1993).

When we search for sedimentary or structural features on seismic sections, we are looking at how the reflected amplitudes change vertically and laterally on the seismic section. These amplitudes depend on the reflection coefficient (Fig. 9). The reflection coefficient describes the fraction of seismic energy reflected back from an interface**. The reflected amplitude at the interface between two media is the product of the incident amplitude and the reflection coefficient** (R_{PP}). The reflection coefficient (R_{PP}) is the difference in the acoustic impedance between the two media divided by their sum (Fig. 9). Figure 9 shows the reflection coefficient between two media (1 and 2) assuming that the incident angle (θ) is zero. The incident angle is the angle between the down-going wave and the line that is perpendicular to the interface.

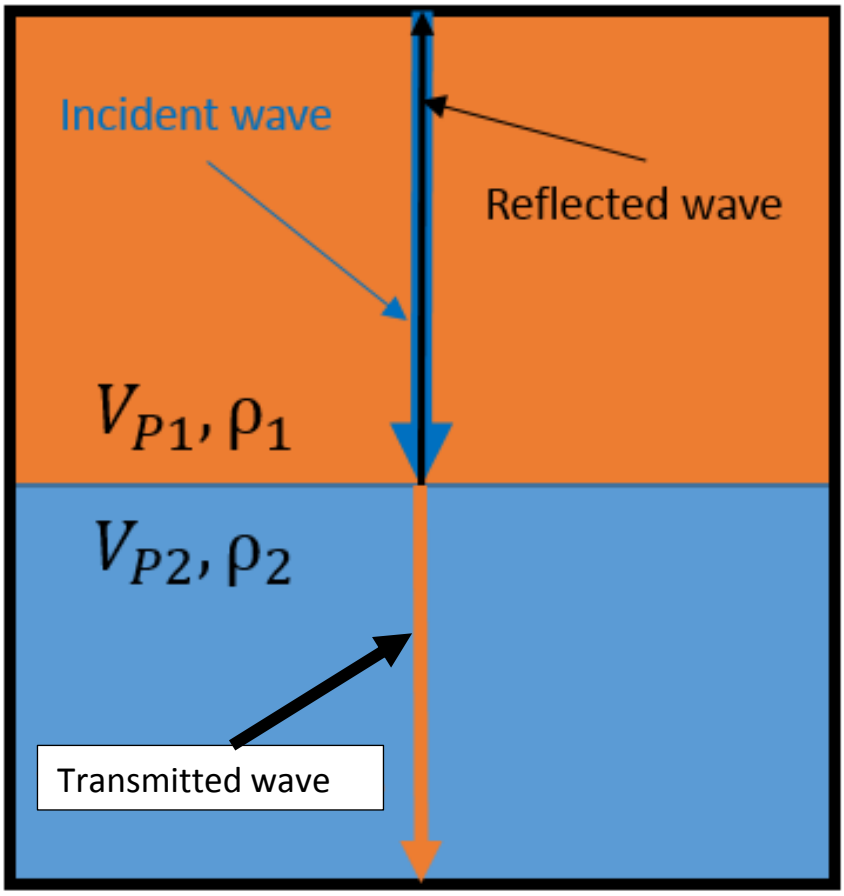

$$R_{PP} = \frac{V_{P2}\rho_2 - V_{P1}\rho_1}{V_{P2}\rho_2 + V_{P1}\rho_1}$$

ρ = Density

And

V_P = Compressional velocity

Figure 9: Reflection coefficient between two media assuming zero incident angle.

In the 1970s, high amplitude anomalies (bright spots) were recognized as gas indicators (Chiburis et al., 1993 and Brown, 2010) . This was an early indication that fluid anomalies could be seen on seismic data (Chiburis et al., 1993). Unfortunately it was later recognized that it is not only gas sands that form bright spots. Hard or tight rocks such as igneous or cemented sedimentary rocks also show as high amplitude anomalies. It is now known that hydrocarbons can also give dim spots or polarity reversals (Fig. 10), (Hilterman and Verm ,1995 and Brown, 2010). Figure 10 shows that these hydrocarbon indicators are caused by changes (at different rates) in acoustic impedance of rocks as you increase depth (or effective pressure) (Brown, 2010).

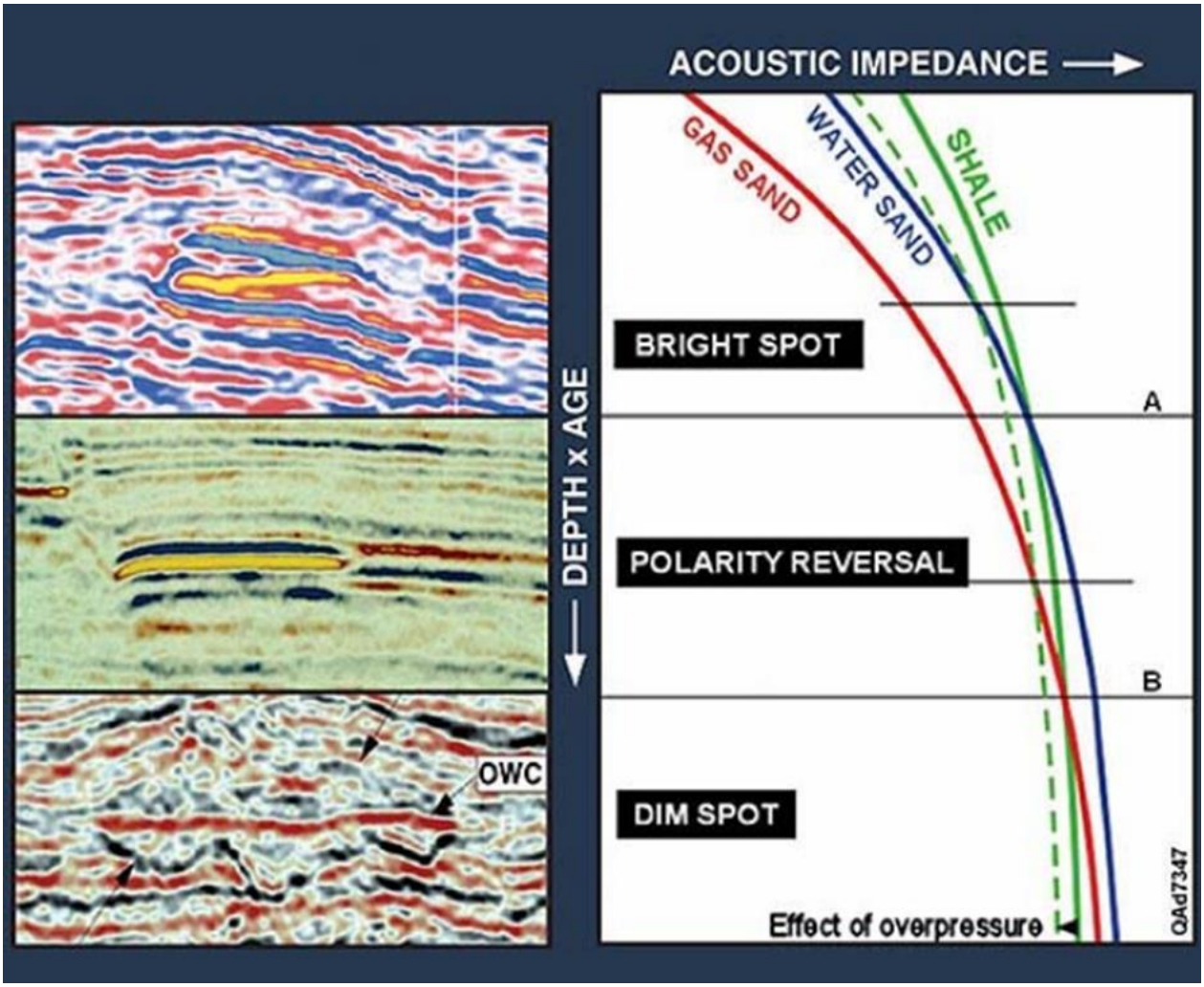

Figure 10: Bright spot, polarity reversal and dim spot. Image from Brown (2010)

1.6.1 Zoeppritz equation and its approximations

When a P-wave hits an interface at an oblique angle ($\theta \neq 0$), some of the incident P-wave energy is converted into shear wave (S-wave) energy. The partitioning between the reflected P-wave, reflected S-wave, transmitted P-wave and transmitted S-wave is described by the Zoeppritz equation (Zoeppritz et al., 1919)**. Snell's law** and **the solutions to the wave equation** are used to produce the Zoeppritz equation (Zoeppritz et al., 1919).

The angle of the reflected P-wave is the same as the incident angle. The angle of the transmitted P-wave can be calculated using Snell's law. For two different media (Fig. 12), Snell's law states that the *sin* of an angle for transmitted wave divided by the velocity of the bottom

layer is equal to the *sin* of an incident angle divided by the velocity of the top layer (see equation below).

The wave equation is a differential equation which describes the acceleration ($\frac{\partial^2 u}{\partial t^2}$) of a particle as a product of its velocity squared (V^2) and the sum of the partial second derivatives $\left(\frac{\partial^2 u}{\partial x^2}+\frac{\partial^2 u}{\partial y^2}+\frac{\partial^2 u}{\partial z^2}\right)$ of the displacement with respect to each dimension of movement (x, y and z).

$$\frac{\sin\theta_2}{V_{P_2}}=\frac{\sin\theta_1}{V_{P_1}}=\frac{sin\,\phi_1}{V_{S_1}}=\frac{sin\,\phi_2}{V_{S_2}} \qquad \text{Snell's law}$$

$$\frac{\partial^2 u}{\partial t^2}=V^2\nabla^2 u=V^2\left(\frac{\partial^2 u}{\partial x^2}+\frac{\partial^2 u}{\partial y^2}+\frac{\partial^2 u}{\partial z^2}\right) \qquad \text{3D Wave equation}$$

$V=$ velocity of the medium, $t=$ time, $u=$ displacement.

$x, y\ and\ z$ are the three dimensions of displacement

The reflection (R_{PP} and R_{PS}) and transmission (T_{PP} and T_{PS}) coefficients associated with transmitted and reflected waves for a specific incident angle (**θ**) can be obtained by solving the Zoeppritz equation (Fig. 12(b)).

The amplitude of the reflected waves is the product of the reflection coefficient (R_{PP} or R_{PS}) and the incident amplitude, for example, if a source generates seismic waves with an initial amplitude of 10, and the reflection coefficient between two media is 0.01 for a specific incident angle, then the reflected wave between the two media will have an amplitude equal to 0.1 (0.01×10) for that angle. The amplitude of the transmitted wave is also the product of the transmission coefficient (T_{PP} and T_{PS}) and the incident amplitude.

(a)

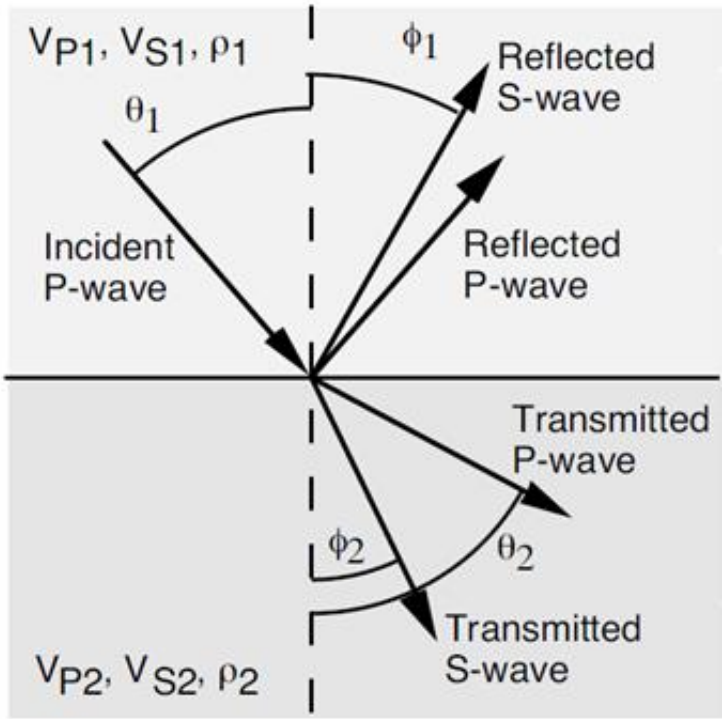

(b)

$$\begin{pmatrix} -\sin\theta_1 & -\cos\emptyset_1 & \sin\theta_2 & \cos\emptyset_2 \\ \cos\theta_1 & -\sin\emptyset_1 & \cos\theta_2 & -\sin\emptyset_2 \\ k_1 I_{S1}\sin 2\theta_1 & I_{S1}\cos 2\emptyset_1 & k_2 I_{S2}\sin 2\theta_2 & I_{S2}\cos 2\emptyset_2 \\ -I_{P1}\cos 2\emptyset_1 & I_{S1}\sin 2\emptyset_1 & I_{P2}\cos 2\emptyset_2 & -I_{S2}\sin 2\emptyset_2 \end{pmatrix} \begin{pmatrix} R_{PP} \\ R_{PS} \\ T_{PP} \\ T_{PS} \end{pmatrix} = \begin{pmatrix} \sin\theta \\ \cos\theta \\ k_1 I_{S1}\sin 2\theta_1 \\ I_{P1}\cos 2\emptyset_1 \end{pmatrix},$$

$$k = \frac{V_S}{V_P}, \qquad I_P = V_P \times \rho, \qquad I_S = V_S \times \rho,$$

V_P = compressional velocity, V_S = shear velocity, **ρ** = density, **θ** = P-wave angle, **ϕ** = S-wave angle, I_S = Shear Impedance and I_P = compressional impedance.

Figure 11: (a) Incident P-wave with reflected and transmitted P and S-waves. (b) Zoeppritz equation.

In general, we are most interested in R_{PP} because R_{PP} data are relatively easy to process and recievers are commonly configured to record the P-wave data. The relative amplitudes of the various phases (i.e. the fraction of incident P-wave energy partitioned into reflected and transmitted P and S waves) is dependent on the angle of incidence. Measuring how reflected P-wave amplitudes vary with increasing offset can provide information about material properties. This is the concept behind the AVO (amplitude variation with offset) or AVA (amplitude variation with angle) methodology. Zoeppritz approximations are used for R_{PP} data, this is to

simplify the maths in the Zoeppritz equation and to get an intuitive understanding of how rock properties affect the reflection coefficient.

Zoeppritz approximations for R_{PP} show clearly how the elastic properties such as velocity relate to reflection coefficient for a region of parameter space (Table 1) (Li at el., 2007).

Zoeppritz approximations	
(a) Shuey (1985)	$R_{PP}(\theta) = R_0 + \left[A_0 R_0 + \left(\frac{\Delta\sigma}{(1-\sigma)^2}\right)\right] sin^2\theta + \frac{1}{2}\frac{\Delta V_P}{V_P}(tan^2\theta - sin^2\theta)$
(b) Hilterman and Verm (1995)	$R_{PP}(\theta) = \frac{1}{2}\left[\frac{\Delta V_P}{V_P} + \frac{\Delta\rho}{\rho}\right] cos^2\theta + \left[\frac{\Delta\sigma}{(1-\sigma)^2}\right] sin^2\theta$ $\sigma = poisons\ ratio$
(c) Smith and Gidlow (1987)	$R_{PP}(\theta) = \left[\frac{\Delta V_P}{V_P}\right]\left[\frac{1}{2}(1 + tan^2\theta) + g\left(1 - 2\left(\frac{V_S}{V_P}\right)^2 sin^2\theta\right)\right]\left[\frac{\Delta V_S}{V_S}\right]\left[4\left(\frac{V_S}{V_P}\right)^2 sin^2\theta\right]$ $\rho = aV_P^g$
(d) Aki and Richards (1980) rearranged	$R_{PP}(\theta) = \frac{1}{2}\left[\frac{\Delta V_P}{V_P} + \frac{\Delta\rho}{\rho}\right] - 2\left(\frac{V_S}{V_P}\right)^2\left[2\frac{\Delta V_S}{V_S} + \frac{\Delta\rho}{\rho}\right] sin^2\theta + \frac{1}{2}\frac{\Delta V_P}{V_P} tan^2\theta$
(e) Gidlow et al. (1992)	$R_{PP}(\theta) = \frac{1}{2}\left[\frac{\Delta I_P}{I_P}\right](1 + tan^2\theta) - 4\left(\frac{V_S}{V_P}\right)^2\left[\frac{\Delta I_S}{I_S}\right] sin^2\theta - \frac{\Delta\rho}{\rho}\left(\frac{1}{2} tan^2\theta - 2\left(\frac{V_S}{V_P}\right)^2 sin^2\theta\right)$
Table 1: Approximations of the Zoeppritz solution for R_{PP}.	

Figure 13 shows a plot of amplitude vs the incident angle (θ) for Zoeppritz et al. (1919) and 3 term approximations (top) for Gidlow et al. (1992), Hilterman and Verm (1995) and Shuey (1985) for up to 60 degrees and the 2 term approximations (bottom) up to 30 degrees . For two term approximations, the third term in Table 1 is eliminated from the equations. The 3 term Shuey (1985) and Gilow et al. (1992) match the Zoeppritz equation up to 30 degrees. Their corresponding two term equations are a very good approximation for angles less than 30 degrees.

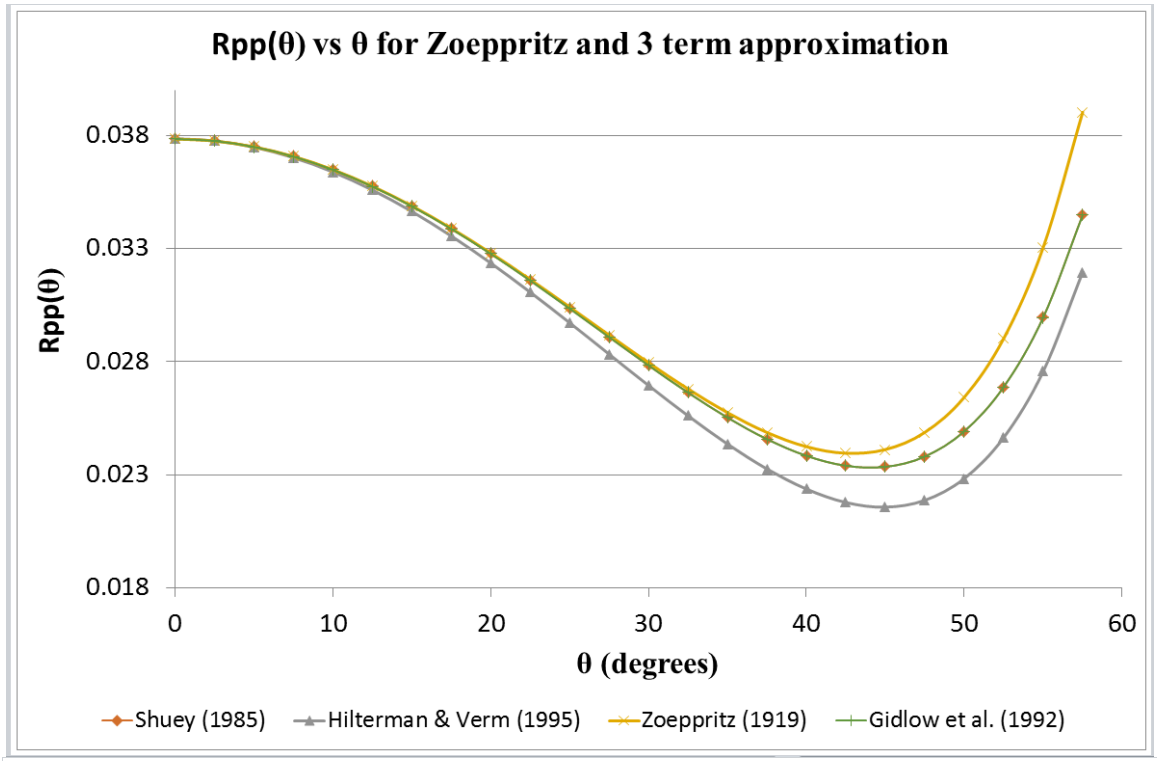

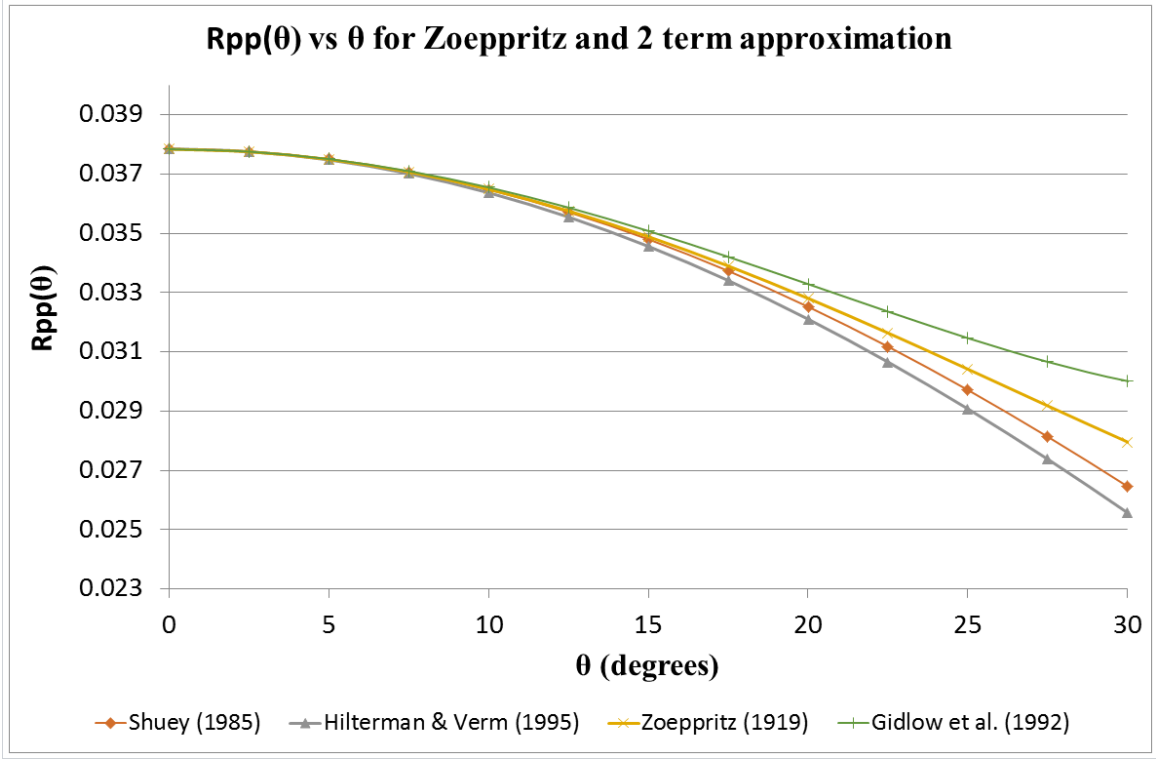

Figure 12: A plot of amplitude vs the incident angle for the Zoeppritz equation (1919), Gidlow et al. (1992), Hilterman and Verm (1995) and Shuey (1985) for 2 and 3 term equations.

1.6.2 AVO classes

In the 1980s, with the improvement of seismic processing, focus shifted from amplitude anomalies within a stacked seismic section to how the amplitude of a reflection from a single point varied with offset (AVO). Rutherford and Williams (1989) defined three classes of AVO anomalies for gas sand overlain by shale. The classes are based on the zero offset (normal incident) reflection coefficient at the top of a gas sand (Fig. 11). Class 1 occurs when the zero offset reflection coefficient between the gas sand and shale is strongly positive and decreases with increasing offset. Class 2 occurs when the zero offset reflection coefficient is closer to zero (slightly positive or negative) and becomes more negative as the offset increases. Positive reflection coefficients have a phase change (positive to negative) and become more negative as the offset increases. Class 3 occurs when the zero offset reflection coefficient is strongly negative and become more negative as the offset increases.

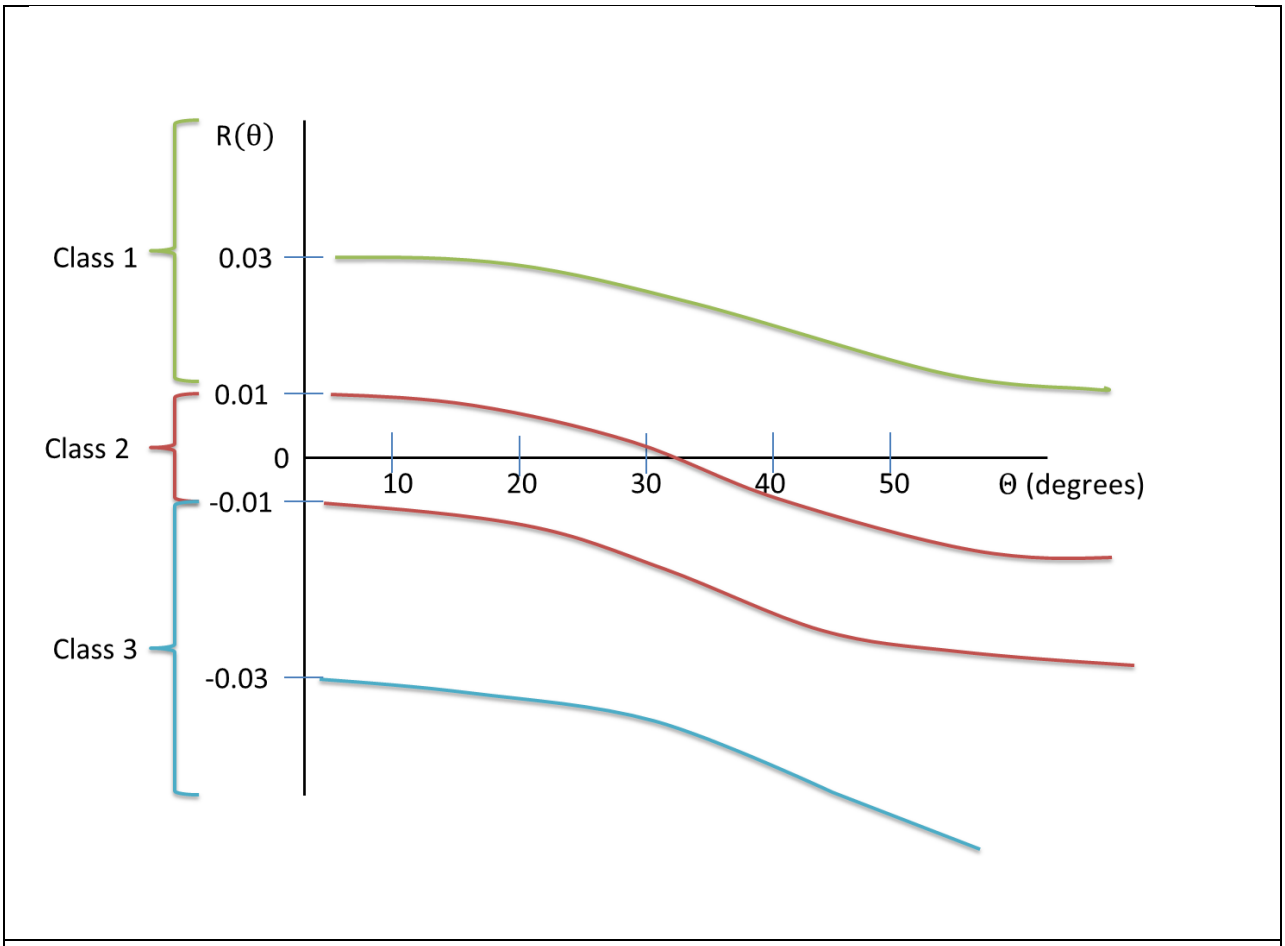

Figure 13: Gas sand classes defined by Rutherford and Williams (1989).

1.6.3 An introduction to seismic intercept and gradient concept of AVO

As seen above, Zoeppritz approximation equations (e.g Shuey, 1985), can be simplified to a two term linear equation ($R_{PP}(\theta) = R_P + Gsin^2\theta$) with respect to $sin^2\theta$ (Shuey, 1985), with the approximation that $sin^2\theta \approx tan^2\theta$ for angles less than 30 degrees. The assumption is made that $\frac{V_P}{V_S} \approx 2$, which is the case for most water saturated reservoirs at depth (≈ 2000-2500m offshore) where we usually find oil.

It is possible to plot a graph of $R_{PP}(\theta)$ vs $sin^2\theta$ and fit a straight line through the data points for a specific time. R_P is the seismic intercept (zero angle approximation) and *G* is the seismic gradient of a line through the points (Fig. 14(a)). Note that the amplitudes displayed in Figure 14 are proportinal to $R_{PP}(\theta)$ (the reflection coefficient).

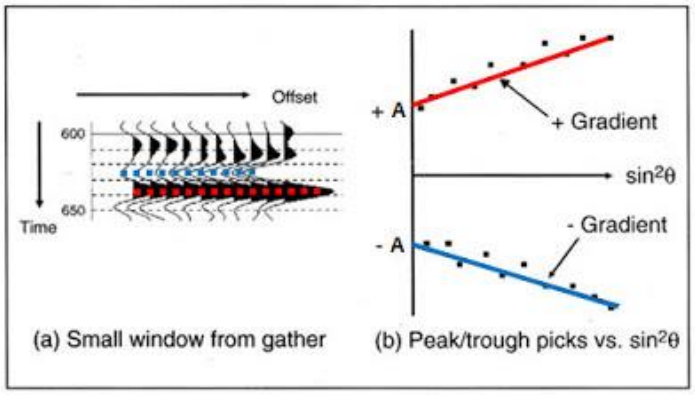

(a)

$$R_{PP}(\theta) = \frac{1}{2}\left[\frac{\Delta V_P}{V_P} + \frac{\Delta\rho}{\rho}\right] - 2\left(\frac{V_S}{V_P}\right)^2\left[2\frac{\Delta V_S}{V_S} + \frac{\Delta\rho}{\rho}\right]sin^2\theta + \frac{1}{2}\frac{\Delta V_P}{V_P}tan^2\theta$$

$$V_P = \frac{V_{P_2} + V_{P_1}}{2}, \qquad \rho = \frac{\rho_2 + \rho_1}{2}, \qquad V_S = \frac{V_{S_2} + V_{S_1}}{2}, \qquad \Delta Vp = V_{P_2} - V_{P_1},$$

$$\Delta V_S = V_{S_2} - V_{S_1}, \qquad \Delta\rho = \rho_2 - \rho_1$$

$$R_{PP}(\theta) \approx R_P + Gsin^2\theta \text{ (for angles less than 30 degrees)}$$

$$G \approx 2\left(\frac{V_S}{V_P}\right)^2\left[2\frac{\Delta V_S}{V_S} + \frac{\Delta\rho}{\rho}\right] + \frac{1}{2}\frac{\Delta V_P}{V_P}, \qquad R_P \approx \frac{1}{2}\left[\frac{\Delta V_P}{V_P} + \frac{\Delta\rho}{\rho}\right]$$

θ = incident P-wave angle and **Δ** = change

(b)

Figure 14: (a) Amplitude variation with Offset (AVO). (b) Aki and Richards approximation and its simplification.

The intercept and gradient are very useful products for seismic analysis. For example, a cross-plot of R_P vs *G* will show a trend line (background trend) associated with shales and water saturated rocks, with hydrocarbon saturated rocks deviating away from the trend (Fig. 15). These anomalies are defined by Castagna and Swan (1997) (Fig. 16).

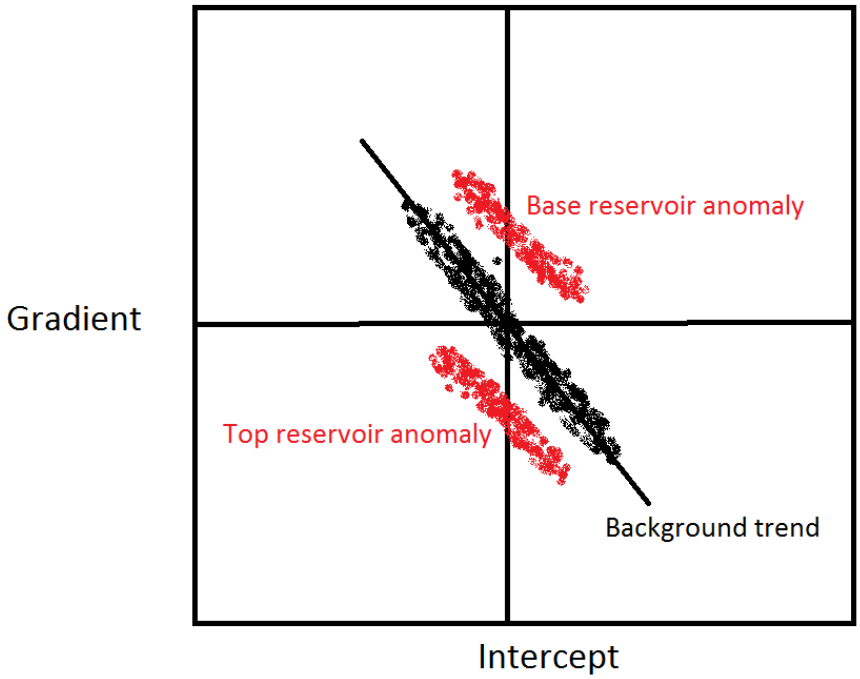

Figure 15: A cartoon showing a cross-plot of Intercept and gradient along with top and base reservoir hydrocarbon anomalies.

1.6.3.1 AVO classes in the intercept and gradient cross-plot.

Castagna and Swan (1997) suggested that hydrocarbon sands should be classified based on their location on the intercept (R_P) and gradient (*G*) cross-plot. They define 4 classes (Class 1, Class 2, Class 3 and Class 4) (Fig. 16). Castagna and Swan (1997) defined the classes based on the Intercept and Gradient points for the top of the hydrocarbon sands. In a cross-plot of intercept and gradient, hydrocarbon sands move away from the background trends formed by water saturated sands and shales. For hydrocarbons sands, Class 1 has a positive intercept and a negative gradient, as in Rutherford and Williams (1989). Class 2 has an intercept closer to zero but the gradient is negative, as in Rutherford and Williams (1989). Class 3 has a negative intercept and a negative gradient and Class 4 has negative intercept and positive gradient.

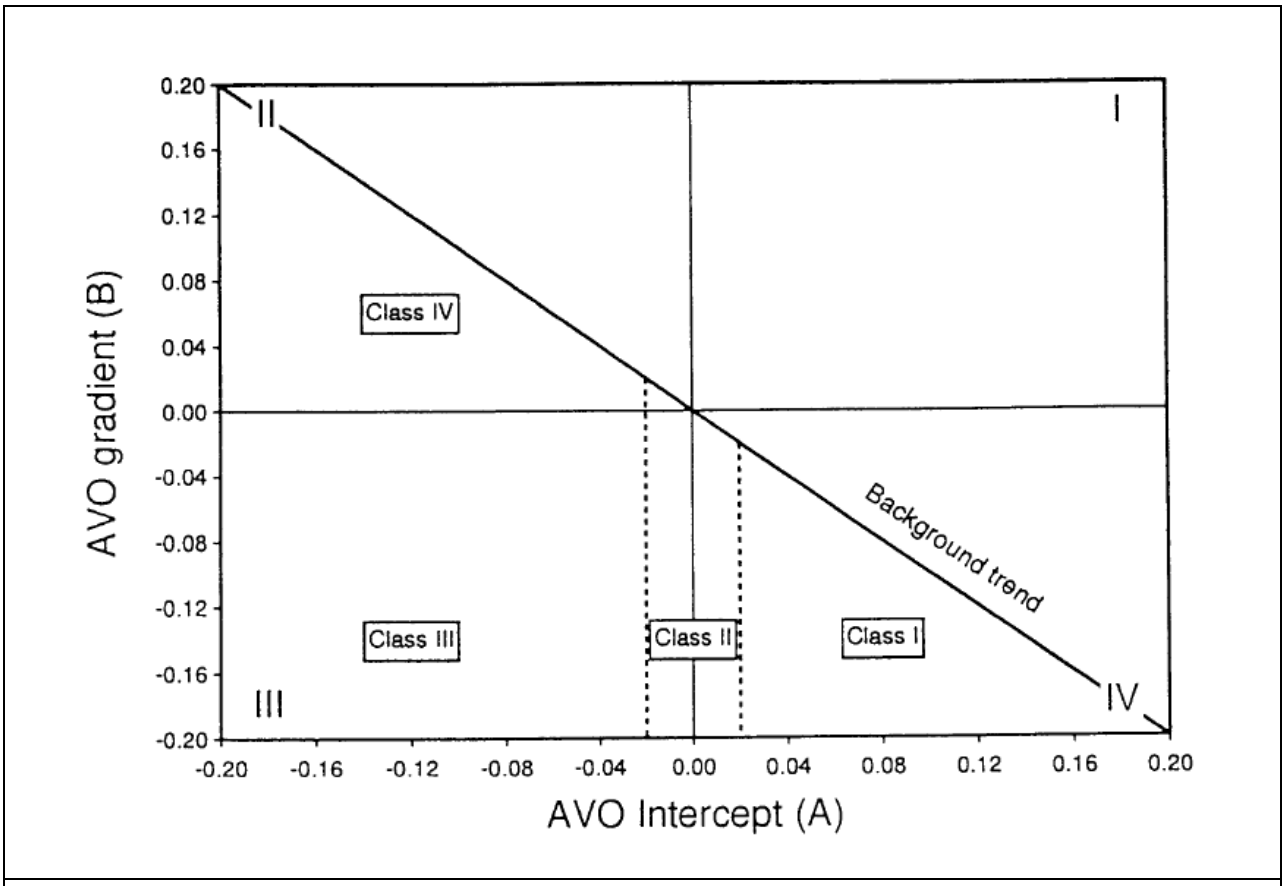

Figure 16: Hydrocarbon sand classes defined by Castagna and Swan (1997).

1.6.3.2 Extended Elastic Impedance (EEI)

Connolly, 1999 defined Elastic Impedance as:

$$EI(\theta) = V_P^a V_S^b \rho^c \qquad \text{Eq.1}$$

$$\boldsymbol{a} = 1 + tan^2\theta, \qquad \boldsymbol{b} = -8\left(\frac{V_S}{V_P}\right)^2 sin^2\theta \qquad and \qquad \boldsymbol{c} = 1 - 4\left(\frac{V_S}{V_P}\right)^2 sin^2\theta$$

In terms of reflectivity data, relative EI is:

$$EI\ (\theta)\ = R_P + \ Gsin^2(\theta) \qquad \text{Eq.2}$$

Appendix A2 shows how Equation 2 is obtained from Equation 1. Connolly (1999) noticed that at some other angles, the EI correlate with other rock properties. The problem with EI is that it does not scale correctly for other angles, meaning a scalar is required to match the EI and some rock properties. This is because the exponents (a, b and c) keep increasing as the angle theta

increases leading to different dimensions for every angle. Another problem is that EI are only valid for 0 to 30 degrees of incident angle (θ) because this is the angle range (0° to 30°) where we see the linear relationship between $R_{PP}(\theta)$ or *EI(θ)* and $sin^2(\theta)$. Mathematically, EI is valid up to 90 degrees (0 to 1 for $sin^2(\theta)$). Beyond 90 degrees it was noticed that EI also correlate with other rock properties.

Whitcombe et al. (2002) introduced normalization constants ($V_{P_0}, V_{S_0}, \ and \ \rho_0$) into the EI equation to eliminate the scaling problem. They replaced $sin^2\theta$ by $\tan\chi$. Chi (χ) is the angle between the gradient axis and a straight line which represent the background trend. This was called Extended Elastic Impedance (EEI) and is shown below. The EEI is defined in the range -90 to +90 degrees and -∞ to +∞ for $\tan\chi$.

$$EEI(\chi) = V_{P_0}\rho_0\left[\left(\frac{V_P}{V_{P_0}}\right)^p\left(\frac{V_S}{V_{S_0}}\right)^q\left(\frac{\rho}{\rho_0}\right)^r\right] \qquad \text{Eq.3}$$

$$p = cos\chi + sin\chi$$
$$q = -8Ksin\chi$$
$$r = cos\chi - 4Ksin\chi$$

$V_{P_0}, V_{S_0}, \ and \ \rho_0$ are normalization constants.

For reflectivity data (seismic), relative EEI can be defined using intercept and gradient (Fig. 17), which are the seismic intercept and gradient traces respectively, with -90° phase rotation applied. In terms of intercept and gradient, relative EEI can be written as:

$$EEI(\chi) = R_P cos(\chi) + Gsin(\chi) \qquad \text{Eq.4}$$

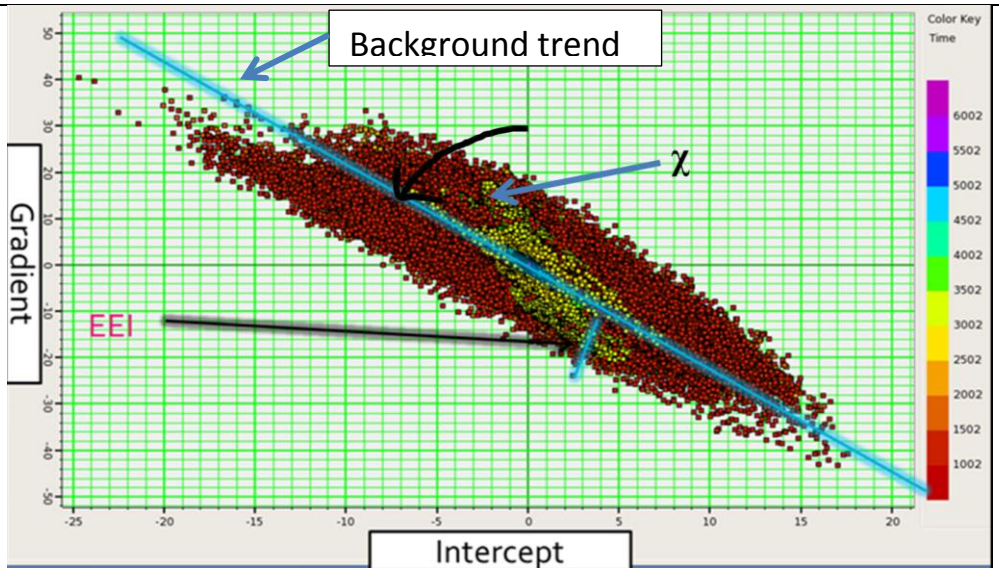

EEI is the shortest distance of each point from a straight line defined by angle Chi (χ).

Figure 17: Intercept and gradient cross-plot showing the Chi angle and the EEI concept.

EEI can be viewed as a perpendicular distance from a point to a straight line defined by χ. EEI and AVO classes are widely used in the oil and gas industry. EEI are useful because they correlate with elastic properties of rocks or AVO attributes (Table 2). EEIs are also correlated with rock properties that are not elastic, for example, clay volume, saturation, etc.

Rock Interval Property	**AVO Attribute**	**χ**
P-Impedance	R_P	0°
S-impedance	R_S	-45°
λ (lambda)	$\Delta\lambda/\lambda$	18°
μ (Mu)	$\Delta\mu/\mu$	-45°
V_P/V_S		45°
Gradient	G	90°
Fluid Factor	ΔF	22°
Table 2: Chi angle with corresponding AVO attributes and rock properties. Msolo and Gidlow (2015).		

μ = shear modulus, λ = K - 2/3μ = Lames modulus

1.6.4 An introduction to 4D seismic analysis

During exploration, hydrocarbon prospects are identified by recognizing favourable structural and stratigraphic settings along with direct hydrocarbon indicators (AVO behavior) from acquired seismic data (Simm and Bacon, 2014). Once a prospect has been identified and evaluated (de-risked), the next step is to confirm the existence of hydrocarbon by drilling a well down to the prospect (Simm and Bacon, 2014). If the drilled target proves to be commercial, the prospect will be developed to a producing field with one or more producing wells.

During production, hydrocarbons are replaced by water, which means the oil water contact (OWC) moves up towards the top of the accumulation. This movement of the OWC is caused by the reduction in pore pressure during production and it provides a way to monitor a producing field due to the changing AVO behavior (Saul and Lumley, 2015 and Sunday et al., 2012). Monitoring a field is important for field development because it gives ideas on where to put an injection well if the hydrocarbons are not swept well enough or where to put another producing well if there are virgin areas that have not been produced (Sunday et al., 2012).

When monitoring a field, the first seismic survey is used as a base survey and it provides the initial state of the field before production (Simm and Bacon, 2014). Two, three, four or more years after production, a second (monitor) survey is acquired in the same way as the base

survey and processed in the same way. After processing, the two seismic data are subtracted from each other to produce seismic difference volumes which indicate areas that show significant changes during the production time frame (Simm and Bacon, 2014). These changes may be caused by a number of things; the most significant are pressure changes and fluid saturation changes (Sunday et al., 2012 and Simm and Bacon, 2014). When hydrocarbons are produced, oil or gas is removed and is replaced by water from the aquifer. This happens because the pore pressure drops in the area of production and the fluid migrates from high pore pressures to low pore pressures.

The changes described above will only be visible on seismic data if the changes are bigger than the random noise in the data i.e. the seismic amplitudes are bigger than the noise received by seismic receivers such as geophones and/or hydrophones. The changes in seismic data are caused by changes in elastic properties such as velocity, because changing the fluid type and effective pressure changes the rock elastic properties. The changes seen on seismic data are a combination of saturation and pressure changes. Replacing oil with a small (0.1 saturation) amount of gas will produce changes in the subsurface that can be seen on seismic data because gas has a very low density and bulk modulus. Replacing oil with water might not be so clearly observed using seismic data because oil and water have similar density and bulk modulus. An effective pressure increase might not be easier to see on seismic whereas a decrease of the same amount might be visible (Landrø and Kvam, 2002). The reason is that when we increase effective pressure the bulk modulus does not change as much as it does when we decrease effective pressure by the same amount because the sensitivity of the rock decreases as the effective pressure increases i.e. the rock becomes incompressible. The values above are rough estimates from studies carried out in the literature and might change depending on the location of the study area. It is also worth mentioning that an increase in water saturation and an increase in pore pressure (decrease in effective pressure) have an opposite effect on elastic parameters. This means we might not see any changes in seismic data for an increase in pore pressure combined with an increase in water saturation.

The analysis of the data of a specific field at different times is called 4 dimensional seismic analysis. In 4 dimensional (4D) analysis, the four dimensions are x, y, z and time . x and y are surface coordinates for the location of the field, z is the depth and time represents the production time frame between two seismic surveys.

Figure 18 shows a North Sea example of a producing field (Simm and Bacon, 2014). The 1993 baseline data in Figure 18 shows clearly the oil water contact (OWC) but in 1998 the OWC is not clearly seen, this is because the oil water contact moves upward as the oil is produced.

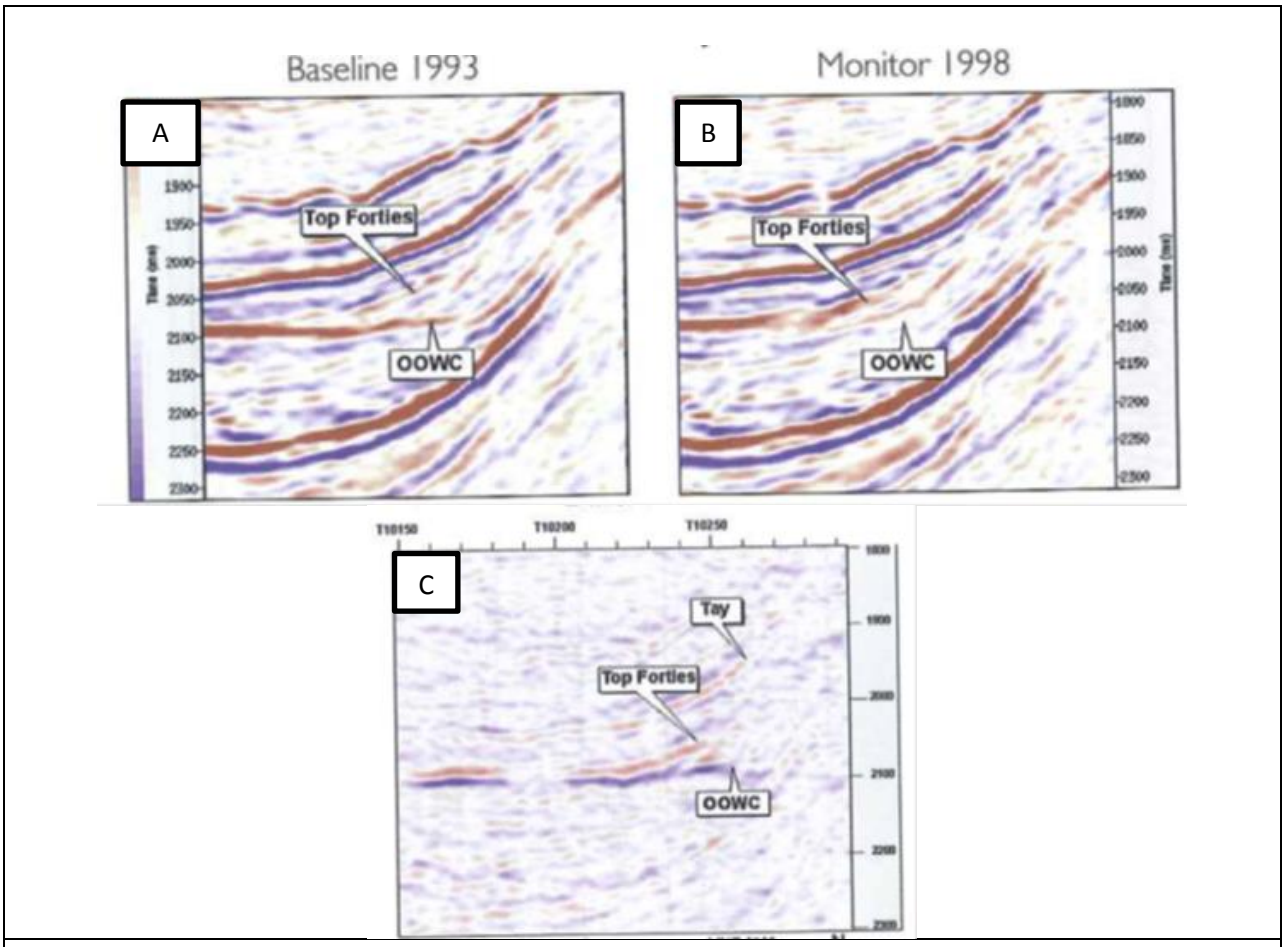

Figure 18: North Sea example showing (a) Baseline seismic in 1993, (b) monitor seismic in 1998 and (d) the difference between baseline and monitor seismic. Red = Peaks (or positive) and Blue = troughs (or negative). Image from Simm and Bacon (2014).

1.6.4.1 Landrø's intercept and gradient technique.

During production, we know we have saturation and pressure changes in the reservoir. Ideally, those changes would be quantified because they provide information about areas were hydrocarbons are removed and where we have high or low pore pressures. Landrø (2001) proposed a technique using seismic intercept and gradient data with the Aki and Richards AVO approximation equation (Eq. 5), to determine pressure and saturation changes from seismic data.

The AVO equation (Eq.5) gives the reflection coefficient at the interface as a function of compressional velocity, shear velocity and density for PP (compressional incident wave to compressional reflected wave) waves. Landrø (2001) showed that the change in reflectivity (or reflection coefficient) associated with changes in fluid saturation is given by Equation 6, with the assumption that the shear modulus does not change when changing fluid saturation. The

superscript (F) in $\Delta {V_P}^F$ indicates velocity change caused by fluid saturation change. Landrø (2001) also showed that the change in reflectivity associated with effective pressure change can be written as shown by Equation 7; here the assumption is that the density of the rock has a negligible change when changing pressure. The total change in reflectivity as a result of effective pressure and saturation changes is the sum of Equation 6 and 7.

$$R_{PP}(\theta) = \frac{1}{2}\left[\frac{\Delta V_P}{V_P} + \frac{\Delta \rho}{\rho}\right] - 2\left(\frac{V_S}{V_P}\right)^2 \left[2\frac{\Delta V_S}{V_S} + \frac{\Delta \rho}{\rho}\right] sin^2\theta + \frac{1}{2}\frac{\Delta V_P}{V_P} tan^2\theta \quad \text{Eq.5}$$

$$\Delta {R_{PP}}^F(\theta) \approx \frac{1}{2}\left[\frac{\Delta {V_P}^F}{V_P} + \frac{\Delta \rho^F}{\rho}\right] + \frac{1}{2}\frac{\Delta {V_P}^F}{V_P} tan^2\theta \quad \text{Eq.6}$$

$$\Delta {R_{PP}}^P(\theta) \approx \frac{1}{2}\left[\frac{\Delta {V_P}^P}{V_P}\right] - 4\left(\frac{V_S}{V_P}\right)^2 \left[\frac{\Delta {V_S}^P}{V_S}\right] sin^2\theta + \frac{1}{2}\frac{\Delta {V_P}^P}{V_P} tan^2\theta \quad \text{Eq.7}$$

ΔS = water saturation changes, ΔP = effective pressure changes, $\Delta {V_P}^F$ = changes inP-wave velocity due to changes in saturation (fluid) and $\Delta {V_P}^P$ = changes in P-wave velocity due to changes in effective pressure

Landrø (2001) used a second order polynomial to describe the relationship between velocity change and effective pressure change (see Eq.8) and a first order polynomial equation to express the relationship between water saturation changes and velocity changes (as well as density) (Eq. 8). The linear constant for saturation is derived by fitting a linear equation to repeated logging data at different water saturation or by modeling. In Landrø (2001) the constants for effective pressure changes vs velocity changes are derived by fitting a second order polynomial to ultrasonic core measurements at different effective pressures.

$$\frac{\Delta V_P}{V_P} \approx \frac{\Delta {V_P}^F}{V_P} + \frac{\Delta {V_P}^P}{V_P} \approx k_{vp}\Delta S + l_{vp}\Delta P + m_{vp}\Delta P^2 \quad \text{Eq.8(a)}$$

$$\frac{\Delta V_S}{V_S} \approx \frac{\Delta {V_S}^F}{V_S} + \frac{\Delta {V_S}^P}{V_S} \approx k_{vs}\Delta S + l_{vs}\Delta P + m_{vs}\Delta P^2 \quad \text{Eq.8(b)}$$

$$\frac{\Delta \rho}{\rho} \approx k_\rho \Delta S \quad \text{Eq.8(c)}$$

Substituting Equation 8(a), 8(b) and 8(c) into the sum of Equation 6 and 7 results in Equation 9. Equation 9 expresses the change in reflectivity in terms of the change in effective pressure and water saturation. Using the conventional equation for AVO intercept and gradient ($R_{PP}(\theta) = R_P + Gsin^2\theta$), the change in intercept is given by the first term and the change in gradient is given by the sum of the second and third terms (Eq. 10 and 11). Note that $sin^2\theta \approx tan^2\theta$ for small (<30 degrees) angles.

$$\Delta R_{PP}(\theta) \approx \frac{1}{2}\left[k_{vp}\Delta S + l_{vp}\Delta P + m_{vp}\Delta P^2 + k_\rho \Delta S\right] - 4\left(\frac{V_S}{V_P}\right)^2 [l_{vs}\Delta P + m_{vs}\Delta P^2]sin^2\theta + \frac{1}{2}\left[k_{vp}\Delta S + l_{vp}\Delta P + m_{vp}\Delta P^2\right]tan^2\theta \quad \text{Eq.9}$$

$$\Delta R_P \approx \frac{1}{2}\left[k_{vp}\Delta S + l_{vp}\Delta P + m_{vp}\Delta P^2 + k_\rho \Delta S\right] \quad \text{Eq.10}$$

$$\Delta G \approx \frac{1}{2}\left[k_{vp}\Delta S + l_{vp}\Delta P + l_{vp}\Delta P^2\right] - 4\left(\frac{V_S}{V_P}\right)^2 [l_{vs}\Delta P + m_{vs}\Delta P^2] \quad \text{Eq.11}$$

The change in intercept and the change in gradient can be generated from seismic data; as a result, solving the two equations produces an expression for both effective pressure and water saturation changes (Eq.12 and Eq.13). Using Landrø's method, Equation 12 and 13 can be used to estimate changes associated with effective pressure and water saturation separately.

$$\Delta P \approx \frac{-\boldsymbol{b}-\sqrt{\boldsymbol{b^2}-4\boldsymbol{ac}}}{2\boldsymbol{a}} \quad \text{Eq.12}$$

$$\boldsymbol{a} = m_{vp} - \frac{8{V_S}^2}{{V_P}^2}m_{vs} - \frac{m_{vp}k_{vp}}{k_{vp}+k_\rho}, \qquad \boldsymbol{b} = l_{vp} - \frac{8{V_S}^2}{{V_P}^2}l_{vs} - \frac{k_{vp}l_{vp}}{k_{vp}+k_\rho}, \qquad \boldsymbol{c} = \frac{2k_{vp}\Delta R_P}{k_{vp}+k_\rho} - 2\Delta G$$

$$\Delta S \approx \frac{1}{k_{vp}+k_\rho}\left(2\Delta R_P - l_{vp}\Delta P - m_{vp}\Delta P^2\right) \quad \text{Eq.13}$$

1.6.4.2 Pressure and saturation changes from EEI.

Pressure and saturation changes can be estimated from EEI. Smith et al. (2010) modeled the changes in water saturation and reservoir pore pressure for different wells from the Enfield oil field in North West shelf of Australia. Figure 19 shows the results of their model. From the graph, the relationship between ΔR_P and ΔG is approximately linear and is a weighted sum of changes in intercept and gradient. This means from the slope (*tan(χ))* of a cross-plot of ΔR_P vs ΔG, we can calculate the angle χ (the angle between the gradient axis and a line perpendicular to the saturation or pressure trend) for a line perpendicular to the saturation or pressure trend. A perpendicular distance away from this line defined by the angle χ would indicate saturation or pressure changes (Fig. 20). This means from the rock physics model we can calculate the angle (χ) which correlate with changes in saturation or pressure. If we know the angle (χ) that correlate with saturation changes, we can use that angle to calculate the EEI that correlate with

saturation before production, this way we can compare the saturation before and after production to search for areas that have no production effect and propose new wells in those areas.

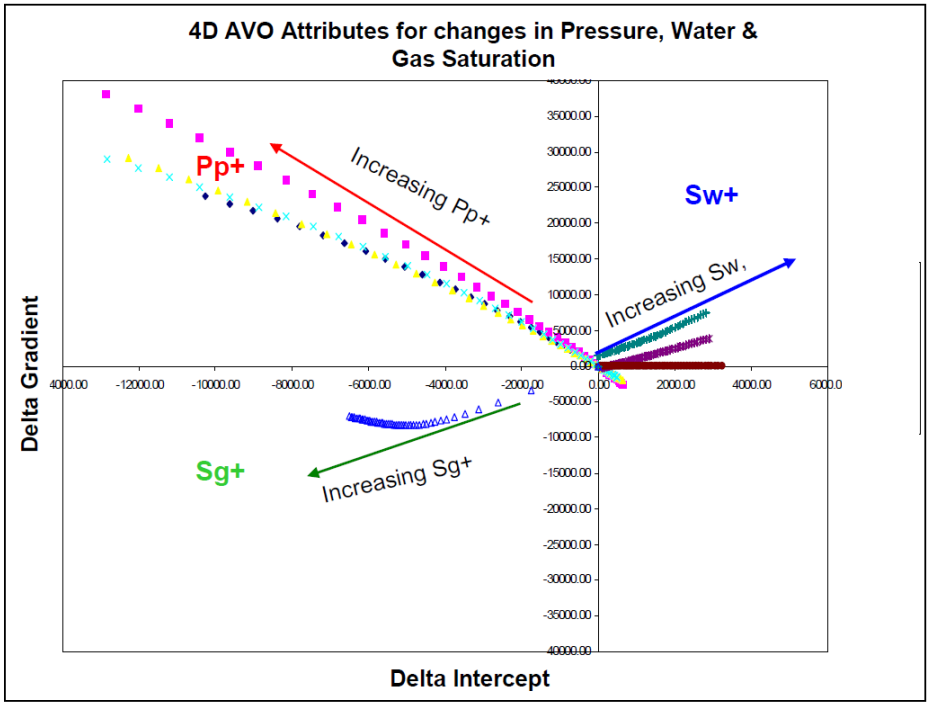

Figure 19: ΔR_P vs ΔG for different saturation and pressure changes. Image from Smith et al. 2010.

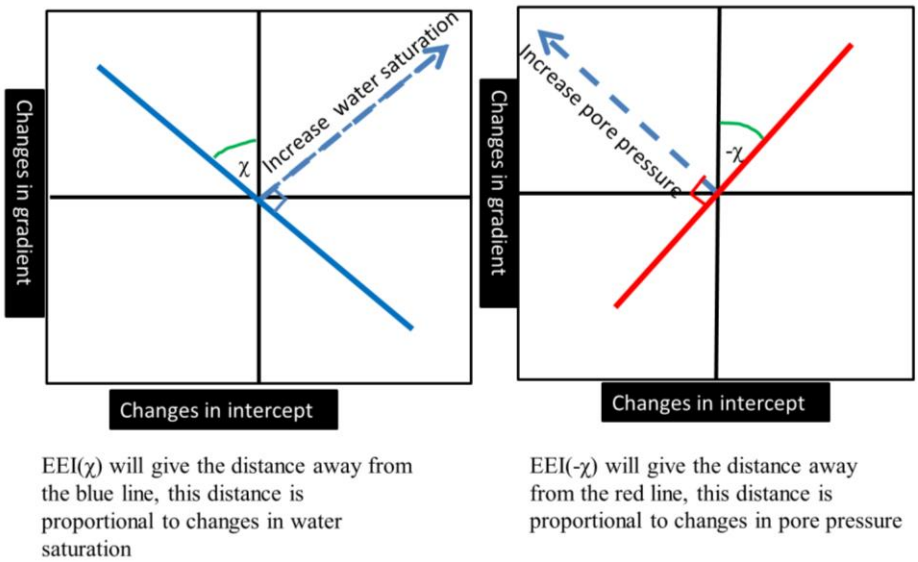

Figure 20: Cartoon showing EEI for saturation and pressure changes on ΔR_P vs ΔG cross-plot.

Landrø (2001) showed that ΔSw ≈ 8(ΔR_P +ΔG) and ΔP ≈ 23ΔR_P -35ΔG for the Gullfaks field. For saturation changes, we can make $cos(\chi) = 8\ and\ sin(\chi) = 8$ (see Eq.4), therefore $\tan\chi = 1$ (χ = 45°). This suggest that ΔEEI(45°) or Δ(V_P/V_S) will correlate with changes in water saturation. For pressure changes, we can make $cos(\chi) = 23\ and\ sin(\chi) = -35$, therefore $\tan\chi = -1.52$ (χ = -57°) and therefore ΔEEI(-57°) will correlate with effective pressure changes. This is expected because when changing water saturation in a rock, we also change the V_P/V_S ratio. We also know that V_P/V_S maybe affected by pressure changes. When we change the pressure in a rock, we also change V_P and V_S. If we look at Figure 21 (MacBeth et al., 2002), we see that at low effective pressures (less than 20MPa), the V_P/V_S ratio changes as we change effective (confining) pressure. At pressures above 20MPa, the V_P/V_S remains constant when we change effective pressure.

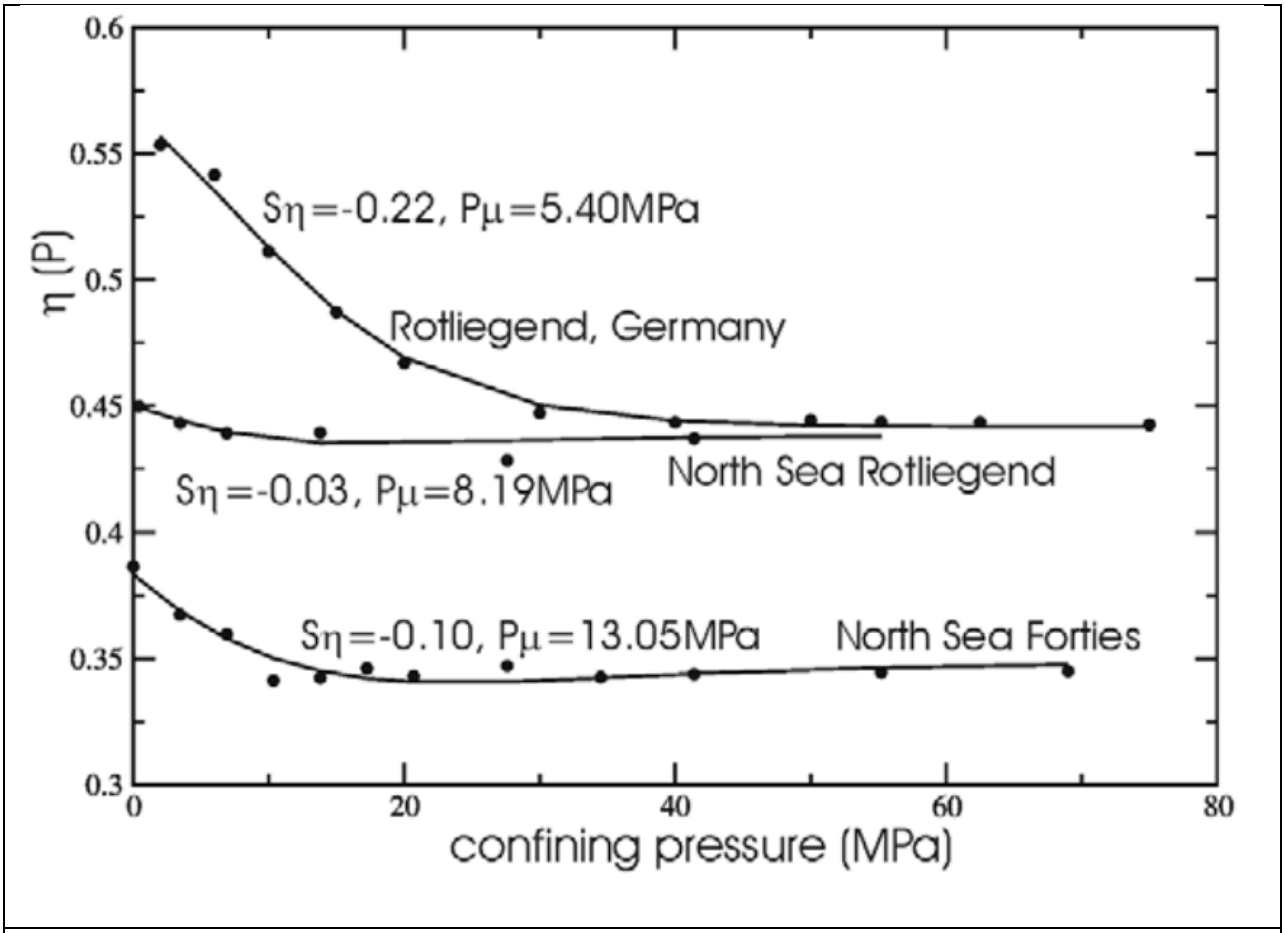

Figure 21: η(P) vs confining (effective) pressure. η(P) = (V_S/V_P)^2. Image from MacBeth et al. (2002)

This means, for effective pressures above 20MPa, ΔEEI(45) might be a good indicator of saturation changes because it is not affected by effective pressure changes, while at low effective pressures, ΔEEI(45°) might not be a good indicator of saturation changes. So, we can conclude that if we working on high effective pressures, ΔSw can correlate with ΔEEI(45°) while at low effective pressures ΔSw can correlate with any chi angle.

Figure 22 is a plot of V_P/V_S vs effective pressure from Han et al. (1986) and Freund (1992), These samples are described in more details in Chapter 2. Again, we see that for some samples (Han sample 1 and 4 and Freund sample 218), the V_P/V_S ratio become constant around 25MPa. The behavior of the velocity ratio with pressure explains why EEI(45) correlates with changes in saturation in some fields when doing reservoir monitoring (4D analysis).

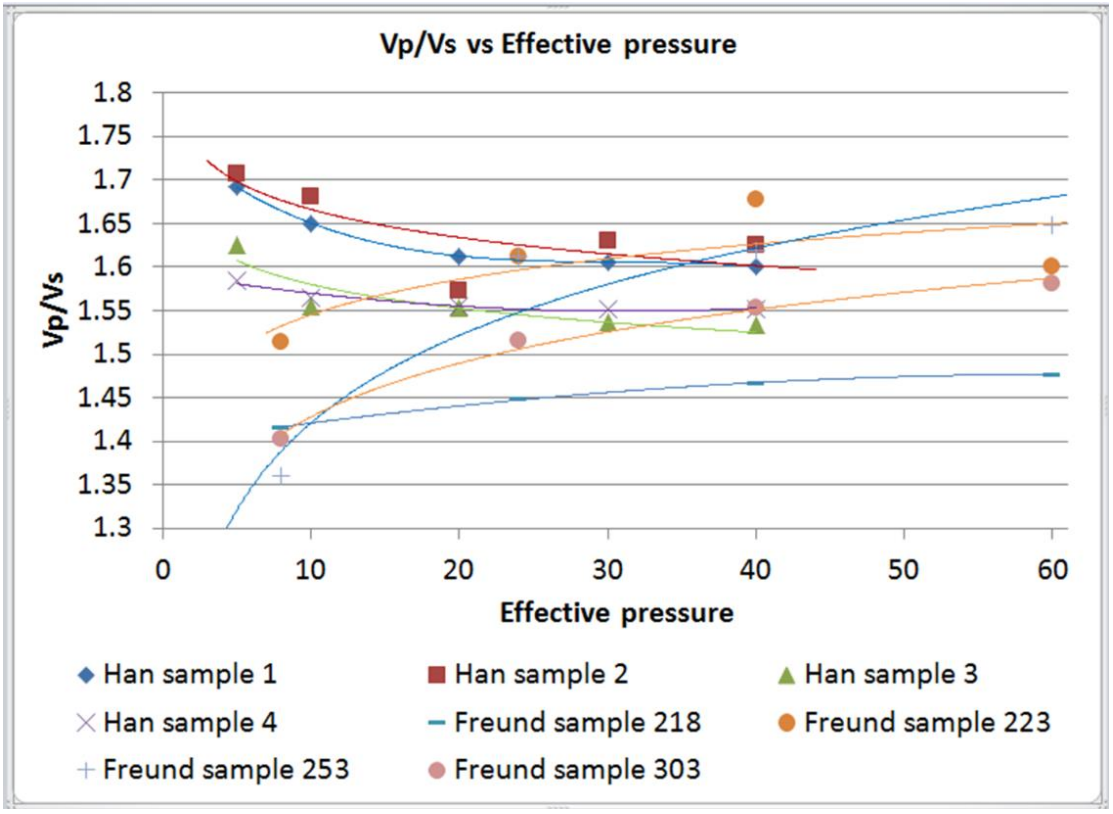

Figure 22: V_P/V_Sratio vs Effective Pressure for clean sands. Data from Han et al. (1986) and Freund (1992).

In conclusion, changes in saturation and pressure can be estimated by a weighted sum of intercept and gradient changes. This means in a spectrum of EEI from -90 to 90 degrees, one of the ΔEEI is effective pressure changes and one is water saturation changes. We can generate ΔEEI from seismic intercept and gradient changes.

Summary of previous sections and where to go from here

I explained that the structures we see on seismic data depend on the reflection coefficient (**section 1.6**). When an incident wave hits an interface at an oblique angle, the reflection coefficient associated with compressional wave can be obtained by solving the Zoeppritz equation (**section 1.6.1**). We generally use the Zoeppritz approximations because they are simplified and they give an intuitive understanding of how amplitude changes when an incident angle changes. The variation of amplitudes with offset (angle) gives rise to the intercept and gradient concept (**section 1.6.3**). Hydrocarbon anomalies can be classified into different classes depending on their position on the intercept and gradient cross-plot (**section 1.6.3.1**). In 4D seismic analysis we use AVO intercept and gradient data with an AVO approximation equation (Aki and Richards) to estimate saturation and pressure changes (**section 1.6.4.1**). Saturation and pressure changes can be estimated from Extended Elastic Impedance (EEI) by calculating the χ angle of a line perpendicular to the pressure or saturation trend (**section 1.6.3.2** and **section 1.6.4.2**).

The question at this point is how to find the pressure and saturation trends (or chi angle) on the intercept and gradient cross-plot. In addition to this question, we want to know how to estimate the constants (k_{vp}, l_{vp}, m_{vp},k_{vs}, l_{vs},m_{vs} and k_{ρ}) in Equation 8 associated with pressure and saturation changes. The answer to these questions is rock physics modeling. The next section will discuss rock physics in more details.

1.6.5 Rock physics modeling

We are interested in pressure and saturation changes, so we need models to relate velocities and density to pressure and saturation. Changes in fluid saturation result in changes in effective bulk modulus and density of the rock which changes the velocities of the rock (MacBeth, 2004, Russell, 2013 and Mavko et al., 2009). The effective bulk and shear moduli both change when effective pressure changes and this leads to changes in velocities of the rock. Rock physics modeling provide the means of modeling these changes. The following sections will explain in more detail how the bulk and shear modulus (and density) changes when adding different material, fluid or changing pressure and how those changes can be modeled.

1.6.5.1 Voigt upper bound and Reuss lower bound

If we wish to determine the seismic velocity of a material made up of different materials (grains, pores, fluid, etc), we need to determine the effective bulk and shear modulus of the material because the velocity is a function of density, effective bulk and effective shear modulus. We also need to specify the proportion of each material, and the geometrical arrangement of those materials (Mavko et al., 2009).

$$V_P = \sqrt{\frac{K + \frac{4}{3}\mu}{\rho}}$$

$$V_S = \sqrt{\frac{\mu}{\rho}}$$

V_P = P-wave velocity, V_S = S-wave velocity, ρ = density, K = effective bulk modulus and μ = effective shear modulus.

If we know the bulk modulus and the proportion of each material with no knowledge of the geometrical arrangements of these materials, we can only calculate the effective bounds (Voigt upper bound and Reuss lower bound) within which the effective moduli will fall, i.e. we can calculate the lowest effective modulus (Reuss lower bound) and the highest effective modulus (Voigt upper bound) (Reuss, 1929). The true effective modulus will be between these values and will depend on the geometric details of the material.

Voigt upper bound (K_V) for N constituents or material is given as:

$$K_V = \sum_{i}^{N} f_i K_i$$

K_V = Voigt effective bulk modulus, K_i = Bulk modulus of each constituent and f_i = Proportion of each constituent.

The Reuss lower bound (K_R) is:

$$\frac{1}{K_R} = \sum_{i}^{N} \frac{f_i}{K_i}$$

K_R = Reuss effective bulk modulus, K_i = Bulk modulus of each constituent and f_i = Proportion of each constituent.

The Voigt upper bound imposes the principle of iso-strain because all the materials (soft and hard) undergo the same strain. For example, if you have a softer material inside a harder material, the harder material will assist the softer material to resist deformation and this will result in both materials having the same strain. The Reuss lower bound imposes the principle of iso-stress because the materials will have the same stress. For example, if you have a harder material inside a softer material, the softer material will deform more to accommodate the same stress as the harder material.

Voigt and Reuss bounds give an allowed range of the effective modulus. When an estimate is needed (in modeling), Voight-Reuss-Hill average is used. Voight-Reuss-Hill average is the average of Voigt and Reuss bounds for a specific proportion.

$K_{VRH} = \frac{K_V + K_R}{2}$ Voigt-Reuss-Hill average

1.6.5.2 Hashin and Shtrikman bounds.

Hashin-Shtrikman bounds are used to get elastic bounds that are narrower than the Voigt and Reuss bounds. Hashin-Shtrikman bounds do not requires any information about the geometries of the mixed materials or constituents (Hashin and Shtrikman, 1963). For a mixture of two (K_1 and K_2) isotropic elastic materials, the Hashin–Shtrikman bounds for their bulk and shear moduli (*K*) are given by:

$$K^{HS\pm} = K_1 + \frac{f_2}{(K_2 + K_1)^{-1} + f_1(K_1 + 4\mu_1/3)^{-1}}$$

$$\mu^{HS\pm} = \mu_1 + \frac{f_2}{(\mu_2 + \mu_1)^{-1} + 2f_1(K_1 + 2\mu_1/3)\left(5\mu_1(K_1 + 4\mu_1/3)\right)^{-1}}$$

K_1 = Bulk modulus of the first constituents, K_2 = Bulk modulus of the second constituents, f_1 = Volume of the first constituent, f_2 = Volume of the second constituent, μ_1 = Shear modulus of the first constituent and μ_2 = Shear modulus of the second constituent.

K^{HS+}(The upper bound) is calculated when the stiff material is K_1 in the above equations and K^{HS-} (the lower bound) is calculated when K_1 is the soft material.

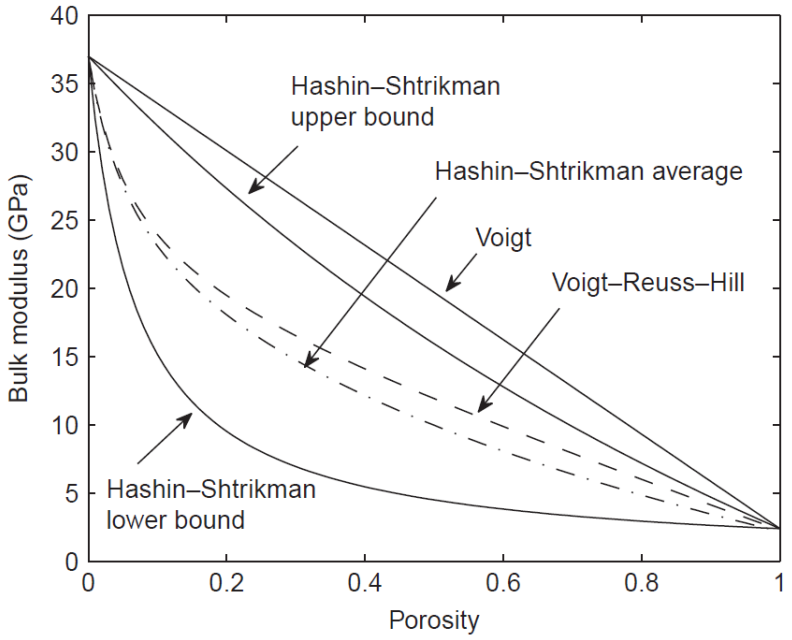

Figure 23: Effective bulk modulus vs volume fraction for a quartz water system ($K_{Quartz} = 37GPa$ and $K_{water} = 2.3GPa$). The Figure also shows the Voigt upper bound, Reuss lower bound, Voigt-Reuss-Hill average and Hashin-Shtrikman bounds. Image from Mavko et al. (2009).

1.6.5.3 Wood's model

For fluids or suspensions (small particles suspended in fluid) where the heterogeneity is small compared to the wavelength of sound, seismic velocities are well defined by Wood's equation (Woods, 1955).

$V_P = \sqrt{\frac{K_W}{\rho}}$ Shear modulus for fluid is zero (μ = 0)

This means for sound velocities in fluid, the effective bulk modulus of N fluid constituents is:

$$\frac{1}{K_W} = \sum_{i=1}^{N} \frac{f_i}{K_i} \qquad \text{Eq.14}$$

K_W = Wood's effective bulk modulus, K_i = ith fluid bulk modulus, f_i = ith volume fraction and N = total number of fluid types.

The assumption in Wood's model is that each material is linear elastic and isotropic.

1.6.5.4 Gassmann fluid substitution (modeling fluid saturation changes for seismic frequencies)

When a seismic wave passes over a rock which contains pore fluid, an increment of pore pressure is induced. This induced pore pressure resists the compression of the rock as the wave passes. The Gassmann equation (Eq.15) is used to calculate the resulting effective bulk modulus due to a seismic wave passing over a rock with pore fluid (Gassmann, 1951). Therefore Gassmann's equation relates changes in saturation to bulk modulus of the rock. The fluid bulk modulus (K_f) is first determined; Wood's model is used if there is more than one fluid (Woods, 1955). The saturated bulk modulus of the rock is then calculated. After calculating the saturated bulk modulus, the velocity of the rock is calculated using Equation 16.

$$\frac{K_{sat}}{K_m - K_{sat}} = \frac{K_{dry}}{K_m - K_{dry}} + \frac{K_f}{\phi(K_m - K_f)} \qquad \text{Eq.15}$$

K_{sat} = saturated bulk modulus, K_{dry} = dry rock modulus, K_f = fluid bulk modulus and ϕ = porosity of the rock and K_m = matrix bulk modulus.

$$\left.\begin{aligned} \rho_{\text{sat}} &= \phi\left(\left(1 - S_w\right)\rho_{HC} + S_w\rho_w\right) + \left(1 - \phi\right)\rho_{ma} \\ V_{p(sat)} &= \sqrt{\frac{K_{sat} + \frac{4}{3}\mu_{sat}}{\rho_{sat}}} \\ V_{S(sat)} &= \sqrt{\frac{\mu_{sat}}{\rho_{sat}}} \end{aligned}\right\} \qquad \text{Eq.16}$$

ρ_{sat} = saturated density of the rock, S_w = water saturation, ρ_{HC} = density of hydrocarbon *(oil or gas),* ρ_w =density of water, ρ_{ma} =density of matrix, $V_{p(sat)}$ =saturated p-wave velocity and $V_{S(sat)}$ = saturated s-wave velocity.

The Gassmann's equation assumes low (<125Hz) seismic frequencies (wavelengths that are very large compared to the pore spaces), this means that the fluid in the pore space is able to equilibrate within the pores to accommodate the induced pore pressure due to the passing wave. Gassmann's equation does not work well with laboratory measured data because the frequencies in the lab are usually in the range $10^4 - 10^6$ Hz (sonic to ultrasonic measurements) (Mavko et al., 2009). For this reason, we need to calibrate the velocity data using check shot data before we can use Gassmann's equation. Check shot data is time-depth pairs measured in the borehole by putting geophones at different depth in the borehole and measuring the times of first arrival from a source located approximately at the top of the borehole.

The Gassmann equation assumes homogeneous mineral and fluid properties and that the pores are connected.

1.6.5.5 MacBeth's model (bulk and shear modulus as a function of pressure)

The previous sections showed how the effective modulus may be estimated when two or more materials are combined, but effective pressure changes were not considered. MacBeth (2004) describes how the effective modulus of a dry rock changes when the effective pressure ($\approx$ overburden pressure minus the pore-pressure) is changed. Note that dry rock means there is no fluid in the pore space (not even air).

MacBeth (2004) introduced a three parameter equation (Eq.17 and 18) which describes how the effective pressure (*P*) affects the dry bulk and shear modulus of a rock. V_P and V_S for dry rocks are measured at different effective pressures, the shear modulus is calculated from the measured velocities (assuming that the density does not change with pressure) using Equation 19 (and 15 if the rock is saturated with fluid). A plot of dry shear modulus vs effective pressure is used to determine the three parameters (μ_∞, S_μ and P_μ). These parameters can be used for the whole field if the porosities of the rocks do not change significantly. The same method can be applied for V_P to determine K_∞, S_K and P_K. Rock samples with different porosity will have different parameters.

$$\mu(P) = \frac{\mu_\infty}{1+E_\mu e^{\frac{-P}{P_\mu}}} \quad \text{Where} \quad E_\mu = \frac{S_\mu}{1-S_\mu} \quad \text{and} \quad S_\mu = \frac{\mu_\infty - \mu(0)}{\mu_\infty} \qquad \text{Eq.17}$$

$$K(P) = \frac{K_\infty}{1+E_K e^{\frac{-P}{P_K}}} \quad \text{Where} \quad E_K = \frac{S_K}{1-S_K} \quad \text{and} \quad S_K = \frac{K_\infty - K(0)}{K_\infty} \qquad \text{Eq.18}$$

P_K and P_μ are characteristic pressure constants and carry the information about the pore geometry. For example, large aspect ratio pores will have high values for P_K and P_μ. K_∞ and μ_∞ are high pressure asymptotes when $K(P)$ and $\mu(P)$ are plotted against effective pressure(*P*). S_K and S_μ describes the overall possible variation of $K(P)$ and $\mu(P)$.

$$V_P(P) = \sqrt{\frac{K(P)+\frac{4}{3}\mu(P)}{\rho}} \qquad \text{Eq.19 (a)}$$

$$V_S(P) = \sqrt{\frac{\mu(P)}{\rho}} \qquad \text{Eq.19 (b)}$$

Eq.19

1.6.5.6 Pore space stiffness model (bulk and shear modulus as a function of pressure)

Russell (2013) describes the pore space stiffness model explicitly. The idea behind the pore space stiffness model is that the pore space stiffness ($K_\emptyset$) remains constant at a specific pressure for a range of porosities. This allows the dry rock modulus to be calculated at different porosities (Eq.20). Russell (2013) used a data from Russell and Smith (2007) to show how the pore space stiffness changes with effective pressure (see Eq.21).

$$\frac{1}{K_{dry}} = \frac{1}{K_M} + \frac{\emptyset}{K_\emptyset} \qquad \text{Eq.20}$$

$$\Delta K_\emptyset = 0.027 K_M \frac{\Delta P}{P} \qquad \text{Eq.21}$$

The importance of rock physics modeling is to link the changes in pressure and saturation occurring in the reservoir to elastic parameters (such as velocity) because seismic reflection data can be described using elastic parameters.

The objective of this project is to separate saturation and pressure changes between the 2010 and 1999, 2003 and 1999 and finally between the 2010 and 2003 seismic data from a producing field in West Africa using a technique derived from Landrø (2001). The new technique used in this project arises from the rearrangement of Landrø's technique and is explained in more detail in the following chapter.

Chapter 2: Proposed Methodology

I will show that the changes in seismic intercept (ΔRp) and seismic gradient (ΔG) can be written as a sum of changes in saturation (ΔS) and changes in velocity reflectivity due to pressure $\left(\frac{\Delta {V_P}^P}{V_P}\right)$, shown below.

$$\begin{bmatrix} \Delta G \\ \Delta R_P \end{bmatrix} = \begin{bmatrix} \frac{1}{2}k_{vp} & \frac{p-8r}{2p} \\ \frac{1}{2}k_{vp} + \frac{1}{2}k_\rho & \frac{1}{2} \end{bmatrix} \begin{bmatrix} \Delta S \\ \frac{\Delta {V_P}^P}{V_P} \end{bmatrix}$$

I derived the above equation because I did not have rock samples of the reservoir which led me to modify the method described by Landrø (2001), hereinafter referred to as Landrø's intercept and gradient technique. A detailed derivation is shown below but I will first explain why Landrø's technique will not work for this project.

2.1 Why Landrø's intercept and gradient technique will not work for this project.

The technique proposed by Landrø replaces the changes in velocity reflectivity $\left(\frac{\Delta V_P}{V_P} \text{ and } \frac{\Delta V_S}{V_S}\right)$ and density reflectivity $\left(\frac{\Delta \rho}{\rho}\right)$ in Equation 2 and 3 by polynomials expressing these reflectivities as a function of change in fluid saturation (ΔS) and effective pressure (ΔP) (Eq. 4). Equation 8 is,

$$\frac{\Delta V_P}{V_P} = \frac{\Delta {V_P}^F}{V_P} + \frac{\Delta {V_P}^P}{V_P},$$

$$\frac{\Delta V_S}{V_S} = \frac{\Delta {V_S}^F}{V_S} + \frac{\Delta {V_S}^P}{V_S}$$

$$\frac{\Delta \rho}{\rho} \approx k_\rho \Delta S$$

with $\frac{\Delta {V_P}^F}{V_P} \approx k_{vp}\Delta S$, $\frac{\Delta {V_S}^F}{V_S} \approx k_{vs}\Delta S$, $\frac{\Delta {V_S}^P}{V_S} \approx l_{vs}\Delta P + m_{vs}\Delta P^2$ and $\frac{\Delta {V_P}^P}{V_P} \approx l_{vp}\Delta P + m_{vp}\Delta P^2$

To use Landrøs technique we need to estimate the constants k_{vp}, l_{vp}, m_{vp}, k_{vs}, l_{vs}, m_{vs} and k_ρ. We can do this by modeling $\frac{\Delta {V_P}^F}{V_P}$, $\frac{\Delta {V_S}^F}{V_S}$ and $\frac{\Delta \rho^F}{\rho}$ as a function of ΔS and fit a straight line through the points and determine k_{vp}, k_{vs} and k_ρ (the slope of the line). This can be done using the Gassmann's fluid substitution equation. To determine l_{vp}, m_{vp}, l_{vs} and m_{vs} we have to

take rock samples of the reservoir and measure the velocities (V_P and V_S) at different effective pressures. With the measured velocities we can plot $\frac{\Delta {V_P}^P}{V_P}$ and $\frac{\Delta {V_S}^P}{V_S}$ vs ΔP and fit a second order polynomial which will allow us to determine l_{vp}, m_{vp}, l_{vs} and m_{vs}.

The challenge for this project is that no rock samples of the reservoir are available for determining the constants l_{vp}, m_{vp}, l_{vs} and m_{vs} . Therefore it is necessary to derive a new equation that will be applicable to the data and will not require the rock samples. I have used Landrø's method as a template for this study. However, I modified the methodology. The modification of Landrø's intercept and gradient technique is explained below.

2.2 Modification of Landrø's intercept and gradient technique.

The process starts with Equation 6 and 7. The change in reflectivity caused by saturation changes only can be written as:

$$\Delta {R_{PP}}^F(\theta) \approx \frac{1}{2}\left[\frac{\Delta {V_P}^F}{V_P} + \frac{\Delta {\rho}^F}{\rho}\right] + \frac{1}{2}\frac{\Delta {V_P}^F}{V_P} tan^2\theta \qquad \text{Eq.6}$$

We can replace the changes in velocity and density from Equation 6 by substituting saturation changes (shown below). The constants can be determined by modeling and using Gassmann's fluid substitution equation.

$$\frac{\Delta {V_P}^F}{V_P} \approx k_{vp}\Delta S$$

$$\frac{\Delta {V_S}^F}{V_S} \approx k_{vs}\Delta S$$

$$\frac{\Delta {\rho}^F}{\rho} \approx k_{\rho}\Delta S$$

By substituting the above Equations into Equation 6, the changes in reflectivity caused by saturation changes can be written as show by Equation 22.

$$\Delta {R_{PP}}^F(\theta) \approx \frac{1}{2}\left[k_{vp}\Delta S + k_{\rho}\Delta S\right] + \frac{1}{2}k_{vp}\Delta S tan^2\theta \qquad \text{Eq.22}$$

$$\Delta {R_{PP}}^F(\theta) \approx \Delta S\left(\frac{1}{2}k_{vp} + \frac{1}{2}k_{\rho}\right) + (\Delta S\frac{1}{2}k_{vp}) tan^2\theta \qquad \text{Eq.23}$$

Equation 7 (also shown below) shows the change in reflectivity caused by changes in effective pressure.

$$\Delta {R_{PP}}^{P}(\theta) \approx \frac{1}{2}\left[\frac{\Delta {V_P}^{P}}{V_P}\right] - 4(r)^2\left[\frac{\Delta {V_S}^{P}}{V_S}\right] sin^2\theta + \frac{1}{2}\frac{\Delta {V_P}^{P}}{V_P} tan^2\theta \qquad \text{where } r = \frac{V_S}{V_P} \qquad \text{Eq.7}$$

The total change in reflectivity is the sum of Equation 7 and 23 (Equation 24).

$$\Delta R_{PP}(\theta) \approx \Delta S\left(\frac{1}{2}k_{vp} + \frac{1}{2}k_{\rho}\right) + \left(\Delta S\frac{1}{2}k_{vp}\right) tan^2\theta + \frac{1}{2}\frac{\Delta {V_P}^{P}}{V_P} - 4(r)^2\left(\frac{\Delta {V_S}^{P}}{V_S}\right) sin^2\theta + \left(\frac{1}{2}\frac{\Delta {V_P}^{P}}{V_P}\right) tan^2\theta \qquad \text{Eq.24}$$

For angles less than 30 degrees $sin^2\theta \approx tan^2\theta$. Therefore Equation 24 can be written as,

$$\Delta R_{PP}(\theta) \approx \Delta R_P + \Delta G sin^2\theta \qquad \text{Eq.25}$$

Where, $\Delta R_P = \left(\frac{1}{2}k_{vp} + \frac{1}{2}k_{\rho}\right)\Delta S + \frac{1}{2}\frac{\Delta {V_P}^{P}}{V_P}$ and $\Delta G = \frac{1}{2}k_{vp}\Delta S + \frac{1}{2}\frac{\Delta {V_P}^{P}}{V_P} - 4(r)^2\frac{\Delta {V_S}^{P}}{V_S}$

Castagna et al. (1985 and 1993) showed that for water saturated sands, V_P and V_S have a linear relationship which can be written as:

$$V_P = pV_S + q \qquad \text{Eq.26}$$

Therefore, changes in V_P and V_S are related as shown by Equation 30.

$$\Delta V_P = p\Delta V_S \qquad \text{Eq.27}$$

$$\frac{\Delta V_P}{\Delta V_S}\left(\frac{V_S}{V_P}\right) = p\left(\frac{V_S}{V_P}\right) \qquad \text{Eq.28}$$

$$\frac{\Delta V_P}{V_P} = pr\left(\frac{\Delta V_S}{V_S}\right) \qquad \text{Where } r = \frac{V_S}{V_P} \text{ (for water saturated sands)} \qquad \text{Eq.29}$$

In the presence of hydrocarbons, the above relationship will have a deviation ΔF (the fluid factor) defined by Smith and Gidlow (1987). If the velocities change only due to pressure, Equation 29 can be written as indicated by Equation 30 (next section will elaborate on this). The assumption I made here is that the velocity will change but will still follow the same trend defined in Equation 26, see Figure 25. This is a reasonable assumption and can be seen in log and measure data as shown in Figure 25. I should stress that fluid substitution is not accounted for by Equation 29. Fluid substitution has been accounted for in Equation 23.

$$\frac{\Delta {V_S}^{P}}{V_S} \approx \frac{\Delta {V_P}^{P}}{V_P}\frac{1}{pr} \qquad \text{Eq.30}$$

Substituting Equation 30 into ΔG (Equation 25), the change in gradient can be written as:

$$\Delta G \approx \frac{1}{2}k_{vp}\Delta S + \left(\frac{p-8r}{2p}\right)\frac{\Delta {V_P}^{P}}{V_P} \qquad \text{Eq.31}$$

Using ΔRp (Equation 25) and ΔG (Equation 31) to solve for ΔS and $\frac{\Delta Vp^P}{Vp}$, the solutions are;

$$\begin{bmatrix}\Delta G\\ \Delta R_P\end{bmatrix}=\begin{bmatrix}\frac{1}{2}k_{vp} & \frac{p-8r}{2p}\\ \frac{1}{2}k_{vp}+\frac{1}{2}k_{\rho} & \frac{1}{2}\end{bmatrix}\begin{bmatrix}\Delta S\\ \frac{\Delta V_P{}^P}{V_P}\end{bmatrix} \quad \text{Eq.32}$$

$$\begin{bmatrix}\Delta S\\ \frac{\Delta V_P{}^P}{V_P}\end{bmatrix}=\begin{bmatrix}\frac{1}{2}k_{vp} & \frac{p-8r}{2p}\\ \frac{1}{2}k_{vp}+\frac{1}{2}k_{\rho} & \frac{1}{2}\end{bmatrix}^{-1}\begin{bmatrix}\Delta G\\ \Delta R_P\end{bmatrix} \quad \text{Eq.33}$$

With Equation 33, I showed that the saturation changes and pressure related velocity changes are a weighted sum of intercept and gradient difference volumes if we know p, r, k_{vp} and k_{ρ}. The assumption in this methodology is that velocity changes due to pressure changes will follow the trend defined in Equation 26, which is the case and is evident when V_P is plotted against V_S for reservoir sands at different depth (i.e effective pressures). The changes in saturation (ΔS) show areas where we have water replacing hydrocarbons due to production; and velocity changes $\left(\frac{\Delta V_P{}^P}{V_P}\right)$ show areas where we have pressure changes.

The good thing about this approach is that we do not need rock samples and we get important information that will allow us to continue with the development plan of the field. The changes in velocity $\frac{\Delta V_P{}^P}{V_P}$ we solve for can be interpreted as areas where we have increase or decrease in effective pressure. This method requires p, r, k_{vp} and k_{ρ} (we do not need k_{vs}), therefore we need 5 fewer parameters compared to Landrø (2001).

2.3 Castagna's equation as an effective pressure trend.

In deriving Equation 33, I assumed that if we change pressure only, the changes in V_P and V_S will still follow the trend defined in Equation 26. To test this assumption, I plotted V_P vs V_S for clean sands from Han et al. (1986) and Freund (1992). I took sample 1, 2, 3 and 4 from Han et al. (1986) and sample 218, 223, 253 and 303 from Freund (1992). These samples have V_P and V_S measured at different effective pressures. I expected the samples to plot very close to the trend defined by Castagna.

Figure 24 is a display of V_P vs V_S for clean sands (from Han et al. (1986) and Freund (1992)) at different effective pressures. The four samples from Han et al. (1986) were obtained from a quarry and they have less than 1% clay content and a porosity range from 15.5% to 18.5%. The

samples from Freund (1992) are from a well SALZWEDEL 2/64 in Germany belonging to the Rotliegendes formation at depths of 3340m to 3670m and they have less that 4% clay and less than 11% porosity. Different rock samples are represented by different colours. The line drawn through the samples has a gradient equal to 1.16, Castagna's mudrock line. We can see that the relationship between V_P and V_S at different effective pressures is linear, even though some samples (sample 218, 233, 253 and 303) deviate from Castagna's line at low velocities (red arrow). The reason for this deviation is the fact that Freund's samples were dried unlike Han et al. which were water saturated. This led to low V_P compared to that predicted by the mudrock line. Note that Freud's dry samples also show a linear relationship but we do not deal with dry rocks at the reservoir.

I used the density and dry rock velocities (V_P and V_S) data from Freund (1992) to calculate K_{dry} $\left(K_{dry} = \rho_{dry}({V_P}_{dry}^{\,2} - \frac{4}{3}{V_S}_{dry}^{\,2}\right)$. I used K_{dry} and gassmann's equation to calculate K_{sat}(water saturated) and Equation 16 to calculate saturated density and velocity. When these dry rocks are saturated with water, they plot on the mudrock line (Fig. 25). For saturated samples, we can conclude from the graph that changes in V_P and V_S due to changes in effective pressure still follow the trend defined by Castagna et al. (1985) which is the assumption made above when coming up with Equation 33.

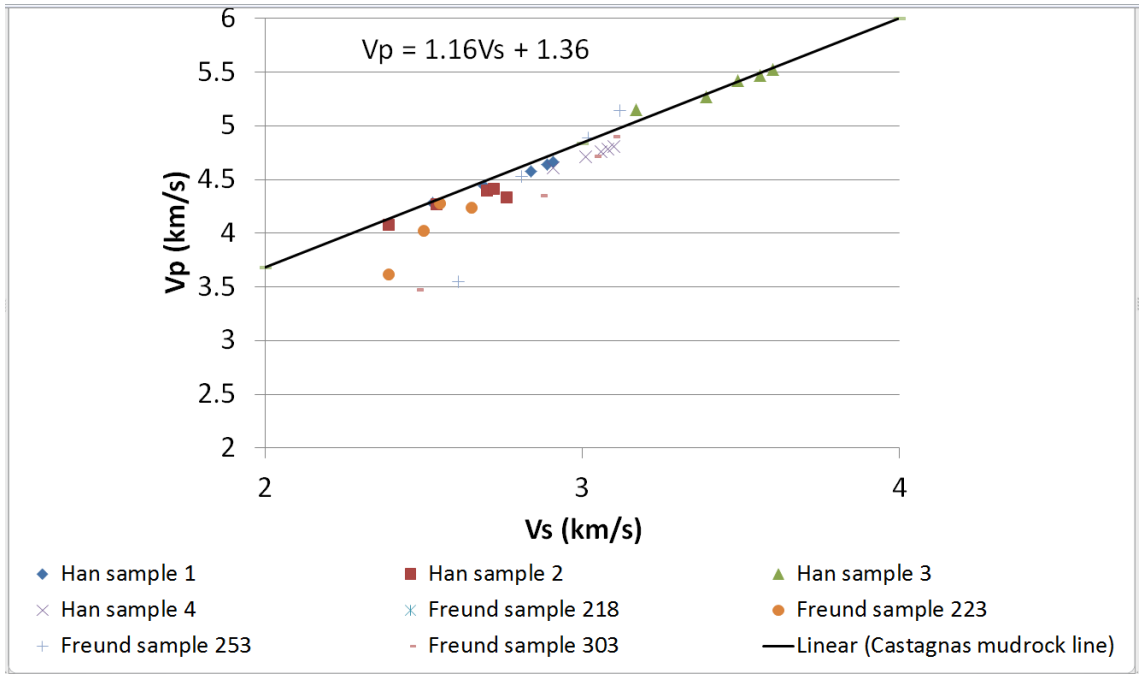

Figure 24: A plot of V_P vs V_S for clean sands at different effective pressures. Data from Han et al. (1986) and Freund (1992). The gradient of the line is 1.16.

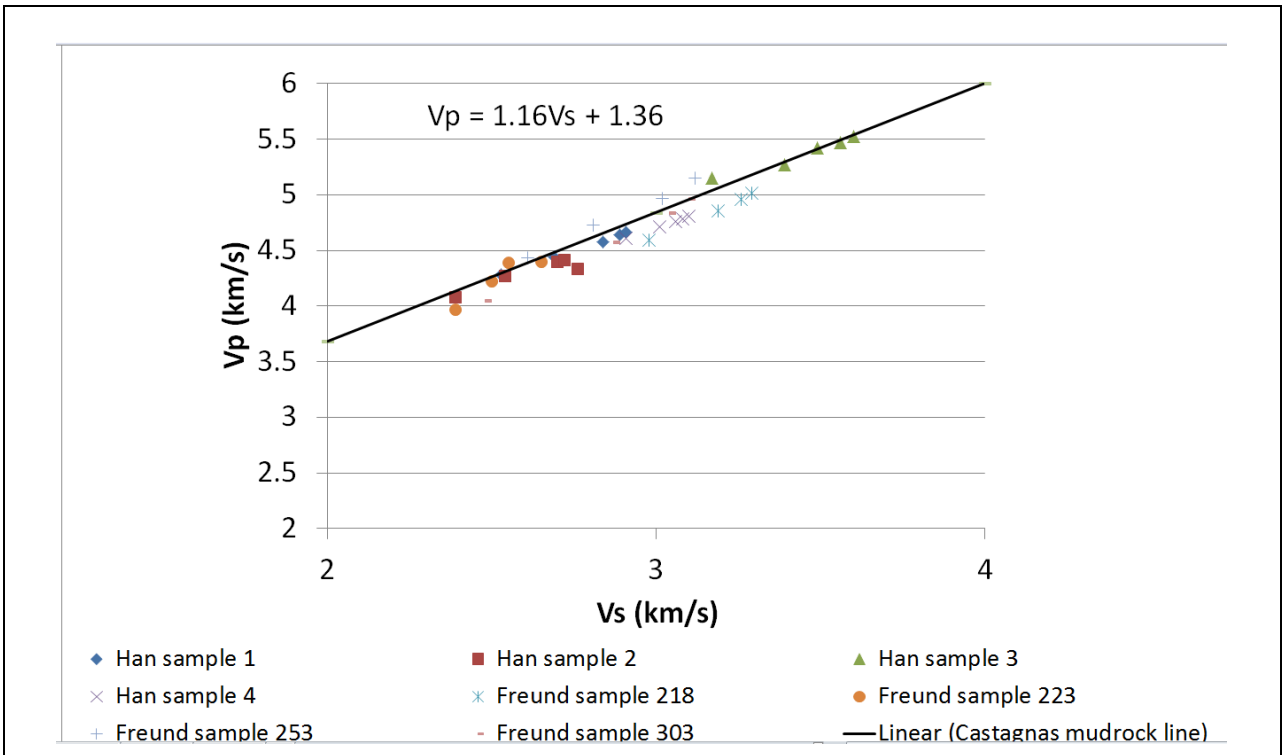

Figure 25: A plot of V_P vs V_S for clean sands at different effective pressures. Data from Han et al. (1986) and Freund (1992). The gradient of the line is 1.16 (mud rock line). Freund samples are saturated with water.

2.4 Proposed methodology validation

Before applying this methodology to West Africa data, I ran a series of synthetic tests. Equation 33 shows that the changes in saturation (ΔS) and the changes in velocity reflectivity due to pressure $\left(\frac{\Delta {V_P}^P}{V_P}\right)$ can be calculated as a weighted sum of changes in intercept and gradient. I created a two layer model to test the solution given by Equation 33. The top layer represents shale and the bottom layer represents a reservoir (Figure 26). I assumed that $V_P = 3300\ m/s$, $V_S = 1800\ m/s$ and $\rho = 2.3\ g/cm^3$ for the top layer. For the bottom layer, I assumed that the porosity is 25% ($\phi = 0.25$) and that the variation of the dry bulk modulus (K_{dry}) and the shear modulus (μ) with effective pressure follows a trend that can be described using MacBeth's three parameter equations (Equation 17 and 18) with $K_\infty = 15\ GPa$, $S_K = 0.75$ and $P_K = 4\ MPa$, $\mu_\infty = 11\ GPa$, $S_\mu = 0.7$ and $P_\mu = 5\ MPa$. The model consists of two parts, the first part is the determination of the changes in intercept and gradient (Figure 26) and the second part is the determination of the constants k_{vp}, k_{vs} and k_ρ (Figure 28).

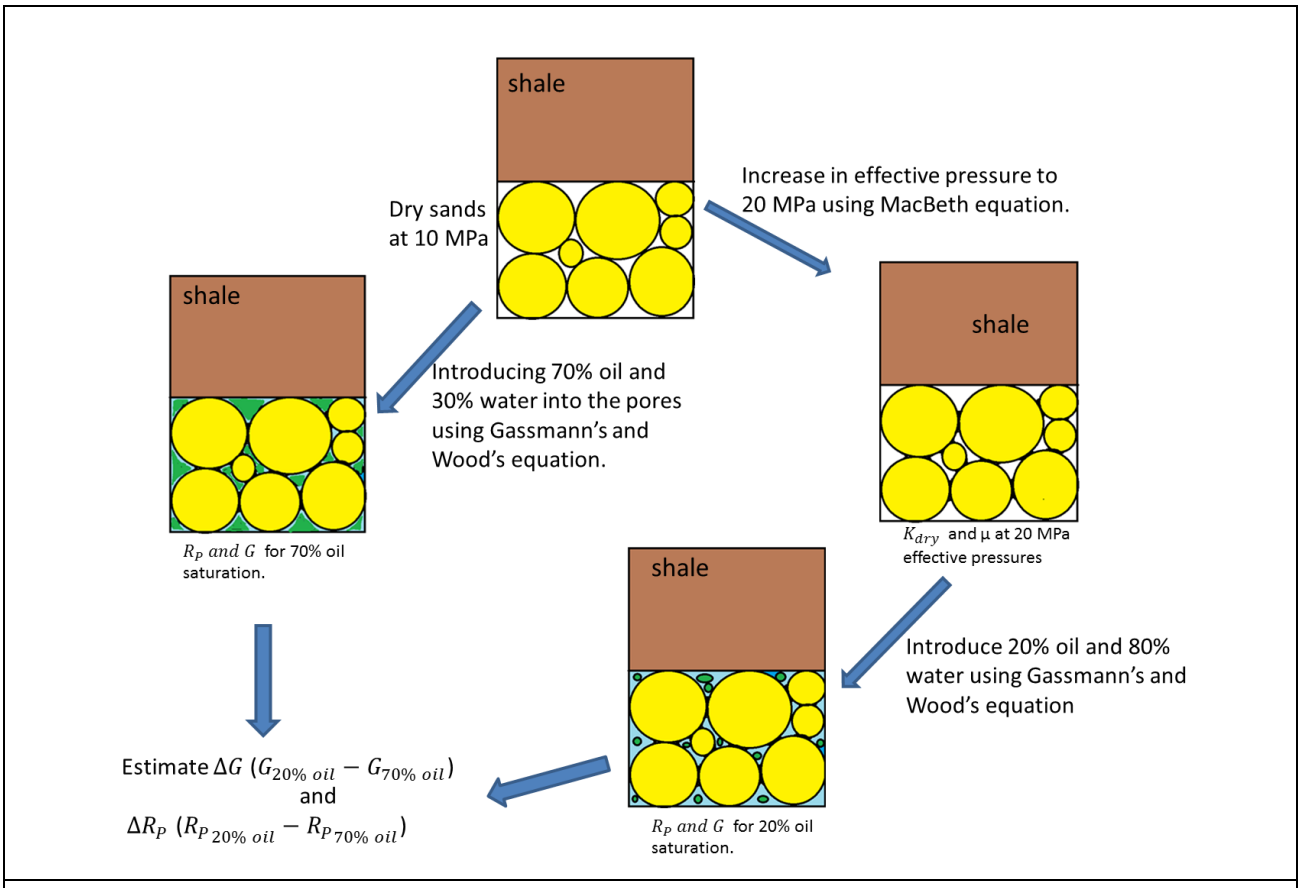

Figure 26: Summarized workflow for determining the changes in gradient (ΔG) and intercept (ΔR_P).

Figure 26 is a summarized workflow for determining the changes in gradient and intercept. Assuming that the initial effective pressure is 10 MPa, I used Equation 17 and 18 to calculate the initial dry bulk modulus and the initial shear modulus. Using the dry bulk modulus at 10 MPa, I introduced 70% oil and 30% water into the pore spaces using Gassmann's equation (Equation 15) and Wood's equation (Equation 14). When introducing oil and water, I assumed that water has a bulk modulus of 2.29 GPa and oil has a bulk modulus of 2 GPa. After introducing 70% oil and 30% water, I used Equation 5 (see also Figure14 (b)) to calculate $R_{PP}(\theta)$ for different incident angles (θ). R_P and G at 70% oil are initial data before production (i.e. when the sands are at 10 MPa of effective pressure and 70% oil in the pore space).

I increased the effective pressure to 20 MPa (i.e. I calculated the dry bulk and shear modulus at 20 MPa). Using the dry bulk modulus at 20 MPa, I introduced 20% oil and 80% water into the pore space using Gassmann's and Wood's equations. After introducing 20% oil and 80% water, I used Equation 5 to calculate $R_{PP}(\theta)$ for different incident angles (θ). R_P and G at 20% oil are final data after production (i.e. when the sands are at 20 MPa of effective pressure and there is

20% oil in the pore space). Note that the effective pressure increased in this model (pore pressure dropped).

I estimated ΔR_P and ΔG from the model above. $\Delta G = G_{20\%\ oil} - G_{70\%\ oil}$ and $\Delta R_P = R_{P\,20\%\ oil} - R_{P\,70\%\ oil}$. The results are shown in Figure 27. Figure 27 shows a plot of R_{PP} vs θ and R_{PP} vs $sin^2\theta$ for θ between 0° to 30° in increments or 2°. I estimated ΔG and ΔR_P from a plot of R_{PP} vs $sin^2\theta$. I fitted a straight line through the points for 10MPa and 20MPa. The gradient of the line is an estimate of G. The difference in *G* between 20MPa and 10MPa is an estimate of ΔG. The intercept of the straight lines with R_{PP} is an estimate of R_P. ΔR_P is the difference in the intercept between 20MPa and 10MPa.

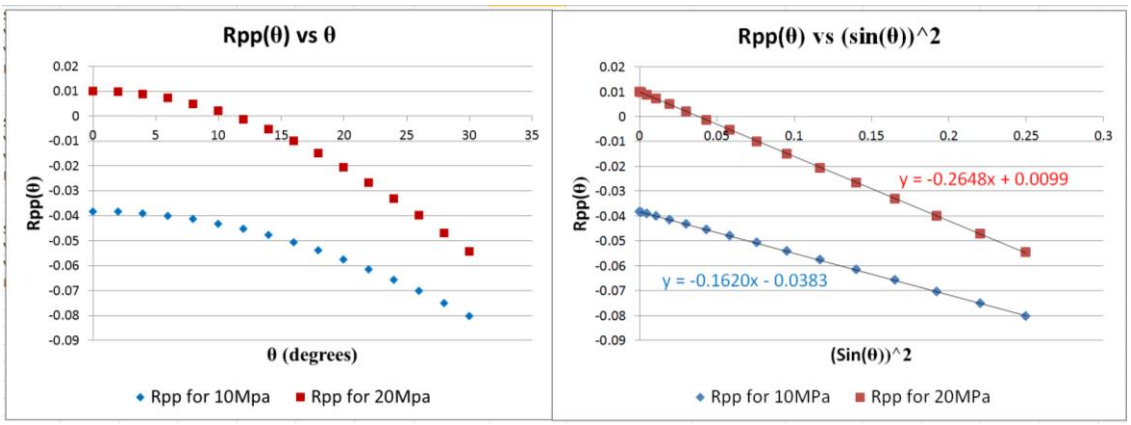

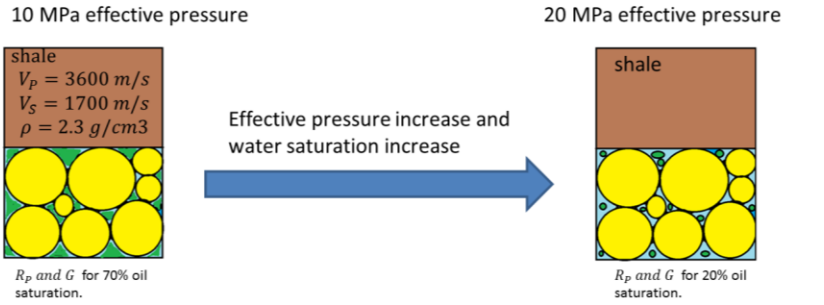

Sands at 10 MPa

$V_P = 3470\ m/s$
$V_S = 1945\ m/s$
$\rho = 2.21\ g/cm3$

	R_P	G
10 MPa	-0.0383	-0.1620
20 MPa	0.0099	-0.2648
	ΔR_P = 0.048	ΔG = -0.1028

Sands at 20 MPa

$V_P = 3754\ m/s$
$V_S = 2161\ m/s$
$\rho = 2.25\ g/cm3$

Figure 27: Estimated ΔG and ΔR_P (from forward modeling) for 10 MPa increase in effective pressure and 0.5 increase in water saturation.

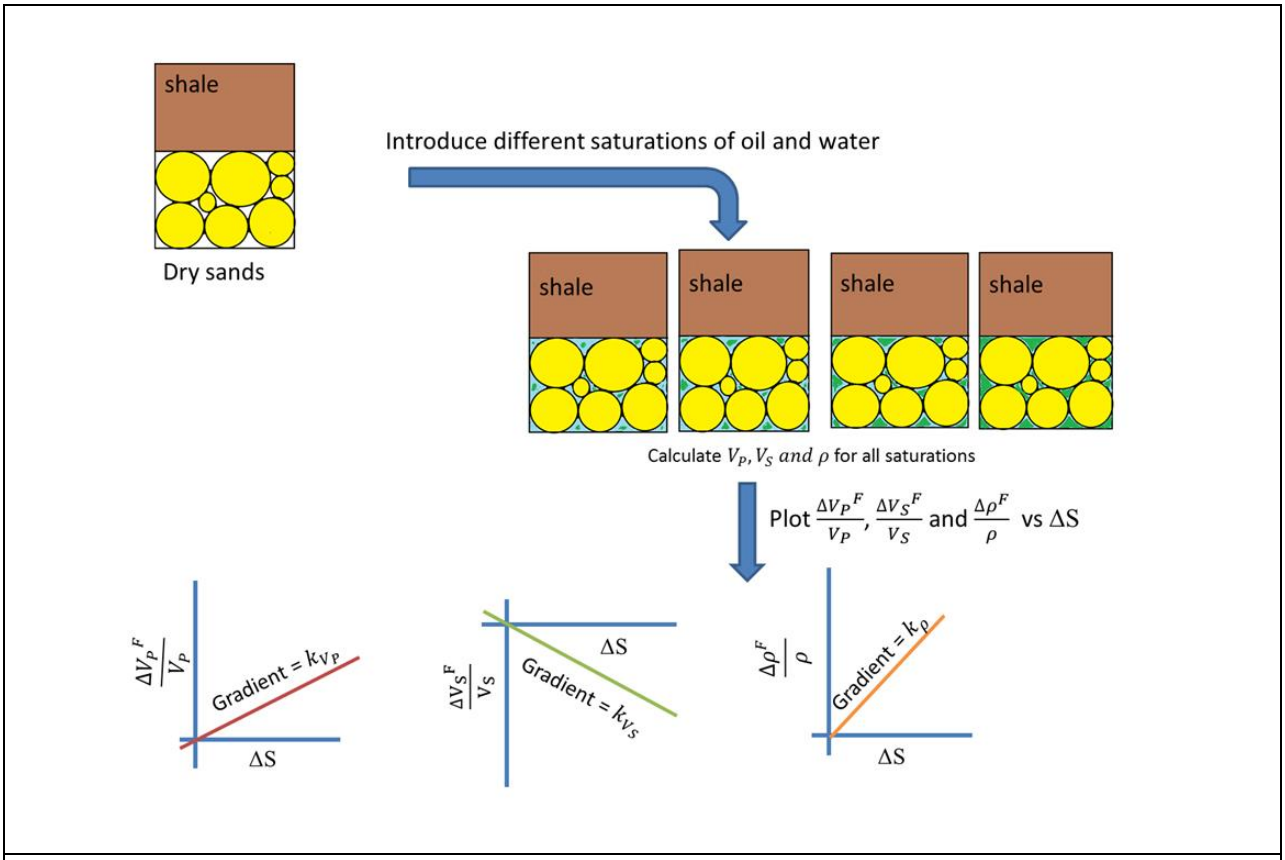

Figure 28: Workflow for estimating k_{vp}, k_{vs} and k_ρ.

Figure 28 shows a second part of this model where I estimated k_{vp}, k_{vs} and k_ρ. To estimate the constants k_{vp}, k_{vs} and k_ρ, I used the dry modulus at 10 MPa and introduced different saturations of oil and water. I calculated and plotted $\frac{\Delta V_P{}^F}{V_P}$, $\frac{\Delta V_S{}^F}{V_S}$ and $\frac{\Delta \rho^F}{\rho}$ vs ΔS .Figure 28 shows the results. $k_{vp} = -0.0083$, $k_{vs} = -0.0179$ and $k_\rho = 0.0333$.

With ΔR_P, ΔG, k_{vp}, k_{vs} and k_ρ modelled, we can substitute their valuse to the matrix in Equation 33.

$$\begin{bmatrix} \Delta S \\ \frac{\Delta V_P{}^P}{V_P} \end{bmatrix} = \begin{bmatrix} \frac{1}{2}(-0.0083) & \frac{p-8r}{2p} \\ \frac{1}{2}(-0.0083) + \frac{1}{2}(0.0333) & \frac{1}{2} \end{bmatrix}^{-1} \begin{bmatrix} -0.098 \\ 0.048 \end{bmatrix}$$

For this model, p = 1.31 and r = 0.56. The solutions of the above equation are $\Delta S = 0.51$ and $\frac{\Delta V_P}{V_P}^P = 0.083$ which can be converted to effective pressure changes of 10.5 MPa. The results are very good because I expected a change in effective pressure of 10 MPa and 0.5 saturation change. Because the results are good, I will apply this method to a real data offshore West Africa.

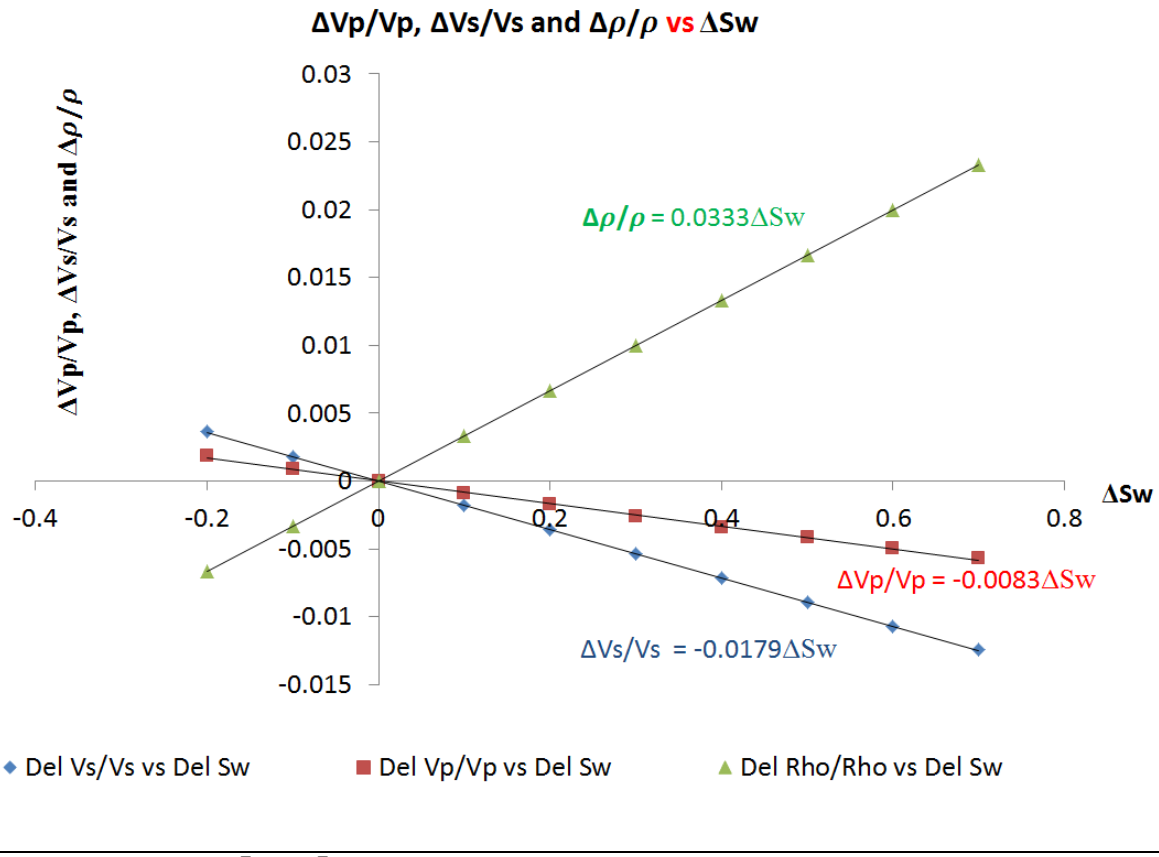

Figure 29: A plot of $\frac{\Delta V_P}{V_P}^F$, $\frac{\Delta V_S}{V_S}^F$ and $\frac{\Delta \rho}{\rho}^F$ vs ΔSw .

2.5 Sensitivity of *p* and *r* to the solution.

Before I can apply the method on a real data, I will first investigate the sensitivity of p and r. Here, I want to see if changing the values of p and r will change the solution significantly or not, this way I will have a better understanding of whether the values of p and r are very important to get right or an estimate of $p = 1$ and $r = 0.5$ can be used.

Table 3 shows estimated saturation and pressure changes when p is kept constant at 1.31 and r varies from 0.2 to 0.8. It is clear that changing the value of r changes the results significantly.

Table 4 shows estimated saturation and pressure changes when *r* is kept constant at 0.56 and *p* varies from 0.25 to 1.75. It is clear that changing the value of *p* changes the results significantly.

r	ΔSw	ΔP
0.2	-23	679
0.3	6	-4
0.4	3	3
0.5	1	8
0.6	0.1	12
0.7	-0.7	16
0.8	-1.4	20

Table 3: Variation of ΔSw and ΔP with varying *r* when *p* is kept constant at 1.31.

p	ΔSw	ΔP
0.25	3.4	6.2
0.5	2.9	6.9
0.75	2.3	7.7
1.0	1.6	8.7
1.25	0.75	10.1
1.5	-0.4	11.9
1.75	-1.8	14.6

Table 4: Variation of ΔSw and ΔP with varying *p* when *r* is kept constant at 0.56.

r cannot physically be greater than $\frac{1}{\sqrt{2}} \approx 0.76$, and will be always less than $\frac{1}{\sqrt{3}} \approx 0.58$ and likely to be closer to 0.5. *p* is generally between 1 and 1.5. For common values of *p* (1 to 1.25) and *r* (0.45 to 0.58). The error in the estimated ΔP is approximatelly +/- 20% (acceptable) but for ΔSw the error can range from - 300% to +300%. This means the saturation changes are very sensitive to *p* and *r*. For this method to be succesful, the estimates of *p* and *r* should be good and we can estimate these parameters when we calculate V_S / V_P from log data (for *r*) and when we plot V_P vs V_S (for *p*). Note that the values of *p* and *r* should be estimated from a plot of the reservoir sands (not shales) because that is where we are expecting to have changes in saturation and pore pressure.

It is a common practise to assume that *r* = 0.5 when we estimate ΔG, we can see that even if we get *p* correct, *r* = 0.5 gives a poor (100% error) estimate of ΔSw, Table 3.

Chapter 3: Application and Results

Equation 33 was tested on a model in Section 2.4 and produced good results. I will apply the proposed method to separate pressure and saturation changes in a producing field in West Africa. The available data are seismic difference volumes (2010-1999, 2003-1999 and 2010-2003) as full stack (7°-47°), near stack (7°-17°), mid stack (17°-27°), far stack (27°-37°), ultrafar stacks (37°-47°). There are log data for 5 wells with well 1 being an exploration well. The mid angle for the nears, mids and fars are 12°, 22° and 32° respectively. Figure 30 shows the full stack changes at the top of the reservoir. In the 2003-1999 data the changes are not clear. This is because the changes are very small and cannot be isolated from random noise.

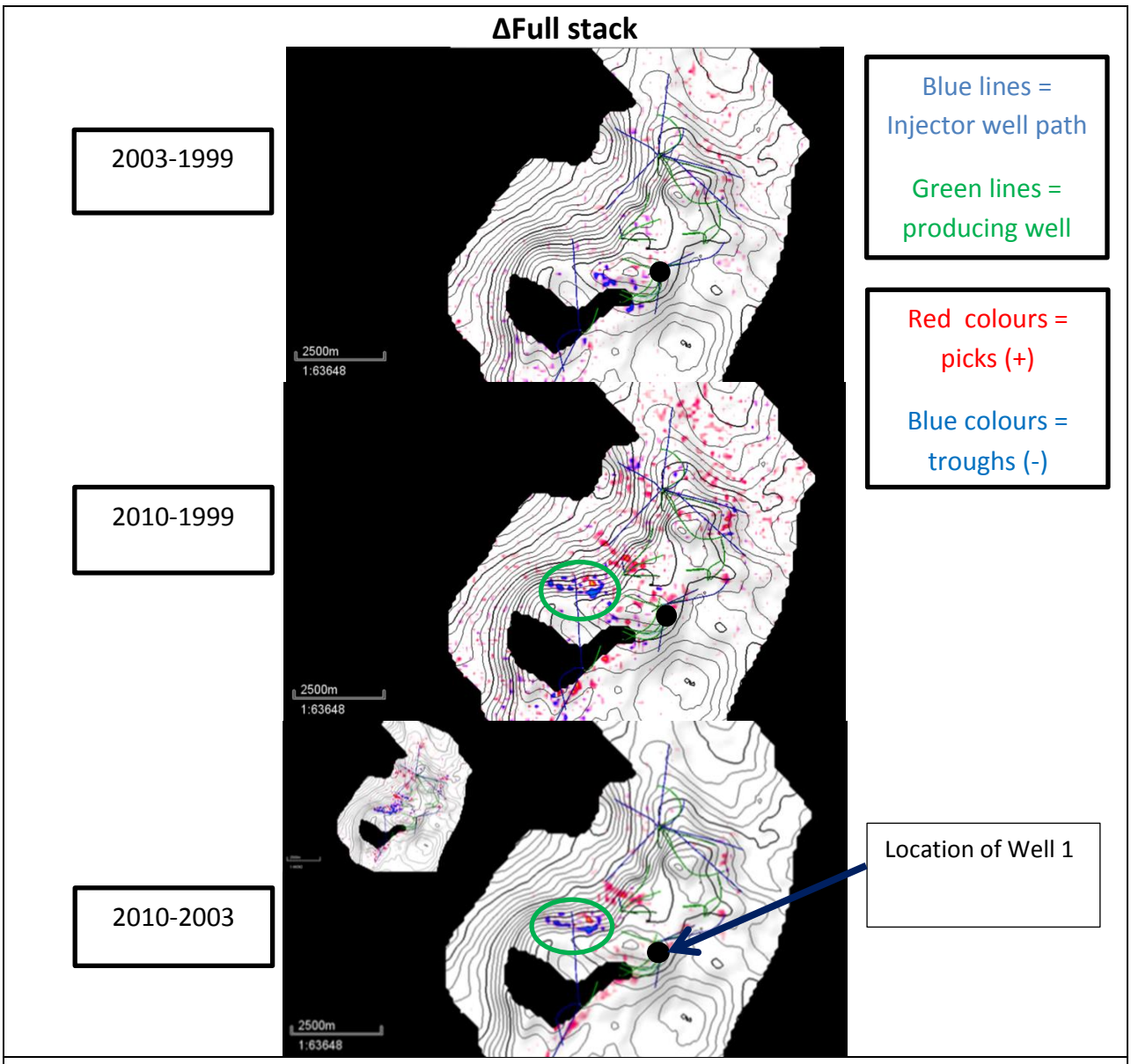

Figure 30**:** Full stack changes**, Top**: 2003-1999, **Middle:** 2010-1999 and **Bottom**: 2010-2003.

The cross-section view of the full stacks is shown in Appendix B1. The changes in intercept and gradient are not available but they can be calculated from the changes in partial stacks. Before we can calculate the changes in intercept and gradient, I will check if the frequency spectra of the different datasets match each other.

3.1 Spectral balancing

The far offset (fars) traces generally lack high frequencies compared to the near offset (nears). The lack of high frequencies in the far offset data is caused by absorption of high frequencies by the subsurface. Absorption is more effective for longer paths; this is why seismic data lack high frequencies at far offset data and at longer TWT. This means before we can start calculating the changes in intercept and gradient from partial stacks as indicated by Equation 35, we need to ensure that the frequency spectra of all the traces (near to far offsets) are balanced (Kemper, 2010). We generally remove the high frequencies from the near offset data to match it to the far offset data. Theoretically, we could also add high frequencies to the far offset data but in reality it is not possible to add back the lost frequency content.

Figure 31(a) shows the frequency spectrum of 2010 minus 1999 nears (blue), mids (green) and fars (red). It is clear that all the traces have similar frequency spectrum for high frequencies, which means the offsets were indeed matched. Figure 31(b) shows the frequency spectrum for 2003-1999 nears, mids and fars. Again the high frequencies do match. It is worth mentioning that both the 2010 and 2003 seismic data were matched to the 1999 seismic data.

We can see that the frequency spectra for nears, mids and fars do match, so we can calculate the changes in intercept and gradient.

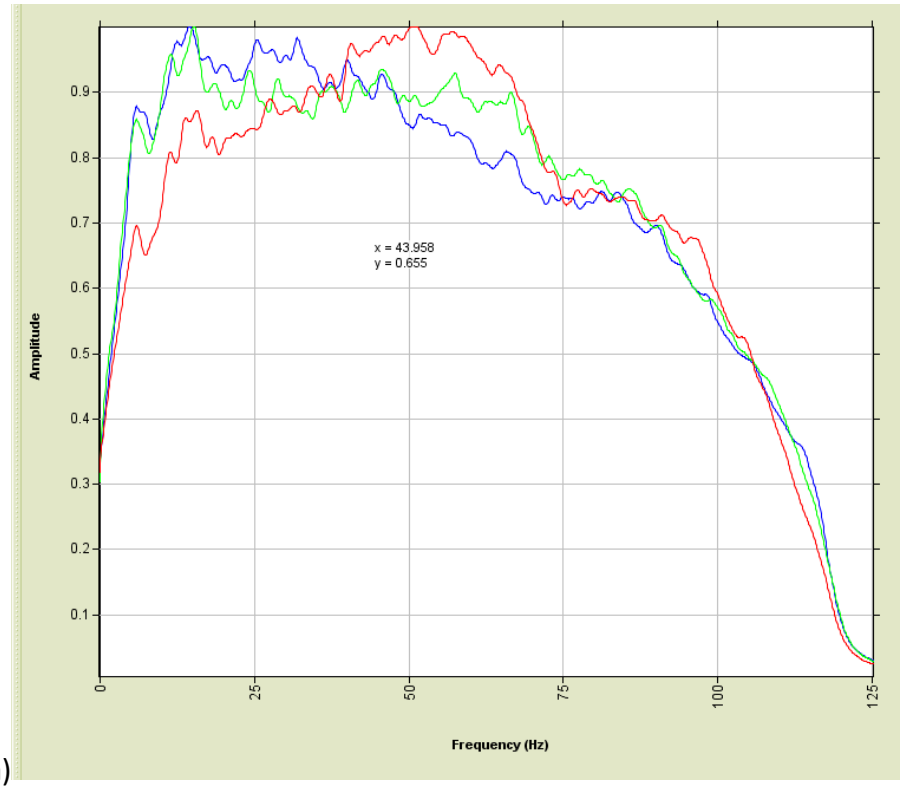

(a)

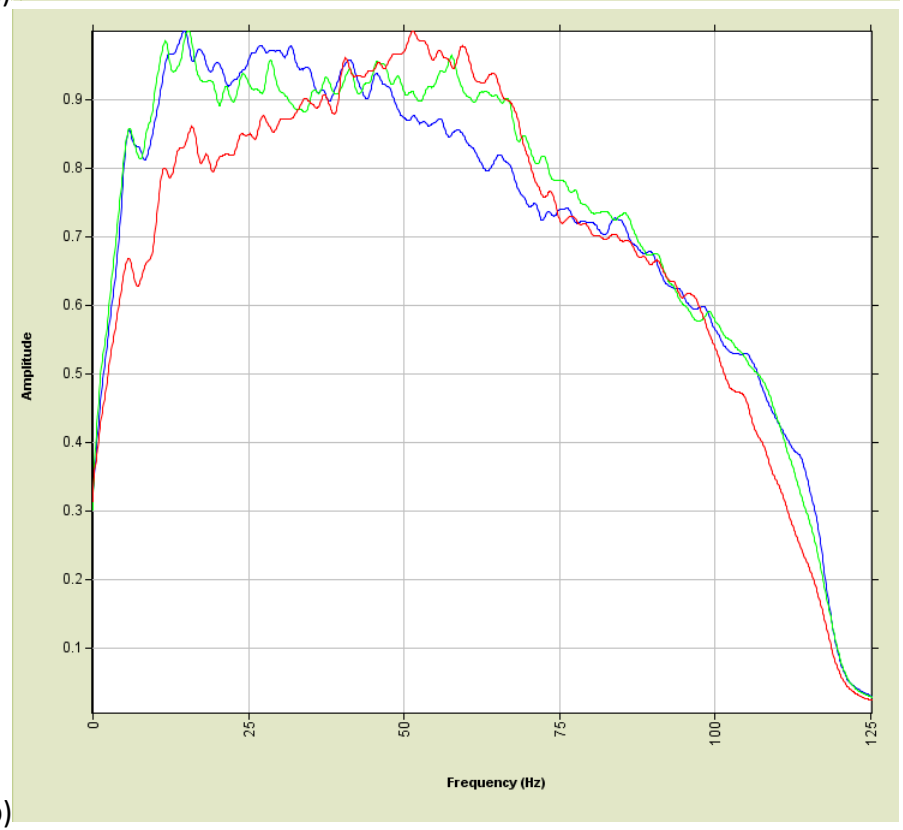

(b)

Figure 31: (a) Frequency spectra for nears, mids and fars for 2010-1999 data. (b) Frequency spectra for nears, mids and fars for 2003-1999 data.

3.2 Changes in Intercept and gradient from partial stacks

The intercept and gradient can be obtained from a linear regression of amplitudes of the near, mids and fars (Nam and Fink, 2008). This way, the signal to noise ratio of intercept and gradient is increased. Fitting a straight line through the amplitudes indicates that the intercept and gradient are a weighted sum of nears, mids and fars. The weights depend on the angle of incidence (Appendix A1).

$$R_P = r_n N + r_m M + r_f F \qquad G = g_n N + g_m M + g_f F \qquad \text{Eq.34}$$

The changes in intercept and gradient can also be calculated from the weighted sum of the changes in nears, mids and fars.

$$\Delta R_P = r_n \Delta N + r_m \Delta M + r_f \Delta F \qquad \Delta G = g_n \Delta N + g_m \Delta M + g_f \Delta F \qquad \text{Eq.35}$$

I calculated the changes in intercept and gradient using the above equations. The calculated changes in intercept and gradient are shown in Figure 32.

Vintage	ΔR_P	ΔG
2003-1999	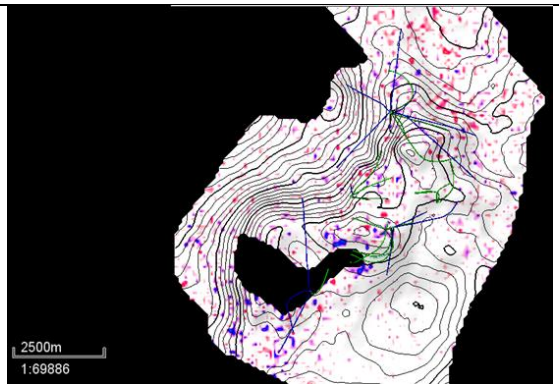	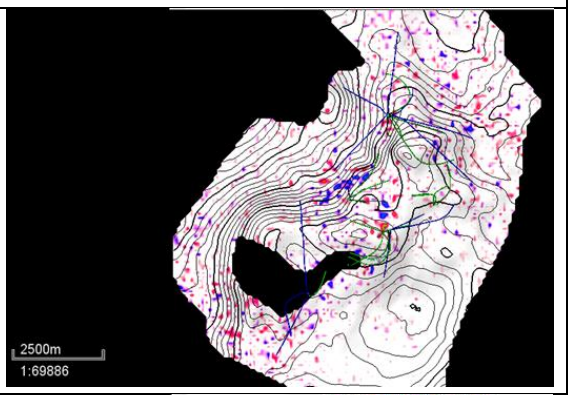
2010-1999	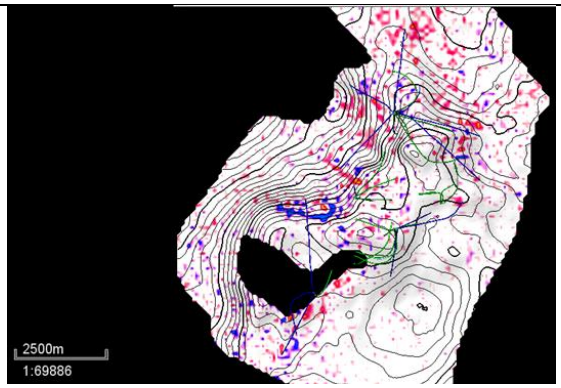	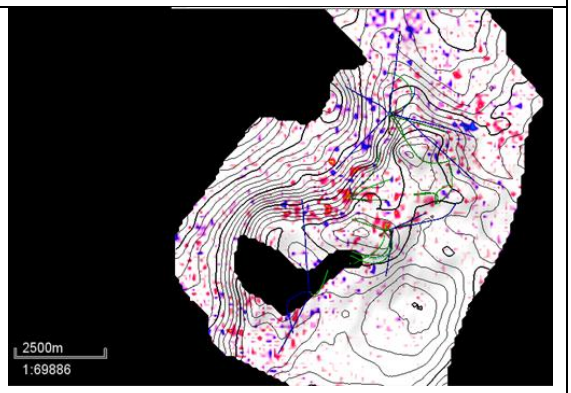
2010-2003	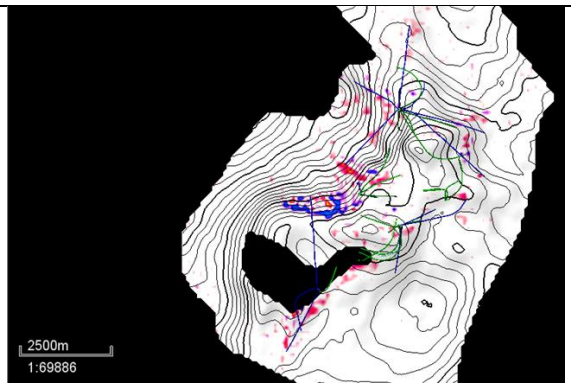	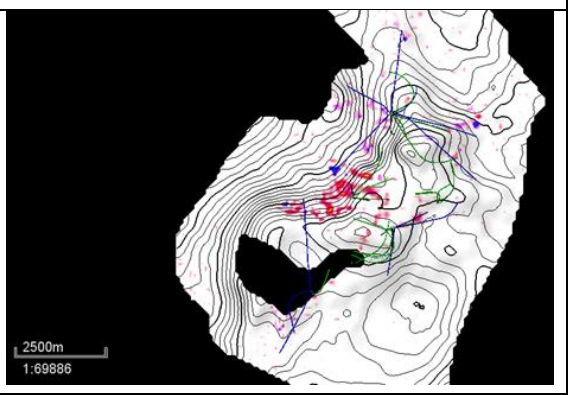

Figure 32: Calculated changes in intercept and gradient, **Top**: 2003-1999, **Middle:** 2010-1999 and **Bottom**: 2010-2003. The image is for the top of the reservoir.

The cross-section view of the top of the reservoir is indicated in Figure 33. The displayed data is the 2010-2003 changes in intercept (bottom) and gradient (top) (Fig. 33). I will focus on one reservoir; the top of the reservoir is indicated by the black line.

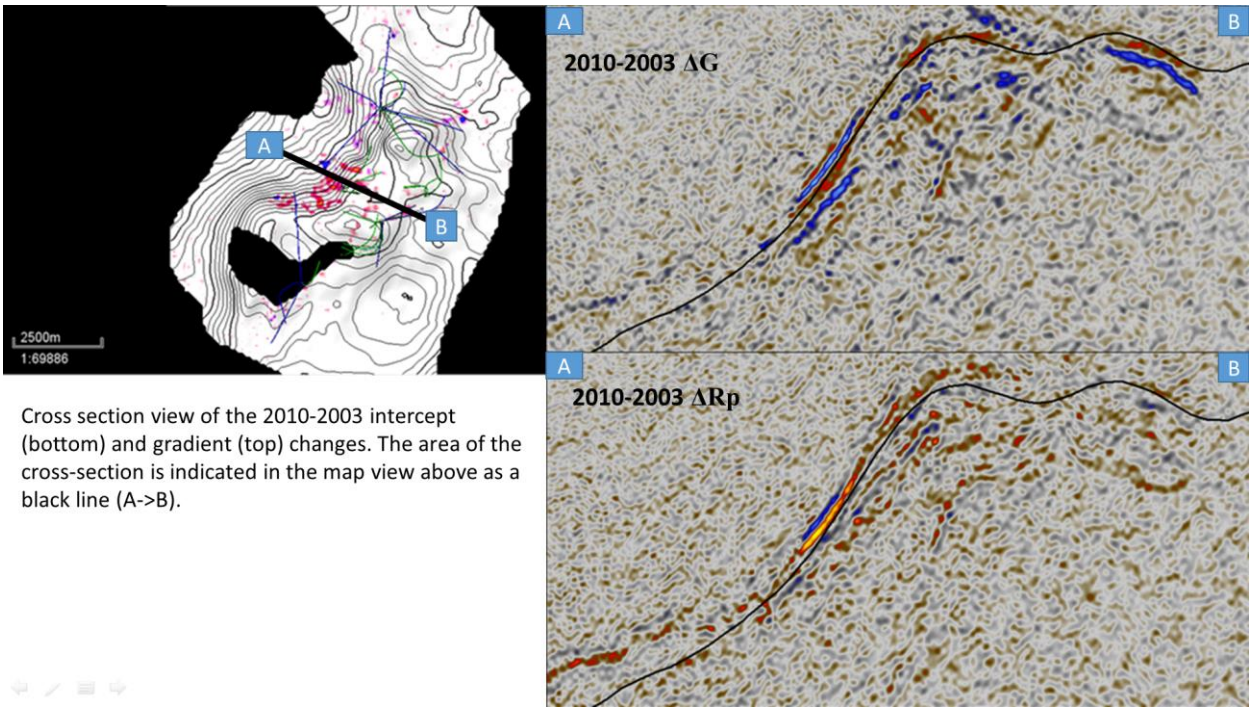

Cross section view of the 2010-2003 intercept (bottom) and gradient (top) changes. The area of the cross-section is indicated in the map view above as a black line (A->B).

Figure 33: Cross-section view of the top of the reservoir. Top: 2010-2003 ΔG, bottom: 2010-2003 ΔR_P.

Now that we have calculated the changes in intercept and gradient, to use Equation 33, we need to get a good estimate of *p*, *r*, k_{vp} and k_ρ. The estimates of these values for this field are shown in the next section (rock physics modeling).

3.3 Rock physics modeling

To estimate the values for k_{vp}, k_{vs} and k_ρ , I will use Well 1 as a calibration to the model. I will first carry out a seismic to well tie in order to ensure that the log data represent what we see on seismic data.

3.3.1 Seismic to well tie

The reason we do seismic to well tie is that when we create rock physics models, we always use log data to calibrate the models because logs provide a very good estimate of the subsurface parameters such as velocity and density. I tied Well 1 to the 1999 full stack seismic data. The seismic to well tie results are shown in Figure 34. The correlation between the seismic data and a synthetic seismic using a wavelet estimated at the well location is 0.775 with -10ms bulk shift

on the well. This is a good correlation and the estimated wavelet is shown in Figure 35. Because the correlation is high, we can say with confidence that the log data do match what we see from seismic data. The estimated wavelet has a 42 degree phase.

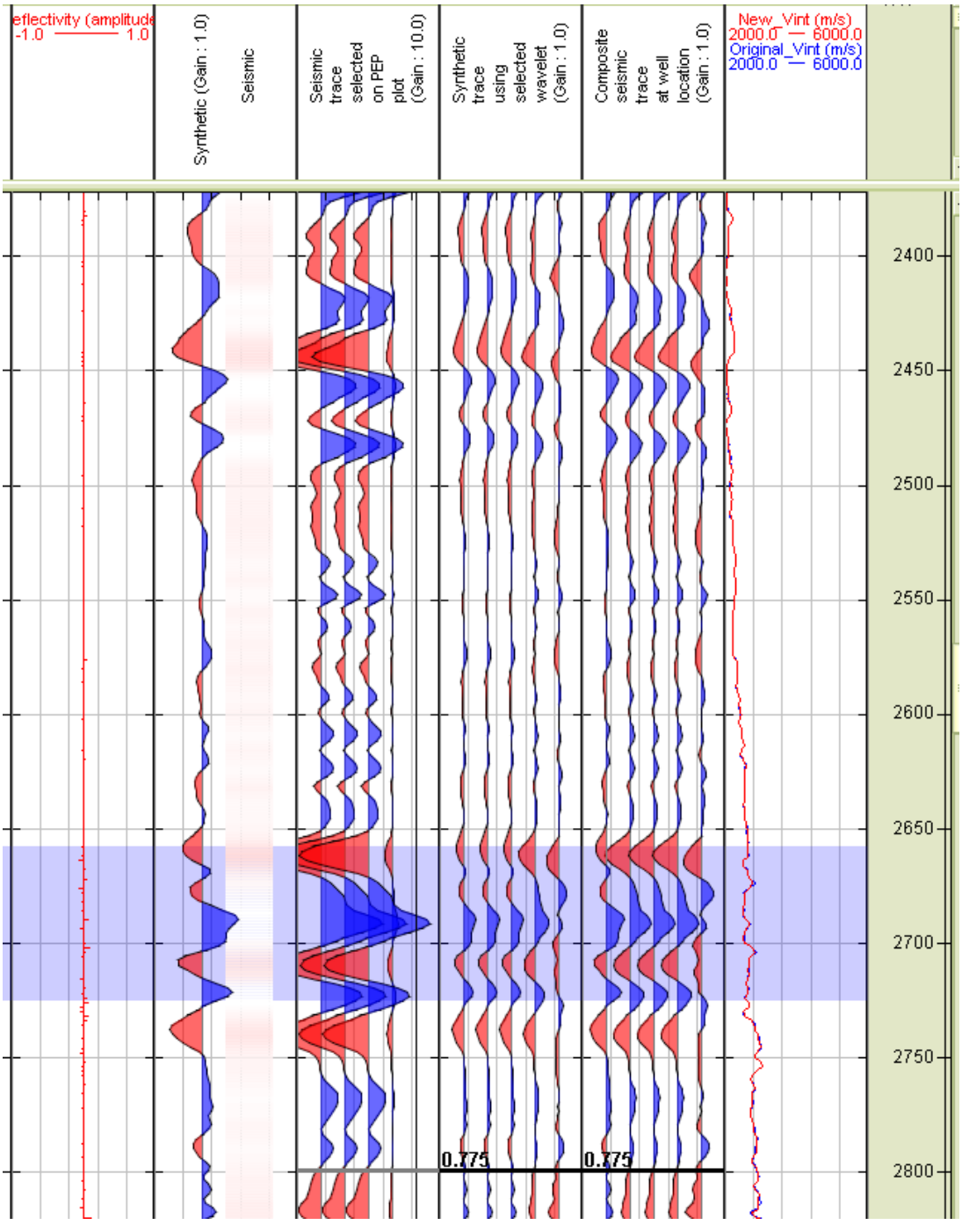

Figure 34: Seismic to well tie, correlation = 0.775

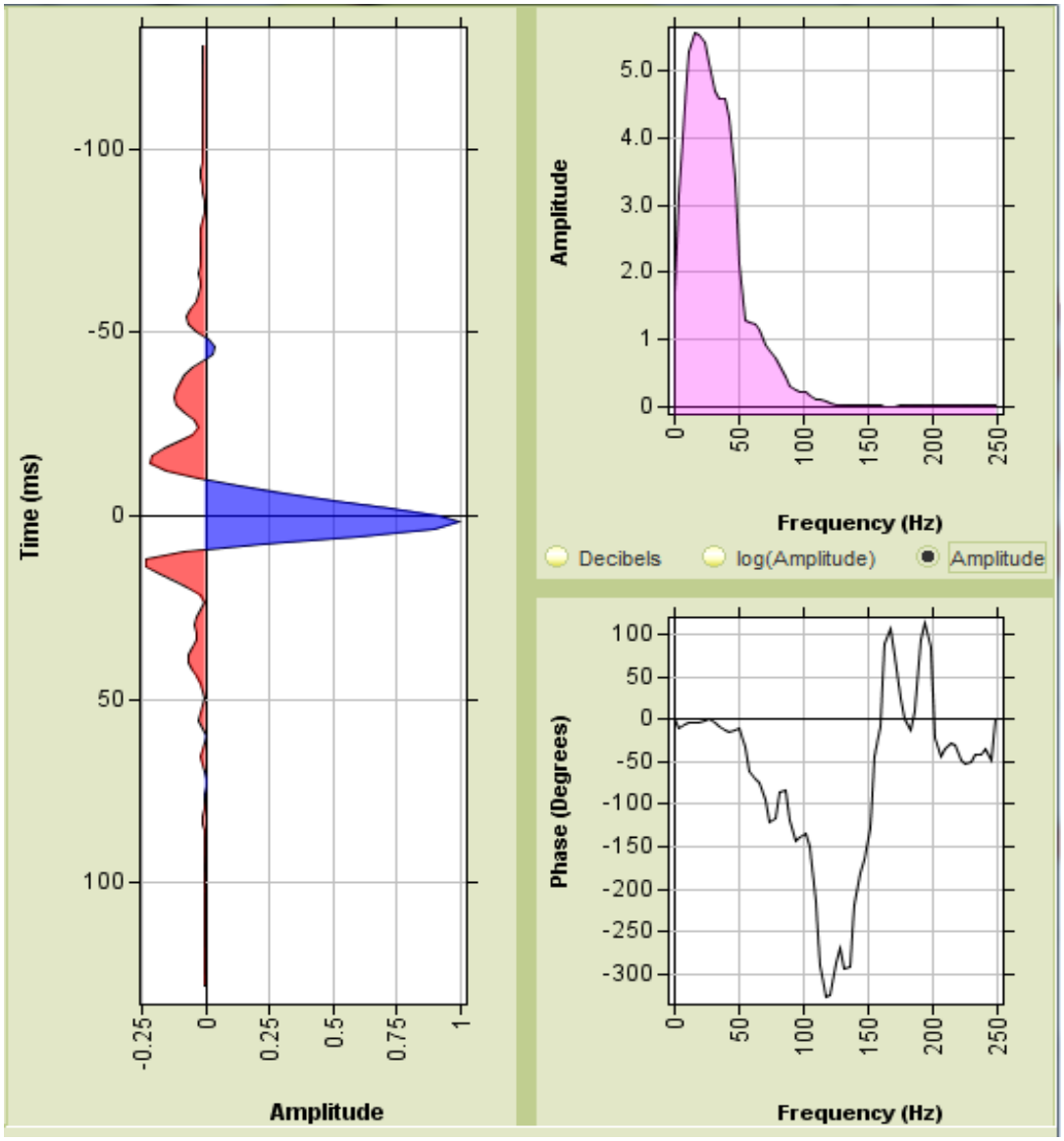

Figure 35: -42 degrees phase rotated wavelet at well location.

3.3.2 Rock physics modeling

A plot of K_{dry}/K_Mvs porosity for Well 1 is shown in figure 36. From the graph, the porosity of the reservoir covers a range between 20 % to 35 %. The data fall between 0.02 and 0.07 for

$K_\emptyset/K_M$ (red curves in Figure 36). I calculated $K_\emptyset$ = 1.48 GPa (assuming K_M = 37 GPa) using $K_\emptyset/K_M$ = 0.04.

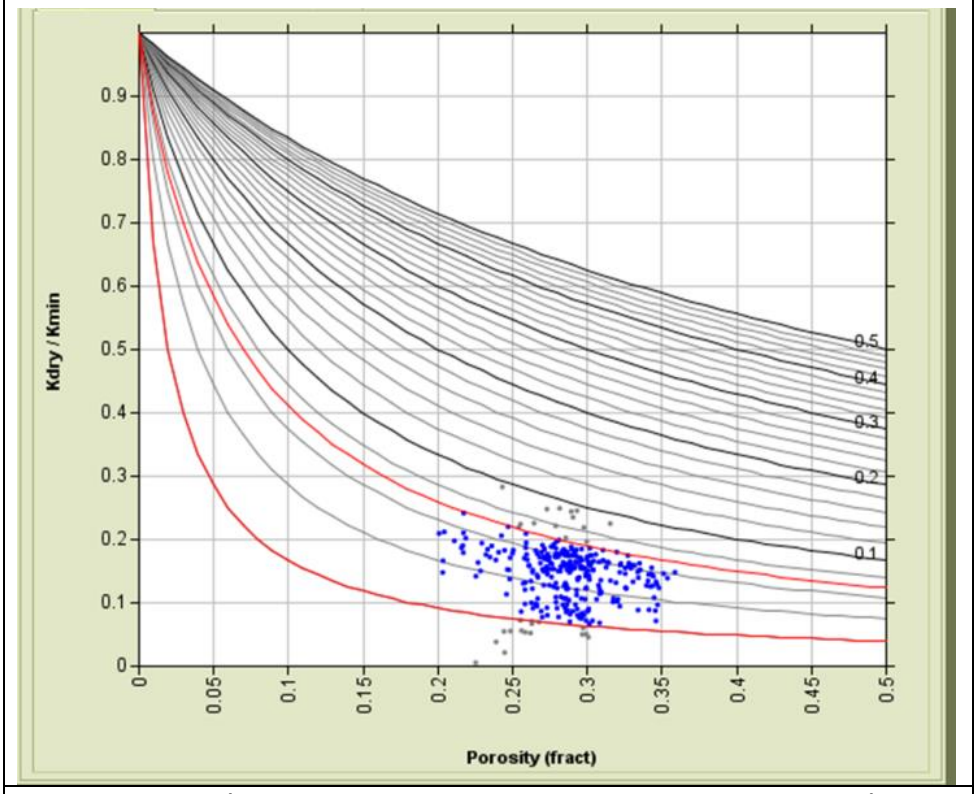

Figure 36: K_{dry}/K_M vs porosity for Well 1. Curves of constant $K_\emptyset/K_M$ are shown in black.

From the saturation log at Well 1, the average initial oil saturation for the reservoir is 0.75 (75% of the pore space). Using an average porosity of 27.5% and $K_\emptyset$ = 1.48 GPa, the calculated dry rock modulus using the pore space stiffness model is 4.70 GPa. I used Wood's equation to calculate the fluid bulk modulus for 0 to 100% water saturation (*Sw*), assuming K_{water}= 2.29 GPa and K_{oil}= 2 GPa. I also calculated the density of the rock at different saturation assuming ρ_M = 2.65 (Quartz). I then used the Gassmann equation to calculate the saturated bulk modulus (K_{sat}) of the rock for different saturations. I calculated V_P using the calculated densities and saturated bulk moduli. To test whether the model estimated these parameters well enough, I used the 0.75 oil saturation velocity and density and superimposed them on top of log data at the top of the reservoir (Fig. 37). The average shale properties are 2656 m/s and 2.26 g/cm^3 for V_P and density respectively.

The Gamma log in Figure 37 shows the API values for shales and reservoir. The second column shows a plot of V_P from the log data (blue) and modeled V_P (red). The column on the right

shows a modeled density (red) and log density (blue). The modeled parameters are good estimates of the reservoir with the high frequency removed. Because the match is good, I can use the model to calculate and plot $\frac{\Delta V_P{}^F}{V_P}$, $\frac{\Delta V_S{}^F}{V_S}$ and $\frac{\Delta \rho^F}{\rho}$ vs ΔSw and determine k_{vp} and k_ρ.

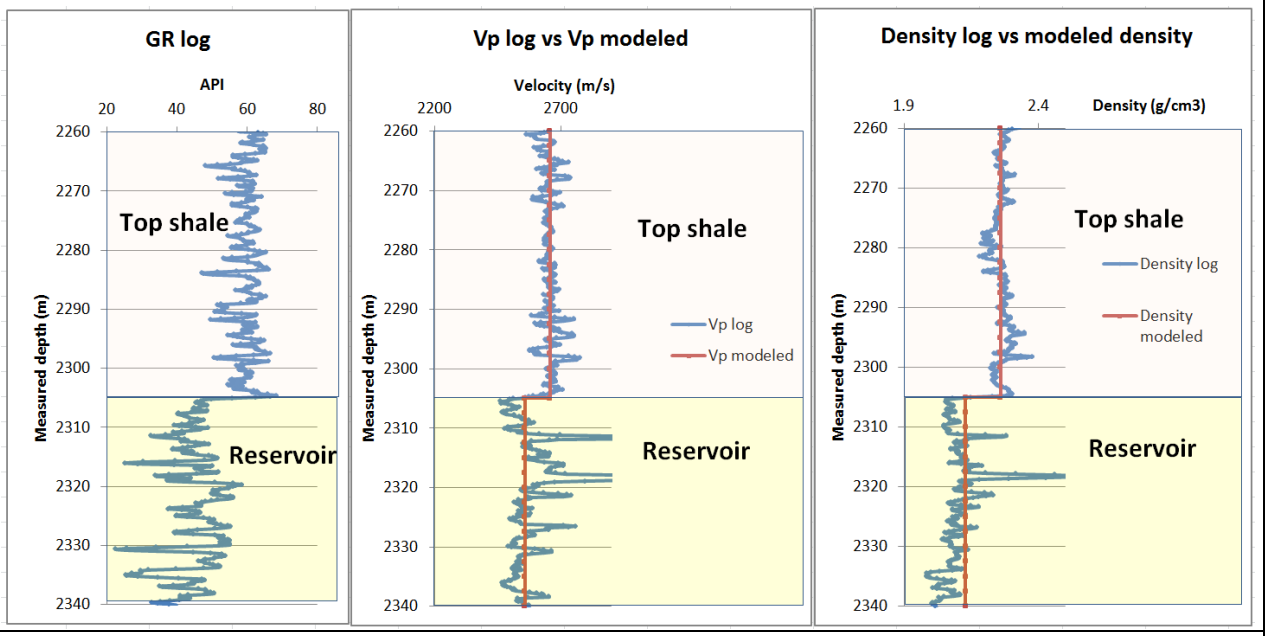

Figure 37: Comparison between modeled and log velocities and densities.

The shear modulus of the fluid is zero; therefore the dry rock shear modulus is the same as that in the log data at 27.5% porosity, μ = 3.12 GPa. The calculated $\frac{\Delta V_P{}^F}{V_P}$, $\frac{\Delta V_S{}^F}{V_S}$ and $\frac{\Delta \rho^F}{\rho}$ vs ΔSw are shown in Figure 38.

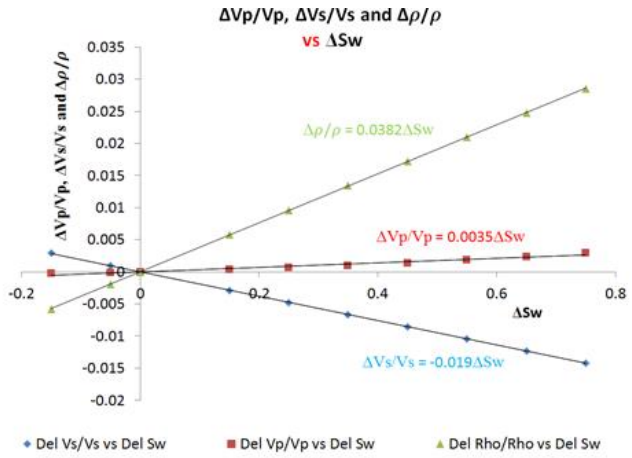

Figure 38. $\frac{\Delta V_P{}^F}{V_P}$, $\frac{\Delta V_S{}^F}{V_S}$ and $\frac{\Delta \rho^F}{\rho}$ vs ΔSw.

The gradient constants in Equation 4 relating changes in velocities and density vs changes in saturation are $k_{vp} = 0.0035$, $k_{vs} = -0.019$ and $k_{\rho} = 0.0382$. Note that k_{vs} is not required for Equation 33.

The nears, mids and fars difference volumes have a mid angle of 12°, 22° and 32° respectively. Using Equation 33, the changes in intercept, the changes in gradient, k_{vp} and k_{ρ} , the solution for $\frac{\Delta {V_P}^P}{V_P}$ and ΔS are:

$$\Delta S \approx 46.6\Delta Rp + 16.4\Delta G$$

$$\frac{\Delta {V_P}^P}{Vp} \approx 0.06\Delta Rp - 0.68\Delta G$$

The *p* and *r* values for this field at the well location are 0.98 and 0.47 respectively. *p* is the gradient when V_P is plotted against V_S and *r* is the velocity ratio (V_S/V_P). *p* and *r* are estimated from log data at the well location for water saturated sands.

A rough estimate of ΔP from $\frac{\Delta {V_P}^P}{V_P}$

The solution of Equation 33 does not show the changes in pressure but they can be interpreted from changes in velocity reflectivity due to pressure changes. This also gives the interpreters the freedom to use any equation they prefer to calculate effective pressure changes from changes in velocity. For example, Landro and Kvam (2002) used Hertz-Mindlin model to show that:

$$\frac{\Delta {V_P}^P}{V_P} = \frac{\Delta {V_S}^P}{V_S} = \left(\frac{P}{P_0}\right)^{\frac{1}{6}} - 1$$

They also mentioned that core measurement sometimes do not agree with the exponent. As an estimate, one can use the above equation to calculate ΔP from $\frac{\Delta {V_S}^P}{V_S}$. Therefore a rough (no core samples to support or calibrate the results) estimate of changes in effective pressure can be calculated from $\frac{\Delta {Vs}^P}{Vs}$ as:

$$\Delta P = \left(\frac{\Delta {V_S}^P}{V_S} + 1\right)^6 P_0 - P_0$$

$$P_0 = initial\ pressure = 10MPa\ (for\ this\ project)$$

$\frac{\Delta {Vs}^P}{Vs}$ can be obtained from $\frac{\Delta {V_P}^P}{V_P}$ using Equation 29.

$$\Delta P \approx \left(\frac{\Delta {V_P}^P}{V_P}\frac{2}{p} + 1\right)^6 P_0 - P_0$$

The above equation can be used to estimate ΔP from $\frac{\Delta {V_P}^P}{V_P}$.

3.4 Results

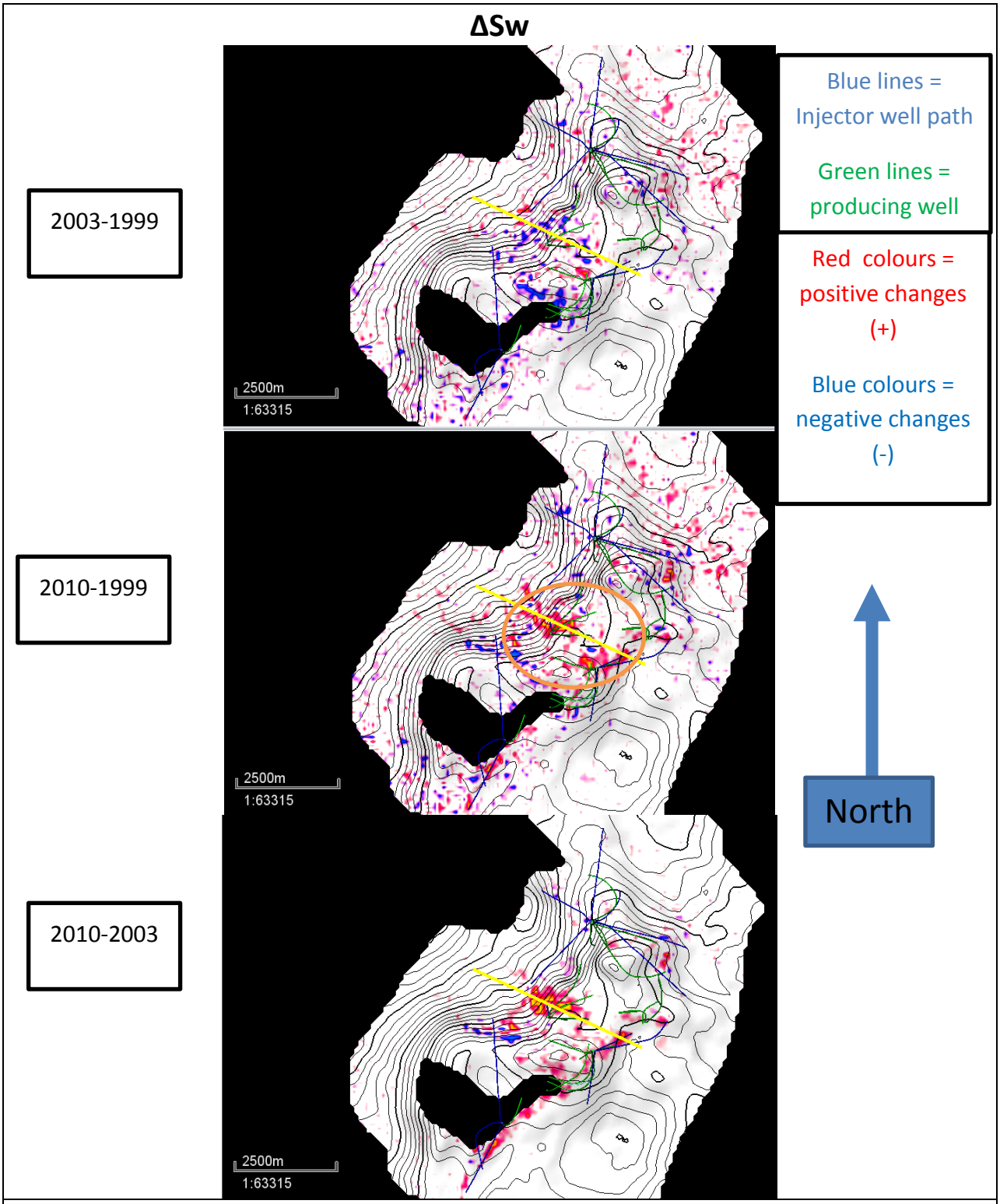

Figure 39**:** Changes in water saturation**, Top**: 2003-1999, **Middle: 2010-1999** and **Bottom**: 2010-2003.

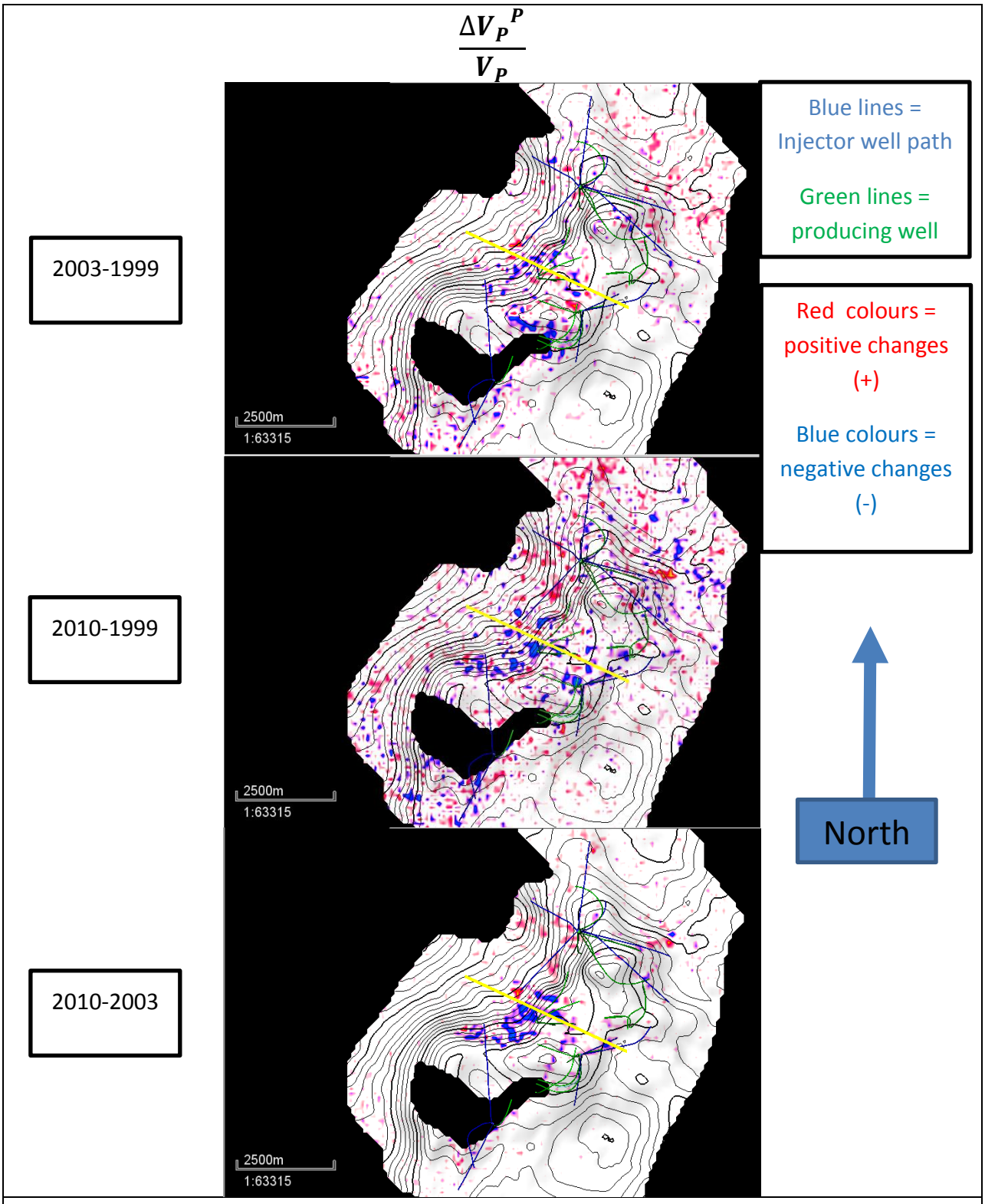

Figure 40**:** Changes in velocity reflectivity due to pressure**, Top**: 2003-1999, **Middle: 2010-1999** and **Bottom**: 2010-2003.

Figure 39 shows the changes in saturation for 2003-1999, 2010-1999 and 2010-2003 data. The 2003-1999 Δ*Sw* do not show any localized changes in saturation. The 2010-1999 Δ*Sw* show positive changes in saturation (orange circle). Both the 2003-1999 and 2010-1999 Δ*Sw* have random distribution of positive and negative changes in areas where there are no wells; these amplitudes are probably noise (discussed in Chapter 4). Noise is also present in the calculated intercept and gradient changes (Fig. 32) and full stack data (Fig. 30) for the 2003-1999 and 2010-1999 results and data.

The 2010-2003 Δ*Sw* show positive saturation changes (red) from the center to the southern part of the reservoir. The northern part of the reservoir does not show any significant saturation changes. The 2010-2003 Δ*Sw* appear to have a much higher signal to noise ratio. The Δ*Sw* results have localized changes where we have wells as expected.

Figure 40 show the changes in velocity reflectivity due to pressure for 2003-1999, 2010-1999 and 2010-2003 data. The 2003-1999 and 2010-1999 results do not show any localized changes and contain a significant amount of noise. The 2010-2003 results show negative changes from the center to the southern part of the reservoir and positive changes from the center to the northern part of the reservoir.

Note that the 2010-2003 results $\left(\Delta Sw \text{ and } \frac{\Delta {V_P}^P}{V_P}\right)$ show changes where we have wells, unlike the 2010-1999 and 2003-1999 results which show changes in areas where there are no wells. This means the 2010-2003 results are as expected and have signal to noise ratio compared to 2010-1999 and 2003-1999.

An obvious question to ask at this point is "**why ΔP was not estimated from $\frac{\Delta {V_P}^P}{V_P}$ as indicated at the end of section 3.3.2?**", the reason is that the seismic difference volumes used to calculate the changes in seismic intercept and gradient have been scaled which resulted in $\frac{\Delta {V_P}^P}{V_P}$ and Δ*Sw* being scaled as well. The challenge is to find out what is the scaling value, but without the knowledge of what the final pressure and saturation at the reservoir is, it is not possible to find the scaling value. Therefore the results will be presented as $\Delta Sw \text{ and } \frac{\Delta {V_P}^P}{V_P}$ rather than ΔSw and ΔP.

Chapter 4: Discussion

4.1 Noise in 1999 data

The differences in full stack data (Fig. 30), ΔSw (Fig. 39) and $\frac{\Delta {V_P}^P}{V_P}$ (Fig. 40) between 2003 and 1999 do not show any interesting amplitude anomalies which are prominent from the background noise. A possible reason for this is that the saturation and pressure changes in 2003 were too **small to be detected using seismic data** because the field in 2003 was still in its initial stages of production and we might not expect to see any significant changes from seismic data. Another possible reason is that **either the 1999 or the 2003 data has low signal to noise ratio**.

The changes in gradient in Figure 41, the 2003-1999 and 2010-1999 contain a significant noise level on the background but we do not see that much noise in the 2010-2003 data (Fig. 41). It is clear that **the 2003 data does not have low signal to noise ratio**. This suggests that the 1999 data has a significant amount of noise which resulted in the 2003-1999 and 2010-1999 data having low signal to noise ratio. For this reason, I will not discuss the 2003-1999 results. The 2010-1999 data also contains noise but the anomalies associated with the reservoir can be seen in some areas (Fig. 41).

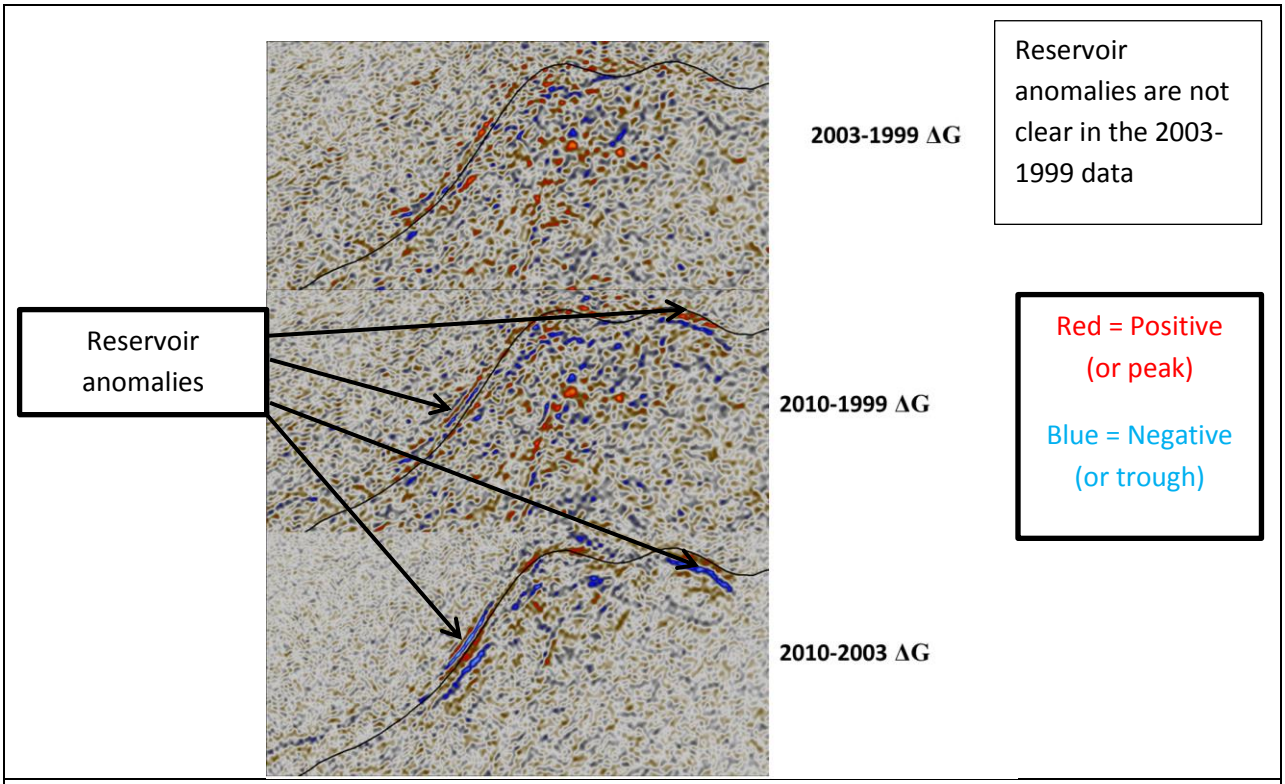

Figure 41: Changes in the gradient. Black line is the top of the reservoir. We can see that the background noise in the 2010-1999 and 2003-1999 is as big as the amplitude anomalies at the top of the reservoir.

4.2 Proposed methodology result

Because the 2003-1999 results and data do not show any prominent changes, it is not surprising that the 2010-1999 and 2010-2003 results display similar amplitude anomalies (Fig. 42).

The 2010-1999 and 2010-2003 ΔSw show similar amplitude anomalies if the background noise in the 2010-1999 results were to be removed (Fig. 42). The results show a positive change in ΔSw (increase in water saturation) almost everywhere in the field (not clear in the northern part of the reservoir). This is expected because when producing from the field we expect water to replace hydrocarbons.

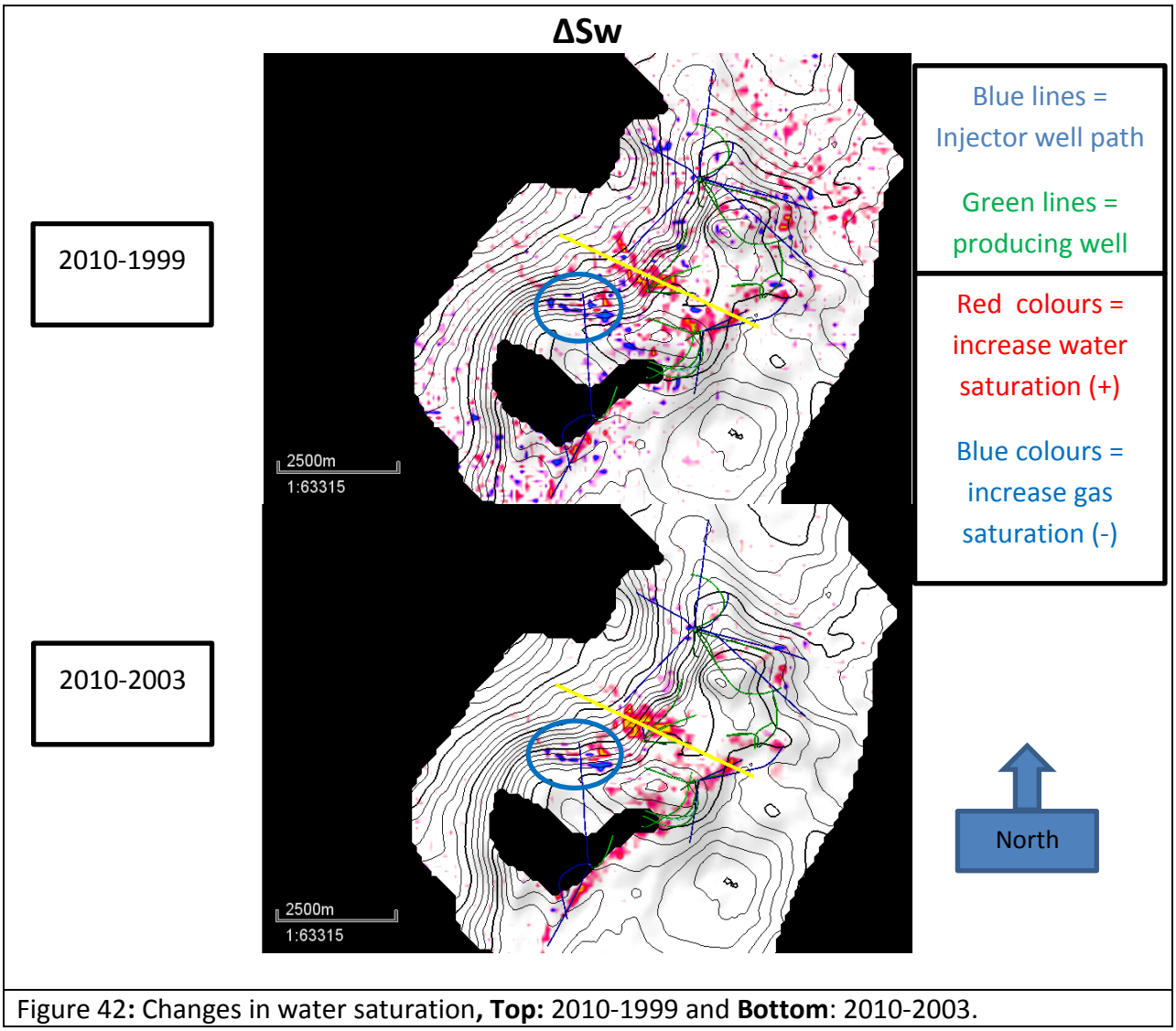

Figure 42**:** Changes in water saturation**, Top:** 2010-1999 and **Bottom**: 2010-2003.

The blue circle in Figure 42 shows an area with negative changes, the negative amplitudes in this area are caused by an error in the interpreted horizon.

Figure 43 shows change in velocity due to pressure $\left(\frac{\Delta V_P{}^P}{V_P}\right)$. The 2010-2003 data shows the results clearly compared to 2010-1999.

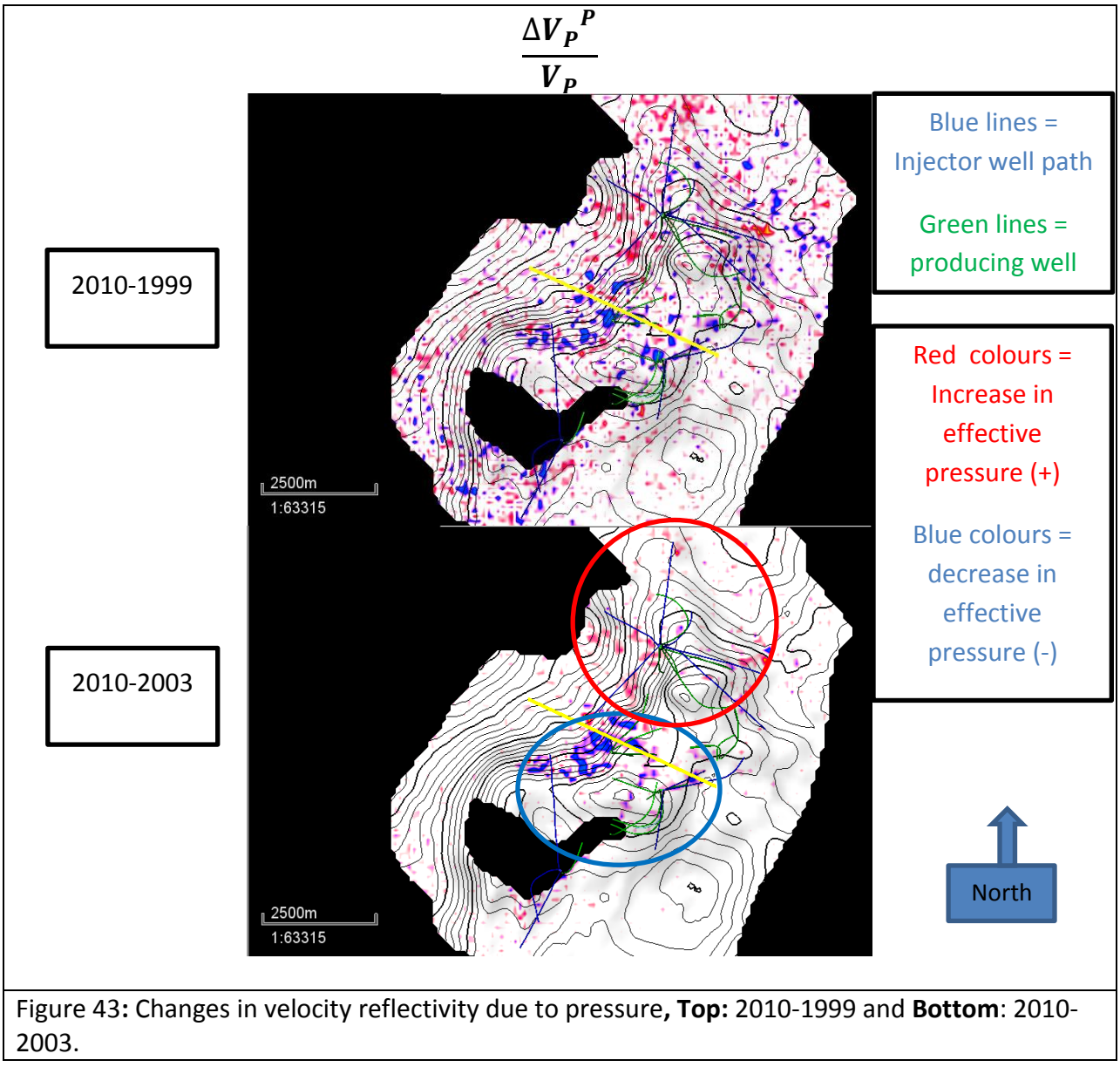

Figure 43**:** Changes in velocity reflectivity due to pressure**, Top:** 2010-1999 and **Bottom**: 2010-2003.

The northern part of Figure 43 shows positive changes and is indicated by the red circle. We expect positive changes if the final velocity is higher than the initial velocity ($\Delta V_P{}^P = V_{Pf} - V_{Pi}$), this suggest that the pore pressure has dropped increasing the contacts between the

grains and causing the velocity to increase. Therefore the northern part experienced an **increase in effective pressure** (drop in pore pressure).

The central and southern part shows negative changes (decrease in effective pressure) and is indicated by the blue circle. We expect negative changes if the final velocity is less than the initial velocity ($\Delta \boldsymbol{V_P}^{\boldsymbol{P}} = \boldsymbol{V_{Pf}} - \boldsymbol{V_{Pi}}$), this suggests that the pore pressure has increased; an increase in pore pressure causes the fluid to push the grains apart and reducing the velocity. Therefore the central and southern part experienced a **decrease in effective pressure** (increase in pore pressure).

From 2003 to 2010, the areas showing an increase in water saturation also show a decrease in effective pressure which is an increase in pore pressure. I think the increase in pore pressure in this area (blue circle) is due to injected water from the injectors. **This means the field is performing well in this area and the injector is keeping the pore pressure high to support the reservoir**.

The northern part of the map in Figure 43 suggests that from 2003 to 2010 the pore pressures have dropped over this region. This area does not show any prominent saturation changes. **More water needs to be injected over this area to support the reservoir and to push the hydrocarbons towards the producers**.

Because the northern part of the map shows a decrease in pore pressure, it is possible that there is pressure communication between all the wells in the area indicated by a red circle. Similarly, there is a possibility of pressure communication between all the wells in the area indicated by a blue circle (increase in pore pressure).

4.3 Changes in pressure and saturation from Extended Elastic Impedance (EEI)

I created the changes in EEI for 2010-2003 volumes from -80 to 80 degrees, the results are shown in Appendix C. From the solution of Equation 33, we expecting EEI(19°) and EEI(-85) to correlate with changes in water saturation and changes in velocity due to pressure respectively. EEI(19°) is approximately the fluid factor (ΔF) which indicate fluid anomalies (Msolo and Gidlow, 2015 and Smith and Gidlow, 1987).

The changes in saturation correlate with the changes in EEI(19°), this means EEI(19°) is a fluid indicator. Figure 44 shows a comparison between EEI(19°) before production, ΔSw (2010-2003) and $\frac{\Delta \boldsymbol{V_P}^{\boldsymbol{P}}}{\boldsymbol{V_P}}$ (2010-2003). The green circle in Figure 44 indicates an area which shows hydrocarbon

anomalies but do not show any 4D effect**. I propose new production wells in thus area because it is clear that hydrocarbons have not been removed.**

EEI(19°) before production	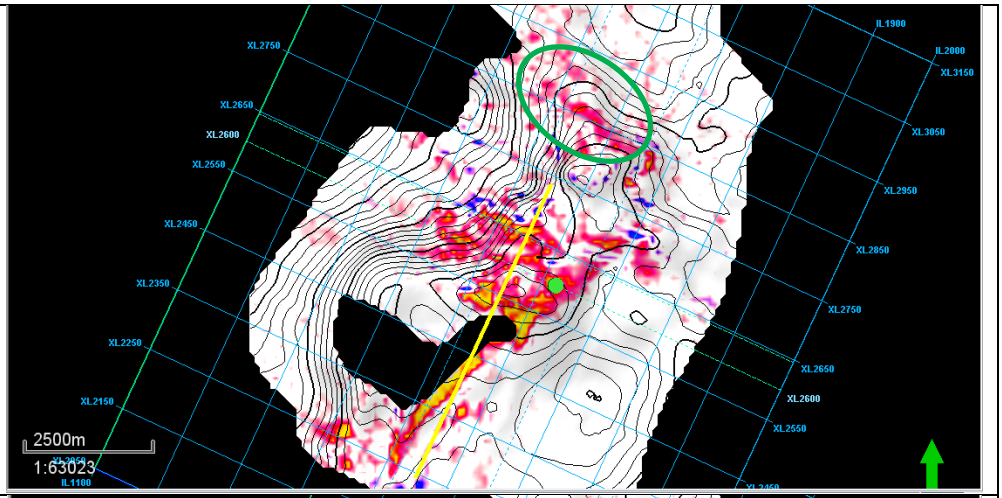
ΔSw (2010-2003) Or ΔEEI(19°)	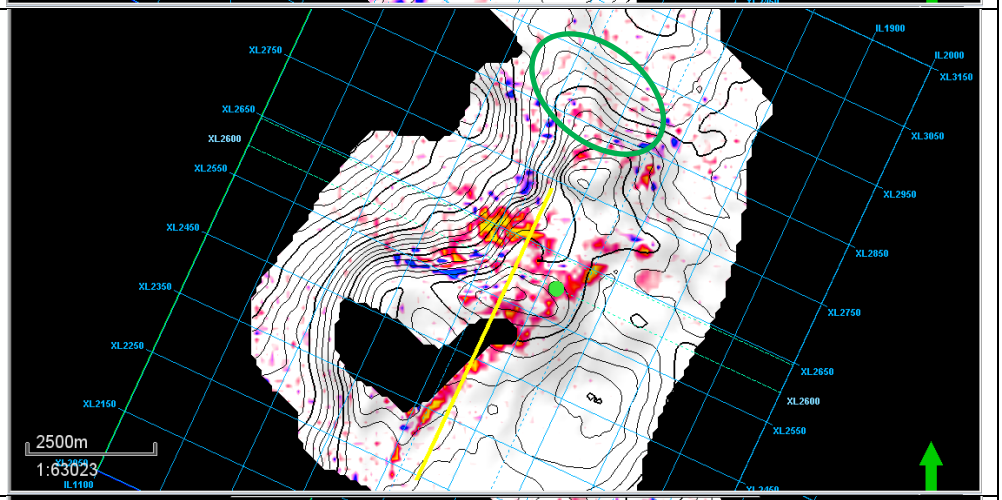
$\frac{\Delta V_P{}^P}{V_P}$ (2010-2003)	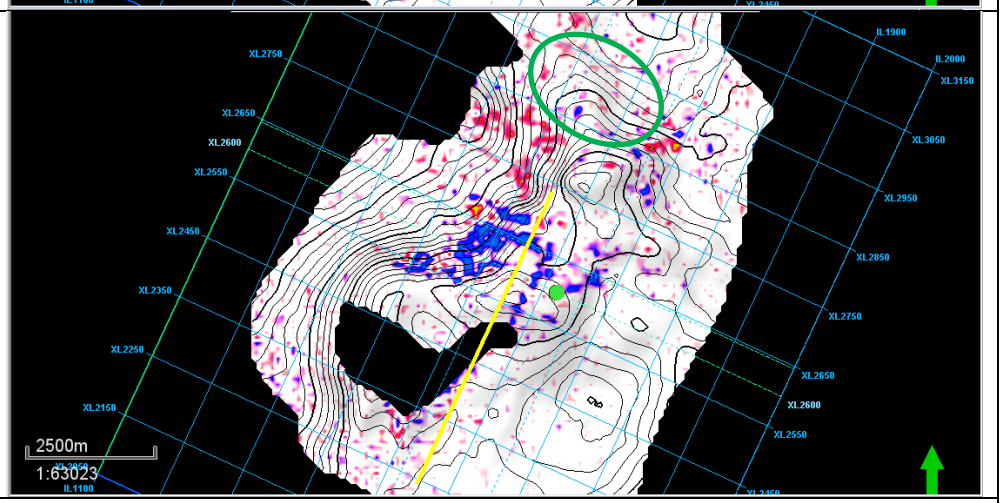

Figure 44: Comparison between EEI(19°) before production, Δ*Sw* (2010-2003) and $\frac{\Delta V_P{}^P}{V_P}$ (2010-2003).

4.4 Error in the estimated water saturation and effective pressure trends

When estimating k_{vp} and k_{ρ} , we used an average porosity of 27.5% and $K_{\emptyset}$ = 1.48 GPa (equivalent to $\frac{K_{dry}}{K_M} = 0.04$). We can see in Figure 36 that the porosity range for the reservoir varies between 20% and 35% and that $\frac{K_{dry}}{K_M}$ ranges between 0.02 and 0.07. I considered the whole porosity and $\frac{K_{dry}}{K_M}$ range to determine the error in the estimated ΔSw and $\frac{\Delta V_P{}^P}{V_P}$. Because we are using seismic intercept and gradient, It is convinient to display the errors in the results as saturation and pressure trends in the intercept and gradient cross-plot.

I varied porosity from 20% to 35% and $\frac{K_{dry}}{K_M}$ from 0.02 to 0.07. I calculated k_{vp} and k_{ρ} for all the combinations of the porosity and $\frac{K_{dry}}{K_M}$. I used the calculated k_{vp} and k_{ρ} to find an expression for ΔSw and $\frac{\Delta V_P{}^P}{V_P}$. From the expressions, I estimated the χ angle corresponding to water saturation trend and velocity reflectivity due to pressure (Fig. 45). The results are summarized in Figure 45.

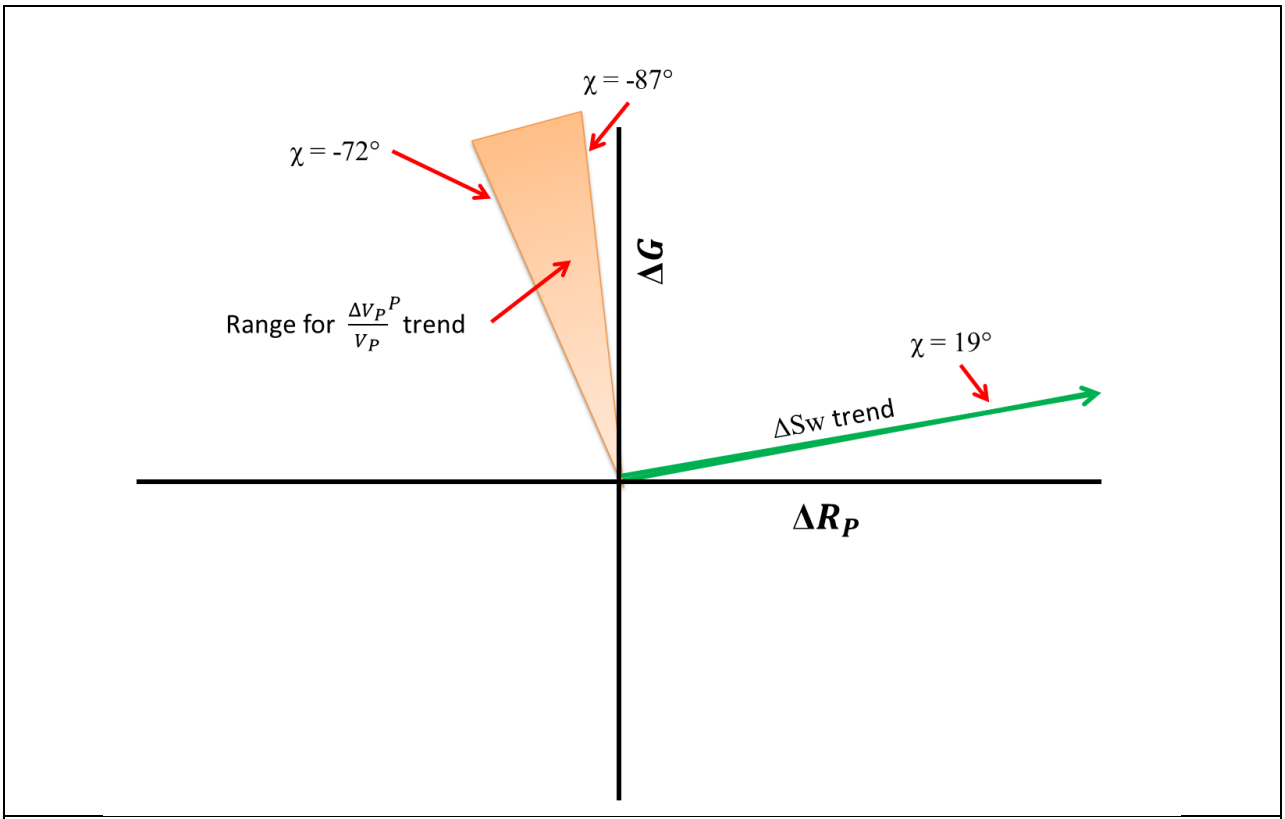

Figure 45: Error in the estimated Δ*Sw* and $\frac{\Delta V_P{}^P}{V_P}$ trends.

Figure 45 indicates that, changing the porosity or the pore space stiffness ($K_{\emptyset}$) of the rock does not change the saturation trend, the χ angle remains 19° for any combination of porosity and $\frac{K_{dry}}{K_M}$. The χ angle ranges between -72° and -87° for $\frac{\Delta \boldsymbol{V_P}^{\boldsymbol{P}}}{\boldsymbol{V_P}}$ for porosity and $\frac{K_{dry}}{K_M}$ in the range 20% - 35% and 0.02 – 0.07 respectively. This is expected because saturation changes do not affect porosity or $\frac{K_{dry}}{K_M}$, whereas pressure changes will change $\frac{K_{dry}}{K_M}$ or the porosity of the rock (see Eq.20). In conclusion, the EEIs corresponding to saturation changes and velocity reflectivity changes due to pressure are described by $\chi\,(\Delta P) \approx 79.5° \pm 7.5°$ and $\chi\,(\Delta Sw) \approx 19°$.

Chapter 5: Conclusion

The rock samples of the reservoir were not available for this study. This led to the modification of Landrø's method. The resulting equation showed that the changes in water saturation (ΔSw) and velocity reflectivity due to pressure $\left(\frac{\Delta V_P{}^P}{V_P}\right)$ are weighted sum of seismic intercept (ΔR_P) and gradient (ΔG).

From the central to the southern part of the ΔSw map for the reservoir, we have an increase in water saturation. These increases in water saturation areas are associated with an increase in pore pressure on the $\frac{\Delta V_P{}^P}{V_P}$ map. A reasonable conclusion is that water has replaced hydrocarbons and the pore pressure has increased due to injected water over this area, this means that the injected water is working effectively (**keeping the pore pressure high around the producers**). Therefore both the injectors and producers are performing well.

Wells in the northern part of the $\frac{\Delta V_P{}^P}{V_P}$ map might be in pressure communication with one another because the whole region shows a drop in pore pressure. The wells in the central and southern part are probably in pressure communication too (the whole region shows an increase in pore pressure).

A comparison between EEI(19°) before production, ΔEEI(19°) between 2010 and 2003 and $\frac{\Delta V_P{}^P}{V_P}$ (2010-2003) suggest potential hydrocarbon areas (green circles in Figure 44) which have not been produced. I propose new production well in these areas.

Chapter 6: Reference

1. Ashcroft W., 2011, A Petroleum Geologist's Guide to Seismic Reflection, *Wiley-Blackwell*.
2. Avseth P., Mukerji T., Mavko G. and Dvorkin J., 2010, Rock-physics diagnostics of depositional texture, diagenetic alterations, and reservoir heterogeneity in high-porosity siliciclastic sediments and rocks — A review of selected models and suggested work flows, *Geophysics*, vol 75, page 75A31-75A47.
3. Brown A. R., 2010, Dim spot in seismic images as hydrocarbon indicators, *Search and discovery article,* page 1-3
4. Castagna P. J. and Swan W. H., 1997,Principles of AVO crossploting, *The Leading Edge,* vol 63, page 337-342
5. Castagna P. J., Batzle M. L. and Eastwood R. L., 1985, Relationship between compressional wave and shear wave velocities in clastic silicate rocks, *Geophysics*, vol 50, page 551-570.
6. Chiburis E., Franck C., Leaney S., McHugo S. and Skidmore C., 1993, Hydrocarbon detection with AVO, *Seismics*, page 42 – 50.
7. Coterill K., Tari C. G., Molnar J. and Ashton R. P., 2002, Comparison of depositional sequences and tectonic styles among the West African deep water frontiers of western Ivory Coast, southern Equatorial Guinea and northern Namibia, *The Leading Edge,* page 1103-1111.
8. Dailly P., Lowry P., Goh K. and Monson G., 2002, Exploration and development of Ceiba Field, Rio Muni Basin, Southern Equatorial Guinea, *The Leading Edge,* page 1140-1146.
9. Freund D., 1992, Ultrasonic compressional and shear velocities in dry clastic rocks as a function of porosity, clay content and confining pressure, *Geophysics*, vol 108, page 125 – 135.
10. Gassmann F., 1951, Uber die Elastizitat poroser Medien: Vierteljahrsschrift der Naturforschenden Gesellschaft in Zurich, vol 1, page 1-23.
11. Gazdag J. and Sguazzero P., 1984, Migration of Seismic Data, *Proceedings of the IEEE*, vol 72, page 1302-1315.
12. Hashin Z. and Shtrikman., 1963, A variational approach to the elastic behavior of multiphase materials*, Journal of the Mechanics and Physics of Solids,* vol 11, page 127-140.
13. Kemper M., 2010, Rock physics driven inversion: the importance of workflow, *firstbreak,* vol 28, page 69-81.
14. Landrø M., 2001, Discrimination between pressure and fluid saturation changes from time-lapse seismic data, *Geophysics,* vol 66, page 836 – 844.

15. Landrø M. and Kvam Ø., 2002, Pore pressure estimation – What can we learn from 4D?, *CSEG Recorder***,** page 82 – 87.
16. Landrø M., Veire H.H., Duffaut K. and Najjar N., 2003, Discrimination between pressure and fluid saturation changes from marine multicomponent time-lapse seismic data, *Geophysics,* vol 68, page 1592 – 1599.
17. Li Y., Downtown J. and Yong X., 2007, practical aspects of AVO modeling, *The Leading Egde,* page 295 – 310.
18. MacBeth C., 2004, A classification for the pressure-sensitivity properties of a sandstone rock frame, *Geophysics,* vol 69, page 497 – 510.
19. Mavko G., Mukerji T. and Dvorkin J., 2009, The rock physics handbook, *Cambridge University Press*, second edition, 355 – 357.
20. Msolo A. and Gidlow M., 2015, Relative Rock physics templates in the elastic impedance domain, *SEG Annual Meeting*, page 575 – 579.
21. Nam N. and Fink L., 2008, From angle stacks to fluid and lithology enhanced stacks, *7th international conference and exposition on geophysics,* page 41-45.
22. Nicholls M., Marler S. and Maguire D., 2014, Integrating 3D & 4D Rock Physics Inversion data into better understanding of field and reservoir behavior to mitigate production decline**,** *SEG Annual Meeting*, page 2798 – 2802.
23. Reuss A., 1929, Berechnung der Fließgrenze von Mischkristallen auf Grund der Plastizitatsbedingung f ¨ ur Einkristalle, *Zeitschrift für angewandte Mathematik und Mechanik,* vol 9, page 49–58.
24. Russell B., 2013, A Gassmann-consistent rock physics template, *Focus Article,* page 22 – 30.
25. Saul M. and Lumley D., 2015, The combined effects of pressure and cementation on 4D seismic data, *Geophysics*, vol 80, page 135 – 148.
26. Shuey R. T., 1985, A simplification of the Zoeppritz equation, *Geophysics,* vol 50, page 609 – 614.
27. Simm R. and Bacon M., 2014, Seismic Amplitude: An Interpreters Handbook, *Cambridge University Press.*
28. Simm R., White R. and Uden R., 2000, The anatomy of AVO cross-ploting, *The Leading Edge,* page 150-155.
29. Smith G. C. and Gidlow P. M., 1987, Weighted stacking for rock property estimation and detection of gas**,** *Geophysical Prospecting,* vol 35, page 993 – 1014.
30. Smith M., Gerhardt A. and Thomas P., 2010, Quantitative 4D interpretation – Relating the seismic to production changes at Enfield, North West Shelf, Australia, *ASEG*, page 1-4.

31. Sunday O. A., Kurt J. M. and Roger M., 2012, Time-lapse (4D) seismic effects: Reservoir sensitivity to stress and water saturation, *SEG Annual Meeting,* page 1- 6.
32. Taner M. T. and Koahler F., 1969, Velocity spectra-Digital computer derivation and applications of velocity functions, *Geophysics*, vol 34, page 851-889.
33. Trani M., Arts R., Leeuwenburgh O. and Brouwer J., 2011, Estimation of changes in saturation and pressure from 4D seismic AVO and time-shift analysis, *Geophysics,* vol 76, page C1-C17.
34. Whitcombe N. D., P. A. Connolly, R. L. Reagan and T. C. Redshaw, 2002, Extended elastic impedance for fluid and lithology prediction: *Geophysics*, vol 67, 63-67.
35. White R. and Simm R., 2003, Tutorial: Good practice in well ties, *first break*, vol 21, page 75-83.
36. Woods A. W, 1955, A textbook of sound, *McMillan Co*.
37. Yan F. and Han D., 2009, Modeling of effective pressure effect on porous reservoir rocks, *SEG Annual Meeting*, page 2025 – 2029.

Appendices

Appendix A

A1

The intercept and gradient or changes in intercept and gradient, can be calculated as:

$R_p = r_n N + r_m M + r_f F$

$G = g_n N + g_m M + g_f F$

$\Delta R_p = r_n \Delta N + r_m \Delta M + r_f \Delta F$

$\Delta G = g_n \Delta N + g_m \Delta M + g_f \Delta F$

For Nears, Mids and Fars, the weights are (using the least square difference):

$$r_i = \frac{\sum sin(\theta_i)^4 - \sin(\theta_i)^2 \sum sin(\theta_i)^2}{3\sum sin(\theta_i)^4 - (\sum sin(\theta_i)^2)^2}$$

$$g_i = \frac{\sum sin(\theta_i)^2 - 3\sin(\theta_i)^2}{(\sum sin(\theta_i)^2)^2 - 3\sum sin(\theta_i)^4}$$

Where i = nears, mids or fars and θ_i = near, mid or far angle

A2

Connolly defined EI as:

$EI(\theta) = V_P^a V_S^b \rho^c$

Where $a = 1 + tan^2\theta,\ b = -8\left(\frac{V_S}{V_P}\right)^2 sin^2\theta \quad and \quad c = 1 - 4\left(\frac{V_S}{V_P}\right)^2 sin^2\theta$

When the natural logarithm is introduced, the above equation for EI can be written as:

$ln(EI(\theta)) = ln(V_P^a V_S^b \rho^c)$

Using natural logarithm rules, the equation can be written as:

$$ln(EI(\theta)) = a\, ln(V_P) + b\, ln(V_S) + c\, ln(\rho)$$

The change in EI for a specific angle is:

$$\Delta\, ln(EI(\theta)) = a\, \Delta ln(V_P) + b\, \Delta ln(V_S) + c\, \Delta ln(\rho)$$

For small changes, $\Delta \ln x \approx \frac{\Delta x}{x}$. So,

$$\frac{\Delta EI(\theta)}{2EI} = a\frac{\Delta V_P}{2V_P} + b\frac{\Delta V_S}{2V_S} + c\frac{\Delta \rho}{2\rho}$$

This can be rearranged to:

$$R_{EI}(\theta) = \frac{1}{2}\left[\frac{\Delta V_P}{V_P} + \frac{\Delta \rho}{\rho}\right] - 2\left(\frac{V_S}{V_P}\right)^2\left[2\frac{\Delta V_S}{V_S} + \frac{\Delta \rho}{\rho} - \frac{1}{2}\frac{\Delta V_P}{V_P}\right] sin^2\theta + \frac{1}{2}\frac{\Delta V_P}{V_P}(tan^2\theta - sin^2\theta)$$

$R_{EI}(\theta) \approx R_P + G sin^2\theta$ *(For angles < 30, $tan^2\theta \approx sin^2\theta$, therefore the last term can be neglected)*

Whitcombe at el. (2002) replaced $\sin^2\theta$ by $\tan\chi$. Now the EI was extended from -90 to +90 degrees and was called, Extended Elastic Impedance (EEI).

$$R_{EI}(\chi) = R_P + G\, tan(\chi)$$

$$R_{EEI}(\chi) = R_{EI}(\chi)cos(\chi) = R_P cos(\chi) + G sin(\chi)$$

or

$$rel(EEI(\chi)) = R_P cos(\chi) + G sin(\chi)$$

Appendix B

B1

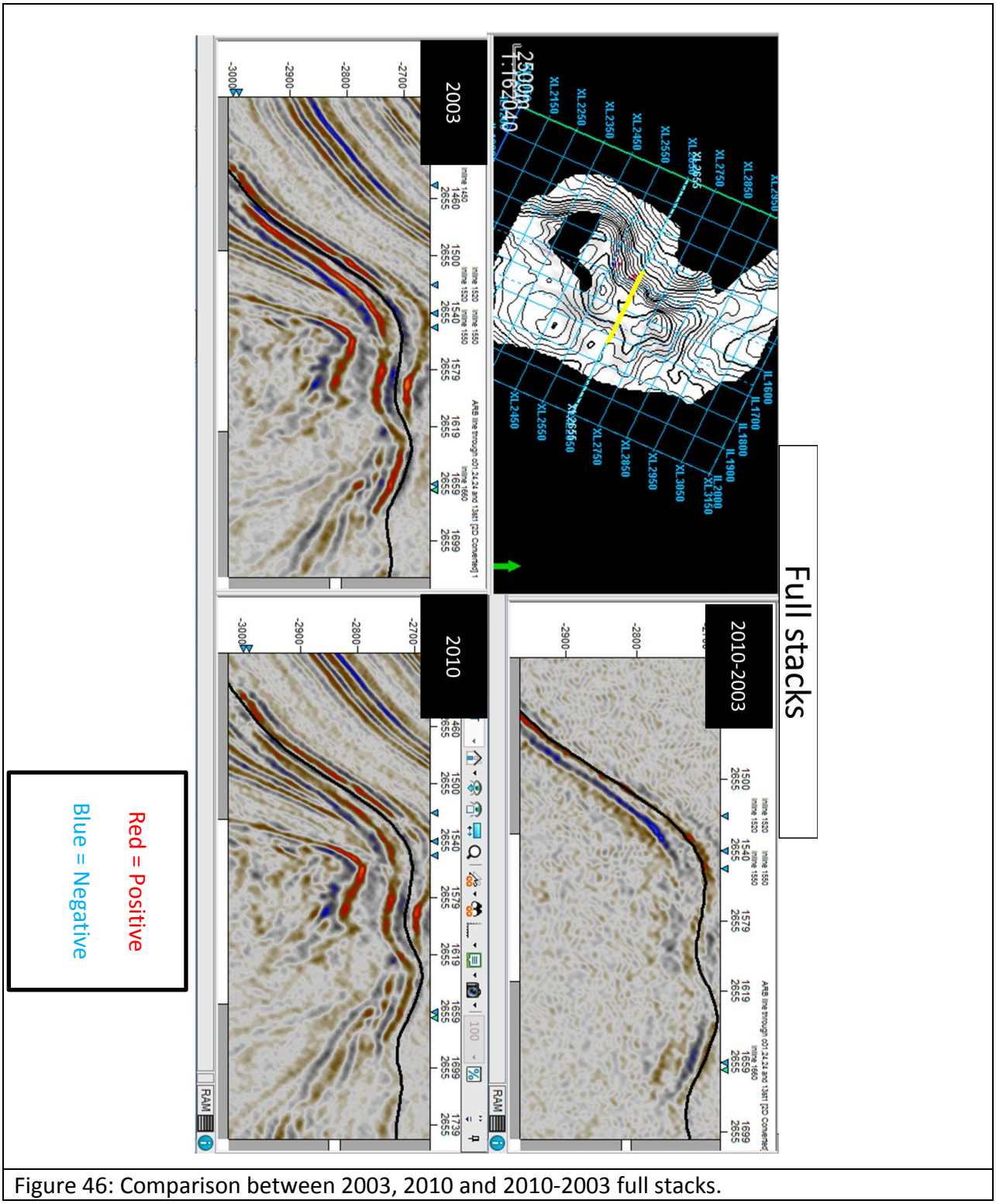

Figure 46: Comparison between 2003, 2010 and 2010-2003 full stacks.

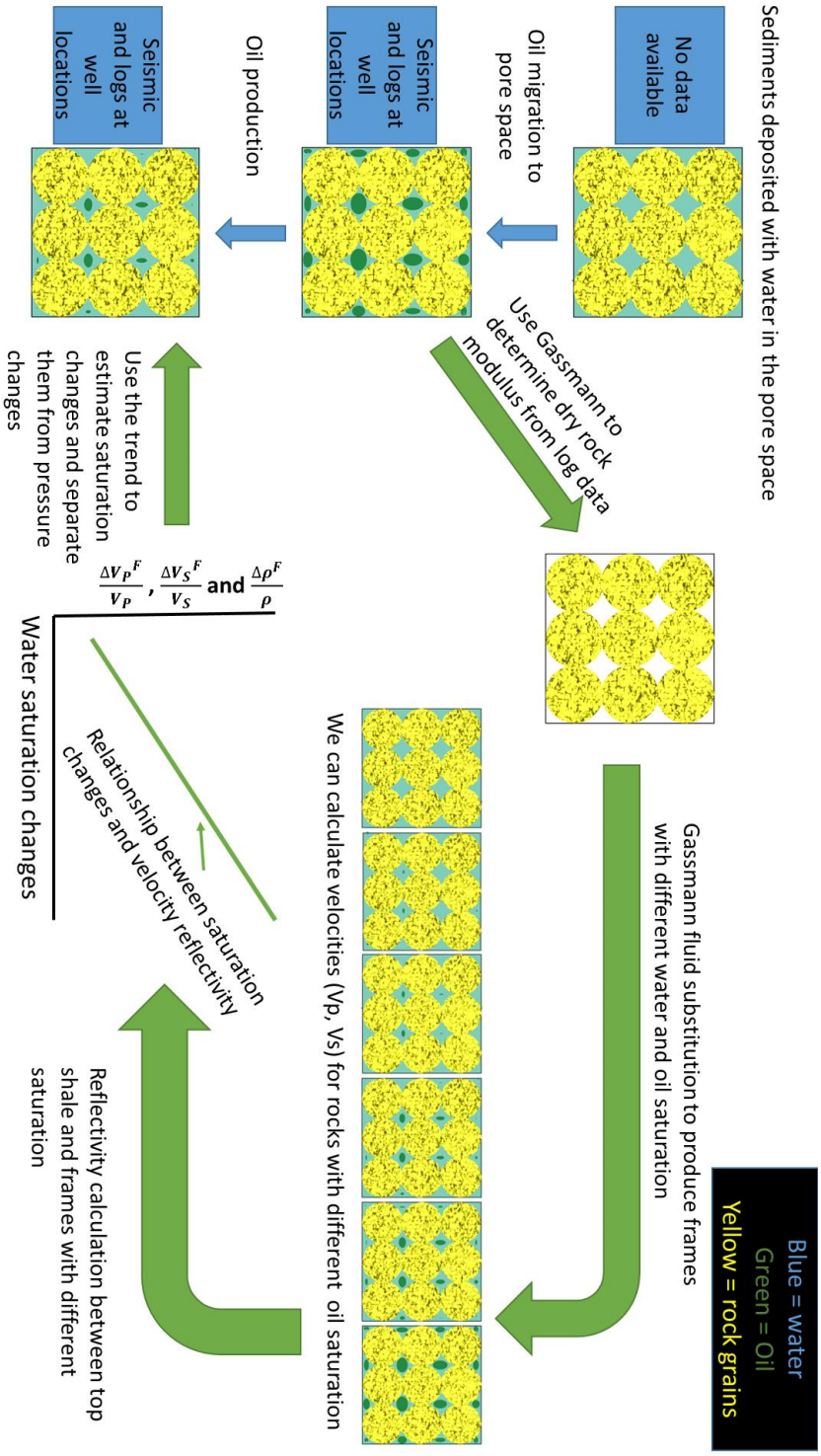

Figure 47: A cartoon showing processes that happen in the field (blue) and rock physics modeling steps (green).

B2

Below is a table for calculated changes in EEI (from -80 to +80) for the top of the reservoir.

Top Reservoir sands ΔEEIs	
2010-2003	
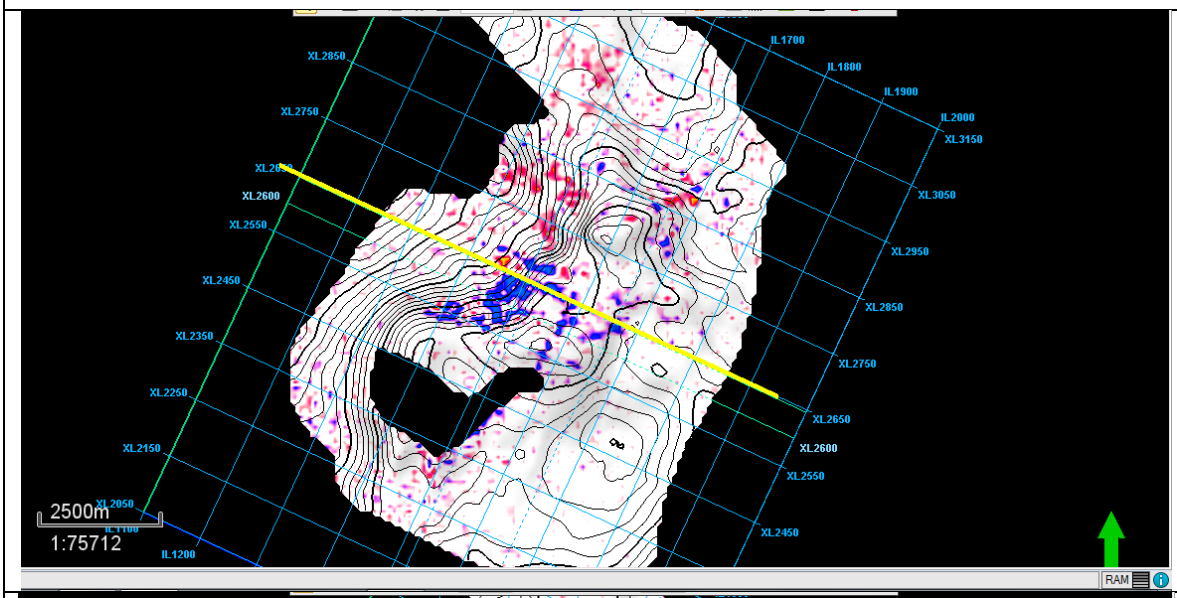	-80
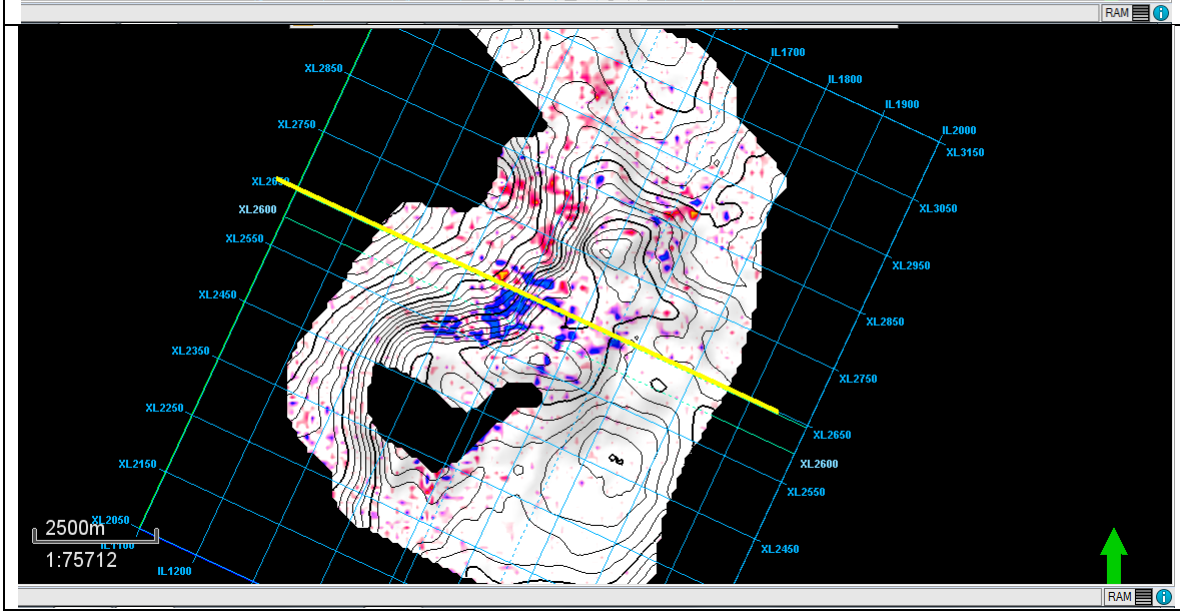	-70

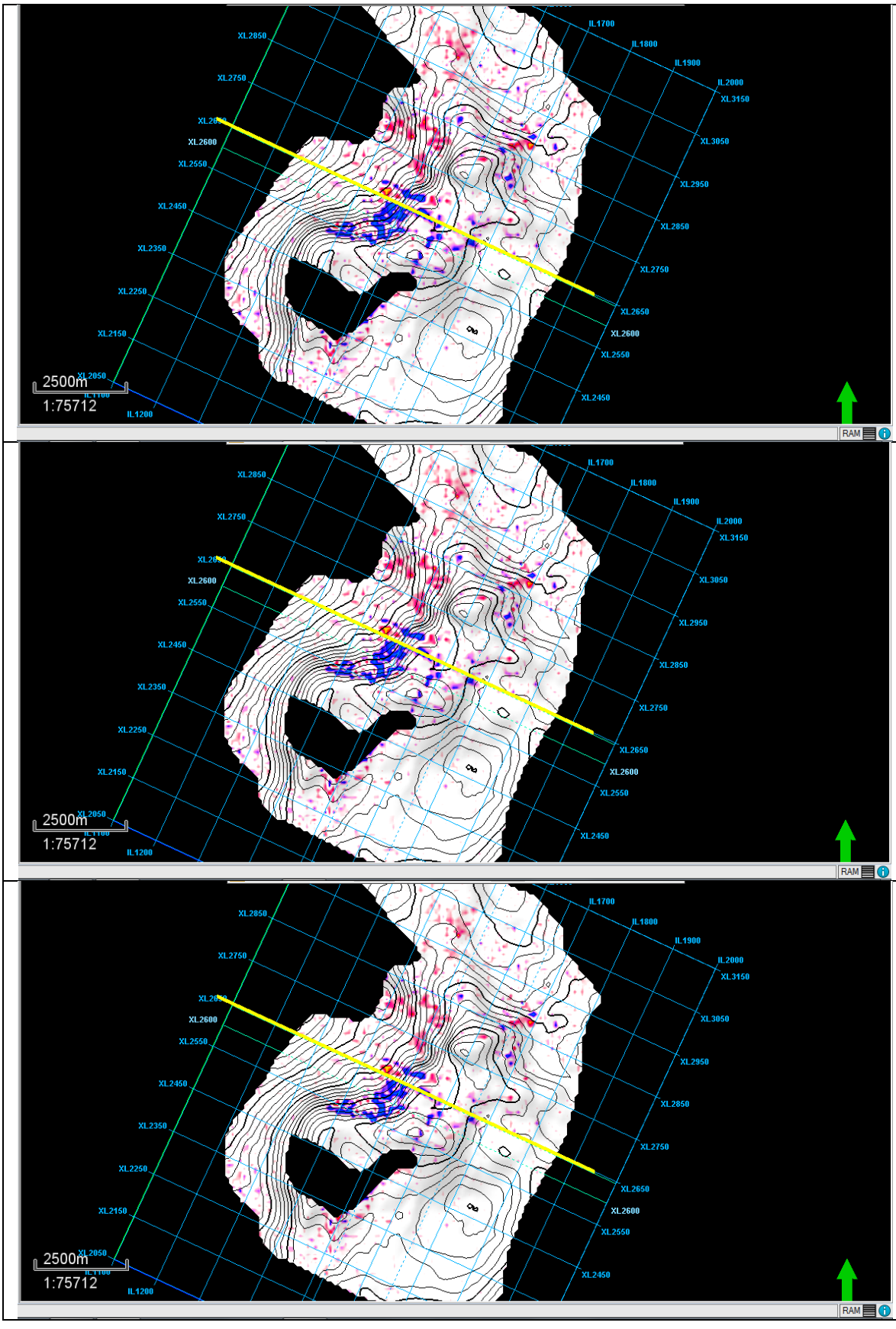
-60
-50
-40
IL1700
IL1800
IL1900
IL2000
XL3150
XL3050
XL2950
XL2850
XL2750
XL2650
XL2600
XL2550
XL2450
XL2350
XL2250
XL2150
XL2050
IL1200
2500m
1:75712
RAM

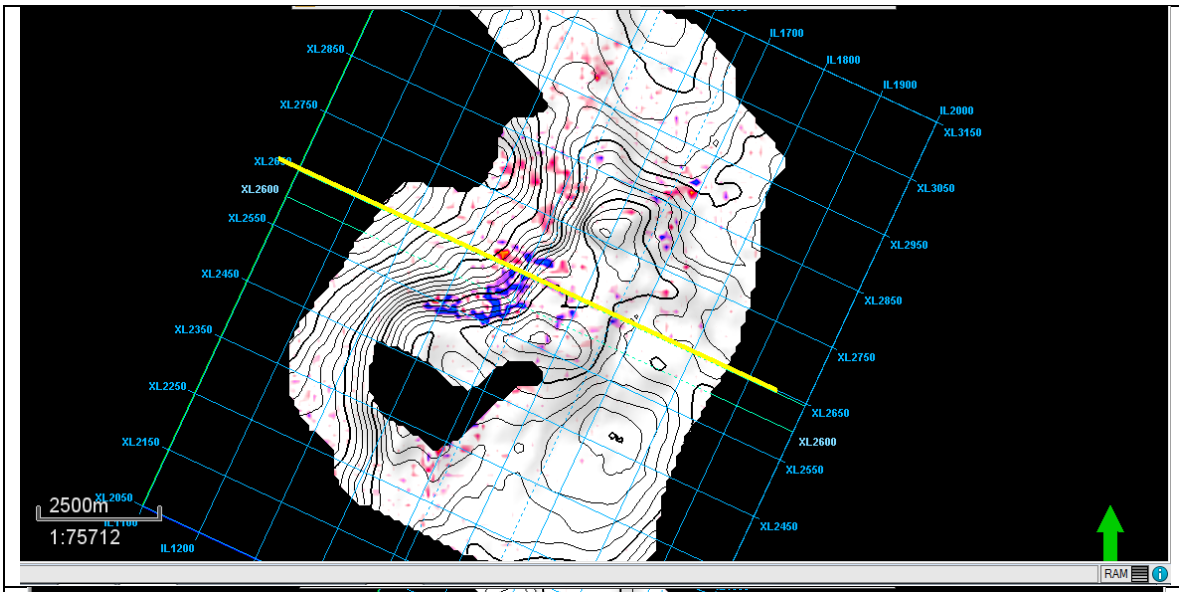
IL1700
IL1800
IL1900
IL2000
XL3150
XL3050
XL2950
XL2850
XL2750
XL2650
XL2600
XL2550
XL2450
XL2350
XL2250
XL2150
XL2050
IL1200
2500m
1:75712
RAM

-30

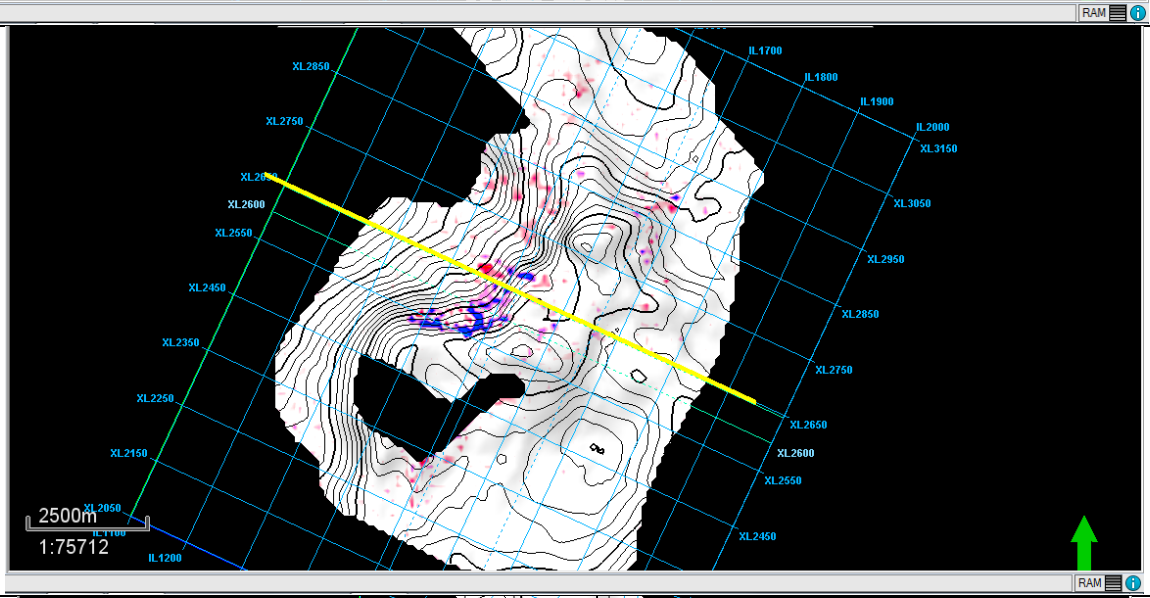
IL1700
IL1800
IL1900
IL2000
XL3150
XL3050
XL2950
XL2850
XL2750
XL2650
XL2600
XL2550
XL2450
XL2350
XL2250
XL2150
XL2050
IL1200
2500m
1:75712
RAM

-20

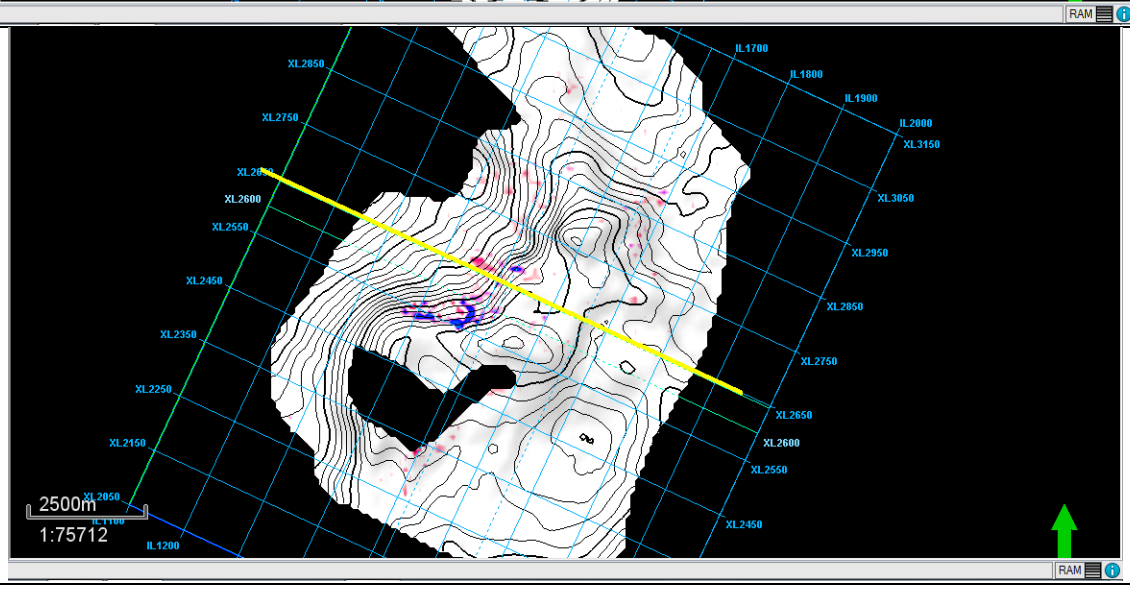
IL1700
IL1800
IL1900
IL2000
XL3150
XL3050
XL2950
XL2850
XL2750
XL2650
XL2600
XL2550
XL2450
XL2350
XL2250
XL2150
XL2050
IL1200
2500m
1:75712
RAM

-10

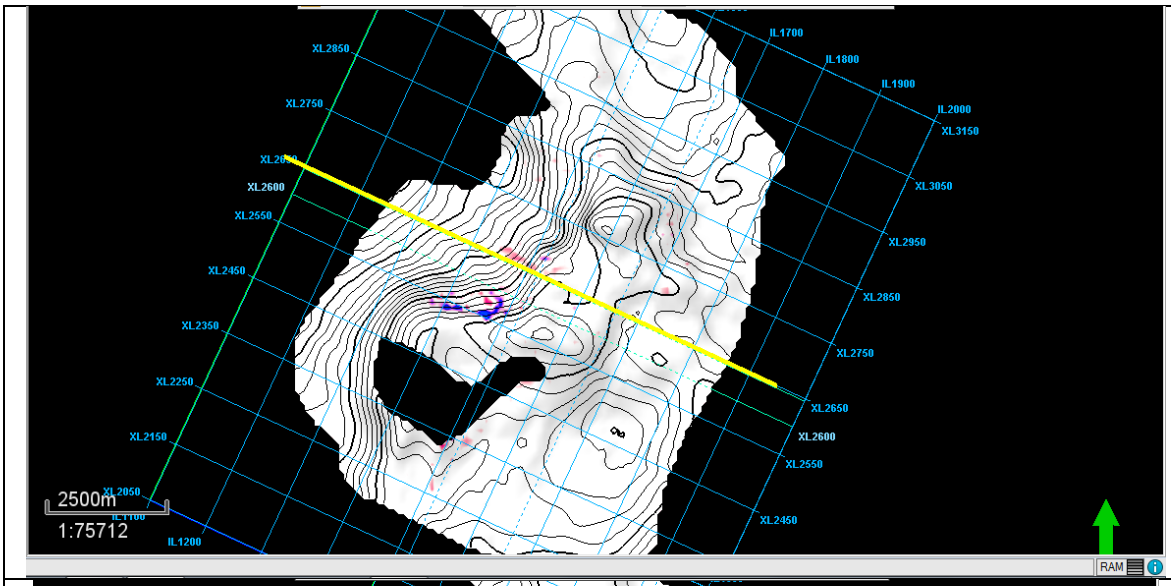
IL1700
IL1800
IL1900
IL2000
XL3150
XL3050
XL2950
XL2850
XL2750
XL2650
XL2600
XL2550
XL2450
XL2350
XL2250
XL2150
XL2050
IL1200
2500m
1:75712
RAM

0

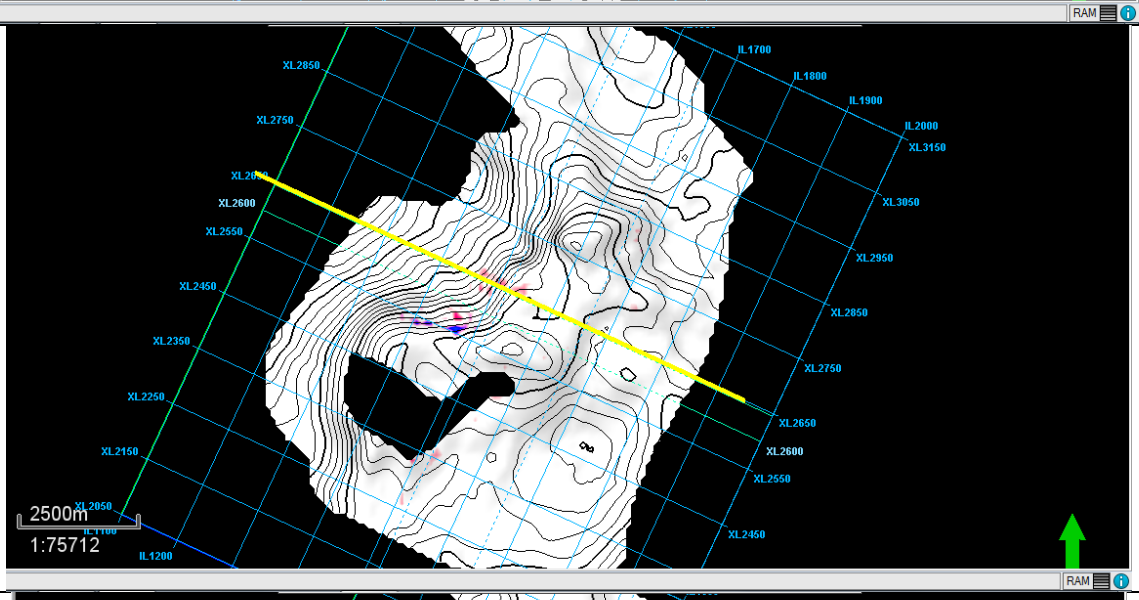
IL1700
IL1800
IL1900
IL2000
XL3150
XL3050
XL2950
XL2850
XL2750
XL2650
XL2600
XL2550
XL2450
XL2350
XL2250
XL2150
XL2050
IL1200
2500m
1:75712
RAM

10

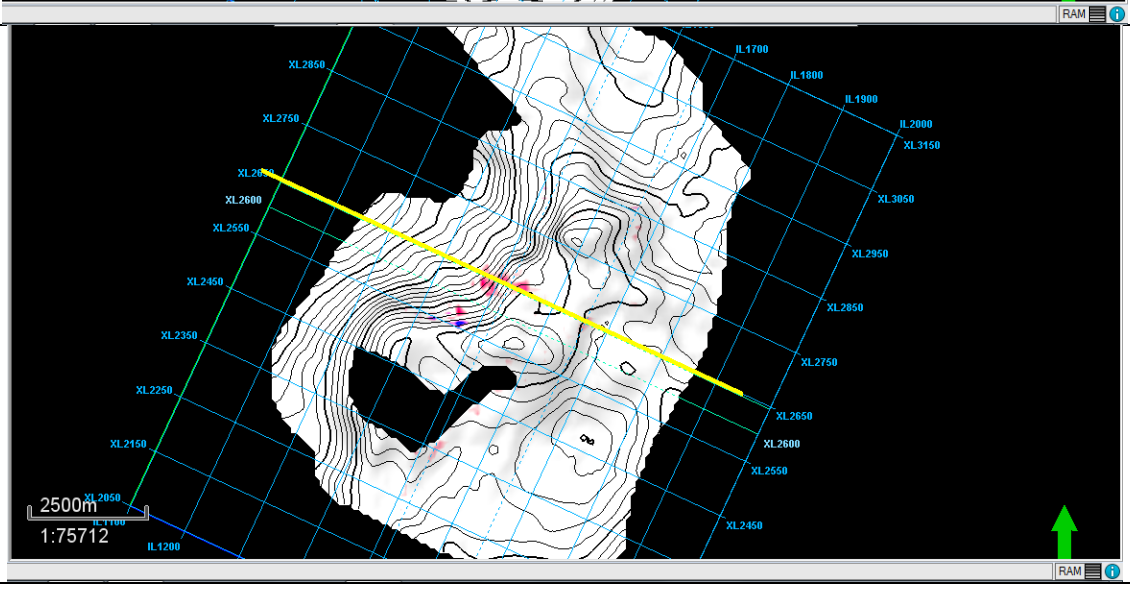
IL1700
IL1800
IL1900
IL2000
XL3150
XL3050
XL2950
XL2850
XL2750
XL2650
XL2600
XL2550
XL2450
XL2350
XL2250
XL2150
XL2050
IL1200
2500m
1:75712
RAM

20

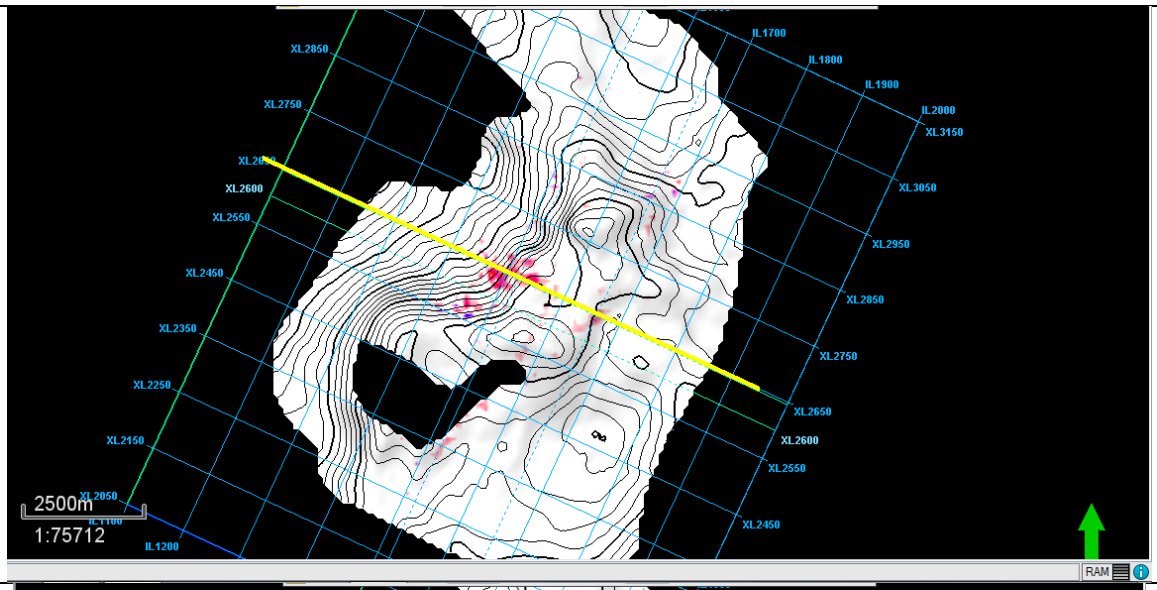
IL1700
IL1800
IL1900
IL2000
XL3150
XL3050
XL2950
XL2850
XL2750
XL2650
XL2600
XL2550
XL2450
XL2350
XL2250
XL2150
XL2050
IL1200
2500m
1:75712
RAM

30

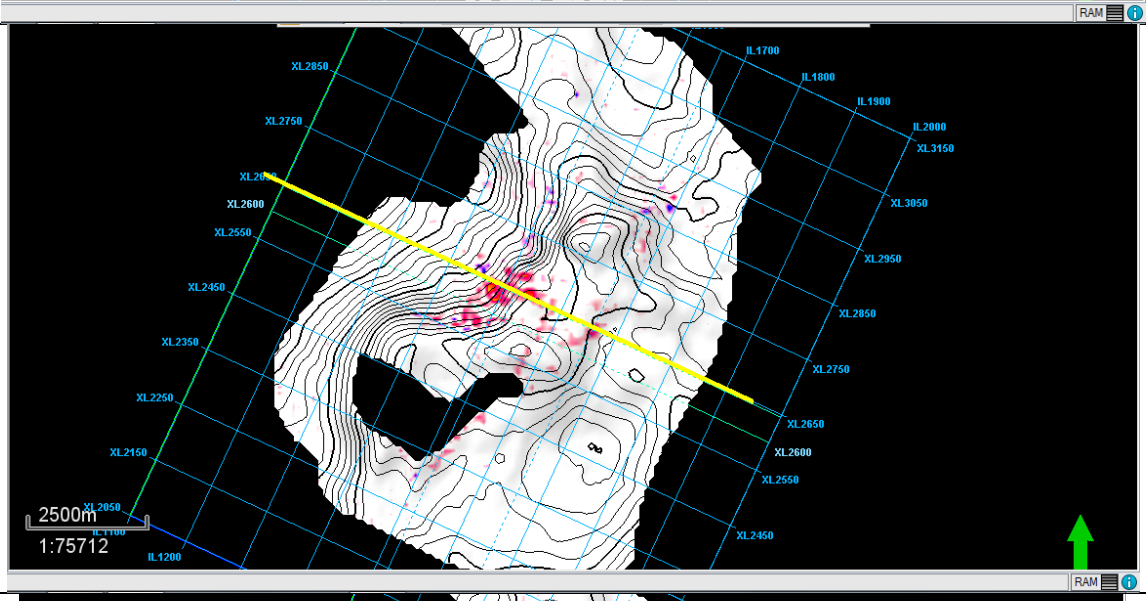
IL1700
IL1800
IL1900
IL2000
XL3150
XL3050
XL2950
XL2850
XL2750
XL2650
XL2600
XL2550
XL2450
XL2350
XL2250
XL2150
XL2050
IL1200
2500m
1:75712
RAM

40

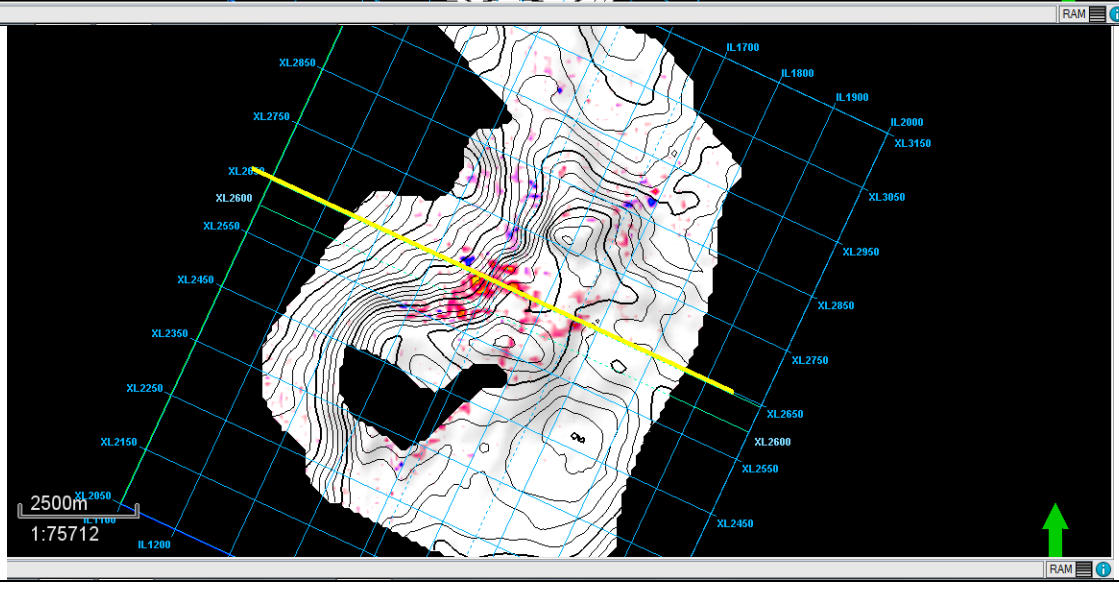
IL1700
IL1800
IL1900
IL2000
XL3150
XL3050
XL2950
XL2850
XL2750
XL2650
XL2600
XL2550
XL2450
XL2350
XL2250
XL2150
XL2050
IL1200
2500m
1:75712
RAM

50

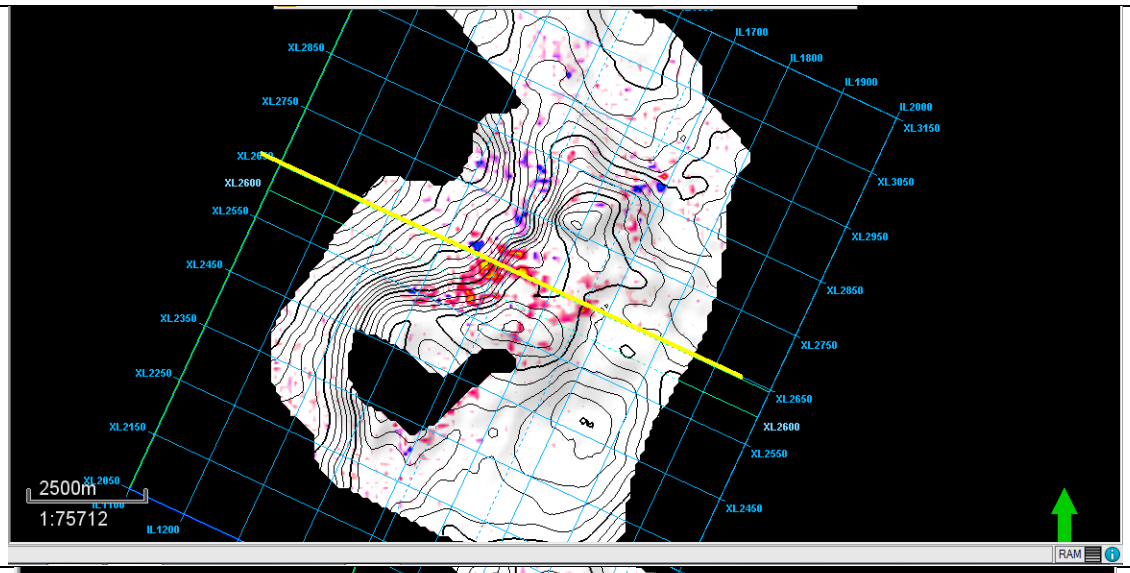

60

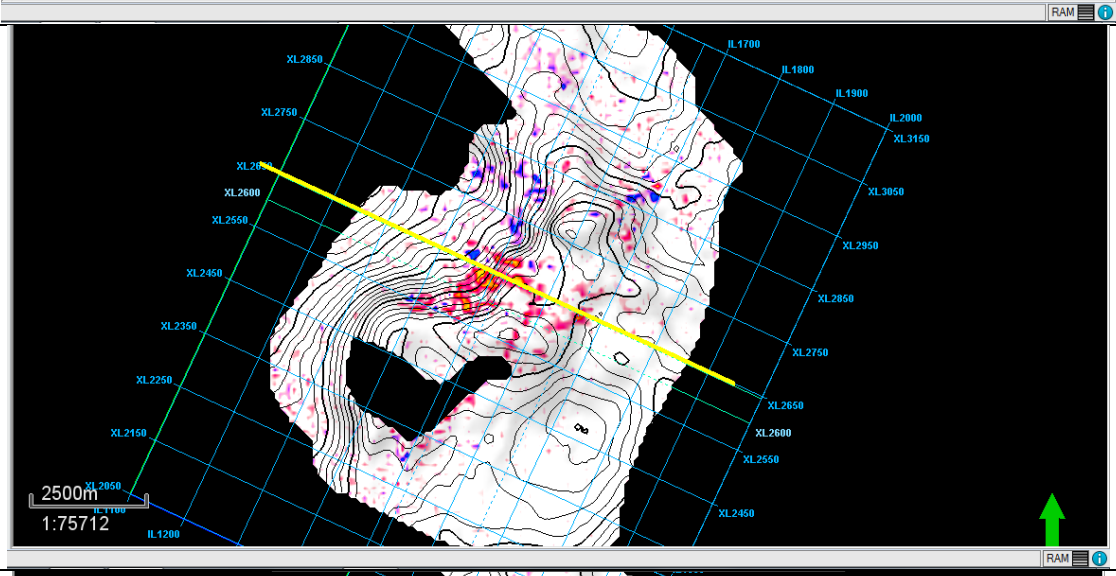

70

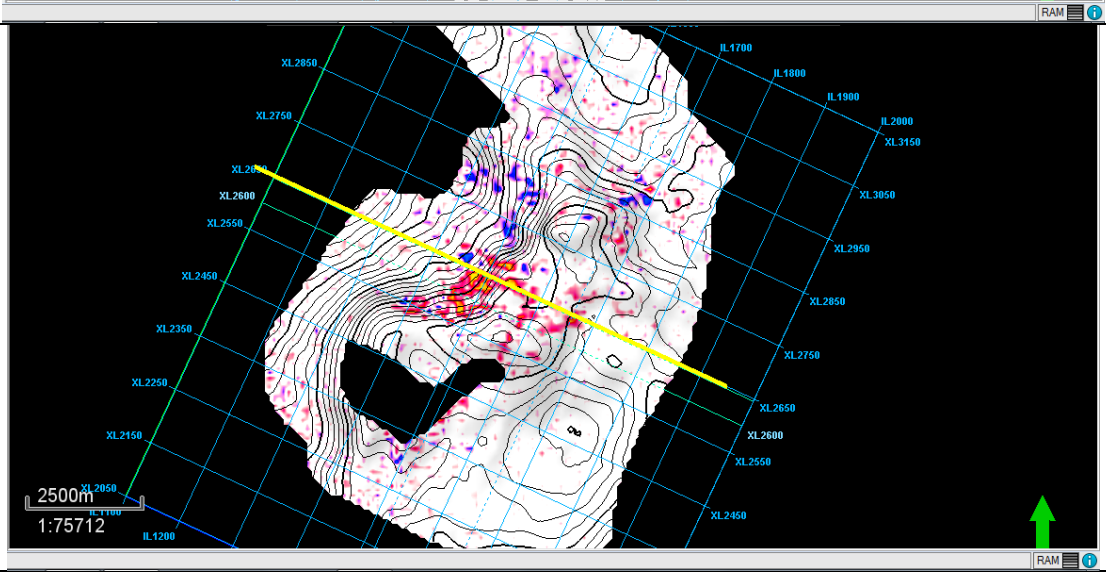

80

Table 5: Calculated changes in EEI (left) with corresponding χ angle (right).